British & Irish Chapter of ISMRM Annual Conference

ISMRM | British & Irish CHAPTER

"New Horizons in MRI"

13 - 15 September 2023

PROGRAMME & ABSTRACTS

WE WISH TO THANK ALL OUR SPONSORS AND EXHIBITORS!

GOLD SPONSORS

BRUKER

GE HealthCare

GOLD STANDARD PHANTOMS

SIEMENS Healthineers

SILVER SPONSORS

MR SOLUTIONS

BRONZE SPONSORS

RAPID Biomedical

RS²D REINVENT SYSTEMS FOR SCIENCE & DISCOVERY

tesla ENGINEERING LTD

neoscan solutions

SINAPSE

DEEPSPIN

HYPERFINE®

EXHIBITORS

Xiel.

Table of Contents

Welcome

This year's conference of the British and Irish Chapter of ISMRM (BIC-ISMRM) will be held at the King's College Conference Centre, University of Aberdeen, in the North-East of Scotland. The theme of the conference will be "New Horizons in MRI".

The University of Aberdeen has a long history of research in MRI; the first whole-body MRI scanner was developed here in the late 1970s and the first-ever diagnostic body scan took place at the University of Aberdeen in 1980.

The conference will be held over three days (13th-15th September 2023). The first day will consist of a Workshop on the highly topical subject of Low-Field MRI. The following two days will include invited, oral and poster presentations covering all aspects of MRI. It will bring together scientists, doctors and students concerned with the development and use of MRI from a broad range of disciplinary and geographical regions, primarily from the UK and Ireland, but also from around the world.

A fantastic array of speakers have agreed to deliver invited lectures at the conference and workshop and we are delighted that Professor Fiona Gilbert (University of Cambridge) will deliver the flagship Bill Moore Lecture at this year's meeting.

The organisers wish to extend a very warm welcome to all delegates, speakers, exhibitors and sponsors of BIC-ISRMR 2023 to Aberdeen and to the University of Aberdeen.

Prof. David J. Lurie
Chair of Local Organising Committee

Local Organising Committee

University of Aberdeen

Prof David Lurie (chair)
Dr Lionel Broche
Mrs Teresa Morris
Dr James Ross
Dr Najat Salameh
Dr Mathieu Sarracanie
Dr Gordon Waiter
Mrs Julie Dixon (Event Organiser)
Ms Cara Nicolson (Event Admin)

PROGRAMME

New Horizons in MRI

Full Programme

Wednesday 13th September 2023 - Workshop on low-field MRI

9:15 - 09:45	**Registration**	
9:45 - 10:00	**Welcome**	
10:00 - 11:00	**Invited Lectures:** Low field applications	**Chair: James Ross**
	10:00 – 10:30	Professor Amedeo Chiribiri, King's College London Low-field cardiac MRI: when lower is better
	10:30 – 11:00	Professor Mara Cercignani, University of Cardiff A Journey into Advanced Imaging with Low-Field MRI
11:00 - 11:30	**Refreshment break**	
11:30 - 12:30	**Invited Lectures:** Low field technology **Chair: Mathieu Sarracanie**	
	11.:30 – 12:00	Dr. Tom O'Reilly, Leiden University (NL) Accessible low field MRI – Simple and open hardware
	12:00 – 12.30	Dr. Lionel Broche & Dr. Najat Salameh, University of Aberdeen Distilling information from low field systems: from signals to contrast mechanisms
12:30 - 13:30	**Lunch Break**	
13:45 - 14:15	**Private Bus to Medical School campus at Foresterhill**	
14:30 - 16:30	**Guided visits to MRI facilities:** (a) Original "Mark-I" 0.04T scanner (1980) (b) New clinical Field-Cycling Imaging scanner (c) Low-field MRI laboratory	
16:45 - 17:15	**Private Bus back to city centre**	
19:00 start	**Café Scientifique public engagement/outreach event**, Aberdeen Art Gallery, Schoolhill, Aberdeen AB10 1FQ MRI Research in Aberdeen: the past, present and future Event is free, but pre-booking is required, at this link	
20:30 - late	**"Get-to-Know-You"** gathering/informal get-together. All invited from BIC-ISMRM "Newbies" to seasoned PIs. Drinks will not be provided (alas)! Old School House Pub, Little Belmont Street, Aberdeen AB10 1JG, < 5 minute walk from the Art Gallery.	

Thursday 14th September 2023 - Main conference day 1

9:00 - 9:30	**Registration**	
9:30 - 9:45	**Welcome**	
9:45 - 10:15	**Invited Speaker, Professor David Norris, Radboud University (NL)** **Chair: Richard Bowtell** The Dutch National 14 Tesla Initiative: Approaching the Final Frontier? Note: this lecture will be streamed to BIC members (and members of other European chapters) as part of the BIC-ISMRM online educational programme.	
10:15 - 10:45	**Refreshment break, posters and exhibits**	
10:45 - 12:15	**Proffered talks session 1:** Low field MRI **Chair: Najat Salameh**	
	10:45 - 10:57 PT1-1	James Ross Progress towards cardiac T1 dispersion imaging using field-cycling imaging
	10:57 - 11:09 PT1-2	Marco Fiorito Towards cryogen-free SQUID-MRI at ultra-low field
	11:09 - 11:21 PT1-3	Amnah Alamri In-vivo and ex-vivo detection of Colorectal Cancer at ultra-low field using Fast Field-Cycling methods
	11:21 - 11:33 PT1-4	Reina Ayde Comparing different sampling approaches with data-driven reconstruction techniques for low-field fast MRI acquisitions
	11:33 - 11:45 PT1-5	Nicholas Senn Automated segmentation and quantification of cerebral small vessel disease severity using field-cycling MRI
	11:45 - 11:57 PT1-6	Vasiliki Mallikourti Breast cancer imaging at low and ultra-low magnetic fields using Field Cycling Imaging: a clinical pilot study
	11:57 - 12:09 PT1-7	Harriet Kammayani (remote presentation) African Experience with Ultra-low Field MRI on the REVAMP-TT Study: A Malawian perspective from a Nurse-Midwife and GATES-ISMRM UNITY Mentee.
12:15 - 13:45	**Lunch & posters** (BIC Exec Committee meeting will be held over lunch time, in break-out room) Odd number poster presenters: stand by your poster 13:00-13:45	
13:45-14:15	**Gold Sponsor talks** **Chair: David Lurie** GE Healthcare Gold Standard Phantoms	
14:15 -15:00	**Bill Moore Invited Lecture,** Professor Fiona Gilbert, University of Cambridge **Chair: David Lurie** Standing on the shoulders of Giants – clinical application of the developments in MR	
15:00 0 15:30	**Refreshment break, posters and exhibits**	
15:30 -17:00	**Proffered talks session 2: Advances in clinical MRI** **Chair: Mara Cercignani**	
	15:30 0 15:42 PT2-1	Francesco Digeronimo Exploring the Potential of Quantitative Susceptibility Mapping (QSM) to Predict Plaque Rupture Risk: Ex Vivo Human Carotid Atherosclerotic Plaque QSM Pipeline Optimisation
	15:42 - 15:54 PT2-2	Faiz Alqarni Magnetic resonance imaging measurement of colon length in adults with functional constipation and healthy controls
	15:54 - 16:06 PT2-3	Timothy Mulvany Identification of Distinct Prognostic Groups of Paediatric Brain Tumours using Unsupervised Learning
	16:06 - 16:18 PT2-4	Adrian Tang T1 Dark, Bright or Fright? : Clinical Fat Saturation techniques in the lateral neck from a Medicolegal perspective
	16:18 - 16:30 PT2-5	Elizabeth Shumbayawonda Liver Magnetic Resonance Imaging, Non-Alcoholic Fatty Liver Disease and Metabolic Syndrome Risk in Pre-Pubertal Mexican Boys
	16:30 - 16:42 PT2-6	Charlotte Swain Improving the patient experience for paediatrics in Magnetic Resonance Imaging through Play Therapy
	16:42 - 16:54 PT2-7	Farahnaz Bashah (remote presentation) Hemispheric dominance during comforting sound at various intensity levels: Evidence from BOLD fMRI.
17:00	**Independent travel to city centre for civic reception and conference dinner**	
18:30 - 19:30	**Civic Reception**, Townhouse, Union Street/ Broad Street, Aberdeen AB10 1AQ	
19:30	**Conference Dinner**, Townhouse, Union Street/ Broad Street, Aberdeen AB10 1AQ	

Friday 15th September 2023 - Main conference day 2

9:00 - 9:30	**Invited Speaker,** Dr. Karyn Chappell, Imperial College London MADI: Harnessing the Magic of the Magic Angle Effect	**Chair: Harish Poptani**
9:30 - 10:30	**Proffered talks session 3:** Preclinical Studies	**Chair: Harish Poptani**
	9:30 - 9:42 PT3-1	Christopher Ball Quantitative Dixon imaging and MR spectroscopy to characterise early alterations in liver fat in a novel model of diet-induced Metabolic Associated Fatty Liver Disease.
	9:42 - 9:54 PT3-2	Tareq Alrashidi 1H MR spectroscopy to evaluate the effect of a choline kinase inhibitor and temozolomide therapy in a mouse model of glioblastoma
	9:54 - 10:06 PT3-3	Hana Lahrech Transmembrane water exchange in cellular metabolism and its role on T1 relaxation at low field: towards an invasion/migration theranostic imaging
	10:06 - 10:18 PT3-4	Elisabeth Gash Investigating the effects of hypoxia on tumour vasculature in a chick chorioallantoic (CAM) model of glioblastoma using MRI
10:30 - 12:00	**Refreshment Break & Posters** Even number poster presenters: stand by your poster 11:15-12:00	
12:00 - 12:45	**BICISMRM Annual General Meeting** (open to all conference attendees)	
12:45 - 13:45	**Lunch & Posters**	
13:45 - 14:15	**Invited Lecture:** Professor Jim Wild, University of Sheffield **Chair: Lionel Broche** Hyperpolarised xenon MRI - methods and applications in the lungs and beyond	
14:15 -15:30	**Proffered talks session 4:** Novel methods & applications	**Chair: Lionel Broche**
	14:15 - 14:27 PT4-1	Dominic Harrison Lung ventilation 19F-MRI using FLORET ultrashort echo time imaging.
	14:27 - 14:39 PT4-2	Mehrsa Jafarpour Age Related Changes in Peripheral Muscle Metabolism
	14:39 - 14:51 PT4-3	Liene Balode $T1_{\varrho}$ imaging for detecting takotsubo cardiomyopathy
	14:51 - 15:03 PT4-4	Teodora Catargiu Identifying Brain Calcifications in Down Syndrome Patients: An Analysis Using ZTE-Derived Pseudo-CT Imaging
	15:03 - 15:15 PT4-5	Oriana Arsenov Rapid In-Vivo Quantitative Conductivity Mapping in the Human Brain Using a Multi-Echo EPI Sequence
	15:15 - 15:27 PT4-6	Gabriel Zihlmann A High-Performance Clustered Dictionary Search Engine using GPUs
15:30 - 16:15	**Refreshment break**	
16:15 - 16:45	**Awards & Closing**	

INVITED SPEAKERS

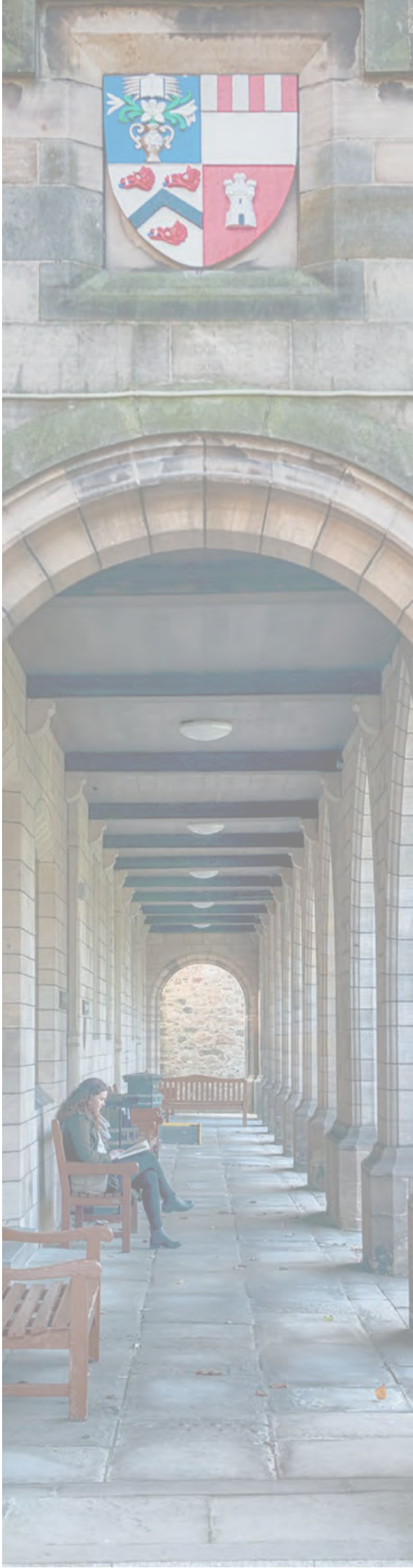

Dr Lionel Broche

University of Aberdeen

Talk Title: **Distilling information from low field systems: from signals to contrast mechanisms**

Biography: I am currently leading the Fast Field-Cycling group at the University of Aberdeen, which is world-leading in the development of large-band, field-cycling imaging scanners. We are currently developing Field-Cycling Imaging (FCI), a new imaging technology derived from MRI that has the unique ability to measure the dynamics of water and lipid molecules non-invasively. This provides unique insights on the pathological remodelling of tissues during the progression of diseases, with exciting applications in medicine. FCI opens access to a new domain of medical research that remains to be explored.

I am currently conducting clinical research showing that FCI can detect stroke, breast cancer, brain glioma, liver fibrosis and osteoarthritis, amongst other pathologies. My research encompasses many disciplines such as electronic engineering, spin physics, biophysics, physiology, cell biology, system engineering or electromagnetism, and my current research direction focuses on three research topics:

- discovering the medical applications of FCI, incuding the biological mechanisms underlying the FCI image contrast
- technology developments of FCI
- dissemination of FFC imaging using open-source hardware

Prof. Mara Cercignani

University of Cardiff

Title: **A Journey into Advanced Imaging with Low-Field MRI**

Biography: Mara Cercignani is Head of MRI at CUBRIC. Her research focuses on quantitative MRI and its application to the study of the central nervous system in health and disease. Best known for her work in white matter imaging, she has been a Senior Fellow of the International Society for Magnetic Resonance in Medicine (ISMRM) since 2019, and a Deputy Editor for Magnetic Resonance in Medicine since 2014. She has published over 180 papers in peer-reviewed journals.

Dr. Karyn Chappell

Imperial College London

Talk Title: **MADI: Harnessing the Magic of the Magic Angle Effect**

Biography: Dr Karyn Chappell is a Postdoctoral Research Radiographer at Imperial College London.

Karyn has never chosen the easiest path in her working life. From doing a PhD involving rummaging around in the dustbin of MRI history to currently preferring not to predict the future of MRI but creating and building it. Life is never boring!

Karyn's research uses magic to make the invisible visible. The 'Magic Angle Directional Imaging' (MADI) technique developed during her PhD harnesses the Magic Angle effect: visualising the alignment of collagen fibres within tendons, ligaments, meniscus, and cartilage. Karyn is working with Mechanical Engineers developing a novel extremity MRI scanner that moves around the patient facilitating in-vivo magic angle research.

Prof. Amedeo Chiribiri

King's College London

Talk Title: **Low-field cardiac MRI: when lower is better**

Biography: Prof Amedeo Chiribiri is a recognised world leading expert in cardiac imaging and cardiovascular MRI. He studied medicine in Turin/Italy and received and MD from the University of Turin in 2001 and completed specialist training in Cardiology in 2006 and a PhD in Human Physiology and Experimental Medicine in 2010.

Between 2006 and 2007, he was visiting physician at the German Heart Institute Berlin (DHZB), Germany, where he specialised in cardiovascular MRI. He works as Consultant Cardiologist at Guy's & St Thomas' Hospital since March 2008. In April 2013, he took up the post as Senior Lecturer in Cardiovascular Imaging at King's College London and in August 2013 he became the Director of the Cardiovascular MRI Service at Guy's and St Thomas' Hospital.

He was promoted to Associate Professor (Reader) in Cardiovascular Imaging in August 2018 and to Full Professor (Chair) in November 2020. Prof Chiribiri's main clinical and research interest is cardiovascular imaging, with a focus on cardiovascular MRI and quantitative imaging. His areas of expertise include the assessment of cardiac structure and function and tissue characterisation using non-invasive imaging, and on the application of machine learning techniques for the acquisition and interpretation of the scans.

Prof Chiribiri has developed several techniques that enable the non-invasive assessment of myocardial blood flow (perfusion) and the non-invasive differential diagnosis between different causes of chest pain. Moreover, Prof Chiribiri is actively involved in the development and validation of novel experimental models to simulate physiological and pathophysiological processes and in the development of low-field MRI scanners for cardiovascular applications.
Speciality: Cardiology, cardiovascular MRI.

Prof. Fiona Gilbert

University of Cambridge

Bill Moore lecture

Talk Title: **Standing on the shoulders of Giants – clinical application of the developments in MR**

Biography: Professor Fiona Gilbert – FRCR, FRCPS, FRCP, FACR, FRSE, FMedSci.

Fiona Gilbert is Professor of Radiology and Head of Department at the University of Cambridge. Her clinical work and research is focused on imaging breast cancer using multimodal functional imaging such as MRI and PET to study the tumour environment and evaluating different modalities for early detection.

Professor Gilbert has over 250 peer reviewed publications, 5 book chapters and numerous international conference abstracts. She was awarded Honorary membership of Radiological Society of North America, Honorary fellowship of the American College of Radiologists, the Royal Society of Edinburgh and the Academy of Medical Sciences and the Gold Medal from the European Society of Radiology. She is immediate past President of the European Society of Breast Imaging.

Prof. David Norris

Radboud University, NL

Talk Title: **The Dutch National 14 Tesla Initiative: Approaching the Final Frontier?**

Biography: I studied Physics at Cambridge and did a Masters in Medical Physics at Aberdeen. My PhD thesis was entitled “NMR Flow Imaging”, supervised by Jim Hutchison at Aberdeen. I then moved to the University of Bremen as a post-doc and later had a tenure-track position. I was head of MR at the Max-Planck-Institute for Cognitive and Behavioural Sciences in Leipzig before moving to the Donders Institute at the Radboud University Nijmegen in 2001. I am a past director of the Donders Centre for Cognitive Neuroimaging and a founding Director of the Erwin L. Hahn Institute at the University Duisburg-Essen. I am a Past-President of the International Society for Magnetic Resonance in Medicine and an External Scientific Member of the Max-Plank-Society. I am the Principal Investigator of the Dutch 14 T initiative (DYNAMIC).

Dr Tom O'Reilly

Leiden University, NL

Talk title: **Accessible low field MRI – Simple and open hardware**

Biography: I studied physics at Leiden University and got my introduction to MRI by doing an internship on the human 7T system working on various application of dielectric materials for manipulating B1 fields, and got the opportunity to pursue a PhD continuing that work in the same group. Shortly after starting my PhD the idea of working on a low field MRI system for imaging Hydrocephalus in infants came up and I was allowed to switch the focus of my PhD to try and bring that system to reality. A driving factor of our work on low field has always been to make the system available to as many people as possible for which our vision has been to utilise materials and methods that are easily sourced and to share our code and designs in an open manner so that others can replicate, adapt and improve the system for their needs. Last year we built a replica of our system in Uganda and were joined by people from all over Africa, as well as the U.S. and South America with the aim of spreading the knowledge of how to build these systems.”

Dr Najat Salameh

University of Aberdeen

Talk Title: **Distilling information from low field systems: from signals to contrast mechanisms**

Biography: Over the last 20+ years I have developed a strong expertise in MR imaging, with multidisciplinary skills ranging from fundamental physics to microsurgery in rodents. I position myself at the interface between Physics and Medicine, easily navigating between developing new methods for MRI and technology transfer to clinical and preclinical applications. Over the years, I have designed, implemented, and validated imaging protocols with very diverse magnetic fields ranging from 0.0065 T to 9.4 T. My area of expertise includes MR elastography in the liver and brain, thermometry, metabolic imaging, and low magnetic field MRI.

Together with Dr. Sarracanie, we co-founded the Center for Adaptable MRI Technology (AMT Center) in 2017 when we were assistant professors in Basel, and have recently (April 2023) relocated our entire low-field MRI platform in Aberdeen, at the Institute of Medical Sciences. Extensive refurbishment of the Biomedical Physics building is currently happening, where three of our fixed, low-field scanners along with 2 Field-Cycling whole-body systems will find their new home. This joint effort with me, Dr. Sarracanie, Dr. Broche, and Dr. Ross will contribute to the largest low-field MR technology platform ever built with about 900 m2 of lab and office space, at the heart of the Foresterhill campus.

Prof. Jim Wild

University of Sheffield

Talk Title: **Hyperpolarised xenon MRI - methods and applications in the lungs and beyond**

Biography: I am an MR imaging physicist, my own research focus is the physics, engineering and clinical applications of MR imaging of hyperpolarised gases in lungs and other organs. In 2015 our POLARIS group established these modalities as part of clinical diagnostic imaging in the NHS a world first for hyperpolarised MRI.

ORAL ABSTRACTS

PT1-1

Progress towards cardiac T1 dispersion imaging using field-cycling imaging

James Ross[a], Gareth Davies[a], Robert Stormont[ab], David Lurie[a], Lionel Broche[a], Dana Dawson[a]

[a]University of Aberdeen, Aberdeen, UK
[b]GE Healthcare, Milwaukee, US

Introduction: Field-Cycling Imaging (FCI) is a novel low-field magnetic resonance technique where the external magnetic field, B_0, is deliberately and stepwise decreased during the imaging sequence. Varying B_0 allows the spectrum of the spin-lattice relaxation time T_1 to be probed as a function of magnetic field, known as T_1 dispersion. Our research team have previously shown that T_1 dispersion has new diagnostic potential in ischaemic stroke and breast cancer without the need for exogeneous contrast agents using a home-built FCI scanner with a maximum field strength of 0.2 T. Our previous work made use of transceiver coils, however these are impractical for thoracic applications which typical employ larger receive-only arrays. Although common at high field, array technology has had little development in the low field regime below 20 MHz. In this work we describe the construction of a six-channel anterior-posterior torso array and present the first in-vivo FCI cardiac images and T_1 dispersion from healthy volunteers.

Methods: Both the anterior and posterior coils of the array were constructed with three elements [each element made of a 2-turn 160 mm loops wound from high-frequency 1699 x 0.020 litz wire (Elektrisola Co., Reichshof-Eckenhagen, Germany)] and arranged in a "Venn Diagram" configuration to provide a degree of passive geometric decoupling. Additional decoupling and transmit protection was achieved by impedance matching through a lattice-balun to custom built low impedance preamplifiers (WMA08HA - WanTcom Inc., Chanhassen, MN, USA). The lateral inter-element and axial inter-element coupling figures and Q factors were measured using a vector network analyser (Rhode and Schwarz Co. Munich, Germany).

As a proof of concept, we then used the torso array to collect full left ventricular coverage, short-axis cardiac images (Figure 1) from n = 20 healthy volunteers with scan parameters: slice thickness = 15 mm, slice gap = 2 mm, in-plane resolution = 5.75 mm, FOV = 460 mm, bandwidth = 33 kHz, TE = 22 ms with spin-echo readout. Images were collected ats four predefined field strengths (200 mT, 20 mT, 2 mT, 200 µT from which T_1 dispersion information was derived for healthy left ventricular myocardium. FCI scans were performed twice to assess repeatability of T_1 dispersion measurements. Data is shown as mean±SD.

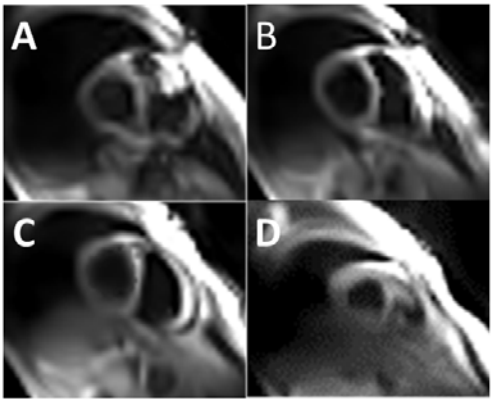

Figure 1. Four short-axis views (A: base, B-C: mid venticle, D: apex) from a volunteer acquired at 0.2T using the array coil demonstrating good image quality and excellent left ventricle delineation.

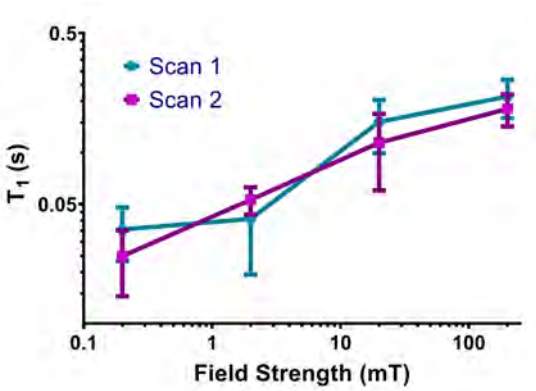

Figure 2. T_1 dispersion results derived from the left ventricle of healthy volunteers. Volunteers underwent two scans in order to assess repeatability of T_1 dispersion measurements.

Results: After localisation, the left ventricle was readily visible in all volunteer FCI images. The derived mean T_1 dispersion values were 0.2 T: 215 ms ± 88, 0.02 T: 149 ms ± 42, 0.002 T: 36 ms ± 19.1, 0.0002 T: 32 ms ± 14. Repeat T_1 dispersion measurements show good reproducibility (Figure 2). Our results are in keeping with T_1 dispersion measurements observed in skeletal muscle.

Conclusions: We have successfully built a six-channel torso array coil for imaging at 0.2T and below and demonstrated the first in-man field-cycling cardiac imaging with T_1 dispersion values of healthy human myocardium. This paves the way for exploring new applications of field-cycling imaging in cardiovascular disease.

PT1-2

Towards cryogen-free SQUID-MRI at ultra-low field

M. Fiorito, I. Saniour, E. Grimaldi, S. Varotto, Y. Belkhodja, R. Couvreur, D. Labat

Chipiron, 75005 Paris, France

Introduction. Over the past decade, a new approach has emerged in the field of MRI, which involves the use of ultra-low field (ULF<10mT) scanners. Besides the cost-effectiveness and portability of ULF MRI, operating at these low magnetic fields has shown improvements in T1 contrast in some tissues [1,2], leading to more efficient diagnostics of various medical conditions, including cancer. The main challenge of ULF MRI lies in a detected signal typically orders of magnitude lower compared to clinical-field MRI, which impacts the signal-to-noise ratio (SNR) in the images. Several methods [3,4] are being explored to address this limitation and improve the sensitivity of ULF MRI. The inherent challenge of poor sensitivity in ULF MRI can be mitigated by choosing a superconducting quantum interference device (SQUID) for signal detection. Various groups [2,5] used SQUIDs at 4.2K employing liquid Helium (LHe) cooled cryostats. The use of cryogenic liquid is detrimental to achieving portable and low-cost MRI systems. Here we propose our first implementation of a cryogen-free SQUID detector inductively coupled to a customised volume MRI RF coil operating at room temperature. We further present our first free induction decay (FID) signal acquired using a fully custom-made ULF MRI scanner at 1mT, which relies on a conventional inductive reception.

Methods. *SQUID sensor*: A micrometre-sized low critical temperature Niobium-based SQUID is coupled to a larger flux transformer in a current-sensing configuration. This transformer comprises a 300K RF pickup coil and a 4.2K superconducting input coil positioned in close proximity to the SQUID in a washer design. Fig.1a illustrates the cryogen-free cryostat, which relies on a pulse tube cryocooler and is used to house the SQUID at a temperature of 4.2K. The magnetic flux seen by the SQUID is directly proportional to the one passing through the second-order volume gradiometer used as RF pickup coil, illustrated in Fig.1b. In order to estimate the far noise filtering of our detection system, we measured the signal detected by the SQUID sensor when emitted by a dipole-like magnetic field coil as function of the distance between the RF source and the isocenter of the gradiometer. *MRI hardware and sequence parameters*: A Merrit coil electromagnet fed by a current source generates a B0 field of 1mT (Fig.2a). The RF field transmission is performed using an 80mm-diameter saddle coil with 5 turns, while the RF reception is achieved using a solenoid-based volume gradiometer. Both RF coils are tuned to 42.5kHz and matched to 50Ohm. The received signal is amplified using a low-noise preamplifier (FEMTO). 0.5L of doped water ($NiSO_4$) was used as a phantom. The FID measurement was obtained in 5min using the following sequence parameters: FA=90°, TR=0.5s, sampling rate=8kHz, with an acquisition window of 200 ms and 120 averages.

Results. *Signal detection with a SQUID sensor coupled to a gradiometer at 300K*: Fig.1c confirms a linear decrease in signal intensity with distance, which translates to effective filtering of far-field noise. *Measurement of the FID at 1mT*: Fig. 2b shows the temporal decay of the demodulated NMR signal received by a similar volume gradiometer RF coil (without the SQUID), as well as its frequency spectrum before demodulation. The peak in the signal is observed at 42.5kHz, corresponding to the expected proton Larmor frequency at 1mT.

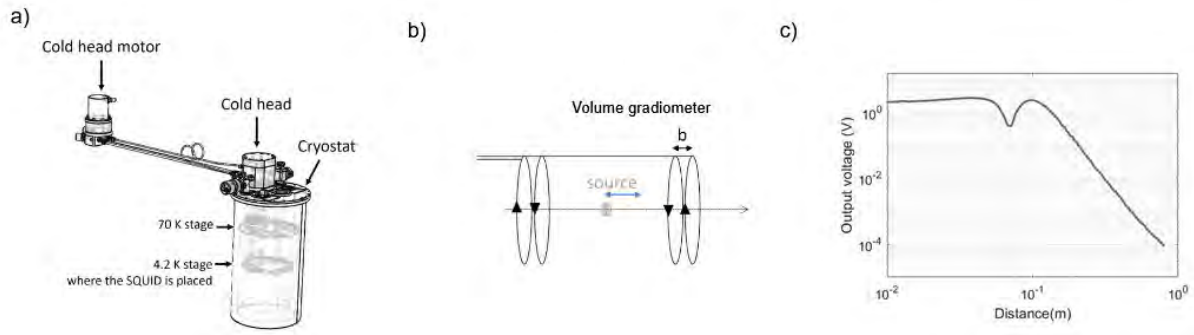

Fig. 1. Schematics of a) the cryostat structure and b) the second-order volume gradiometer. c) Signal detected by the SQUID sensor as a function of the distance between the RF source and the gradiometer isocenter.

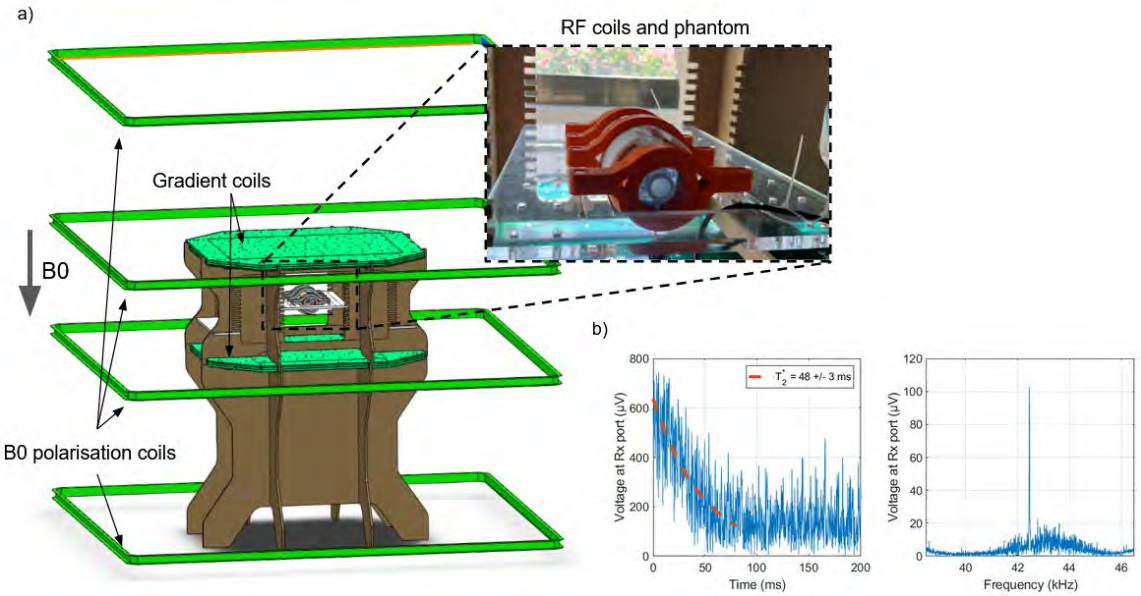

Fig. 2. a) Schematic of the main part of our ULF MRI machine. b) FID signal detected using a volume gradiometer pick up coil in a conventional inductive reception, in the time (left) and frequency domain (right).

Discussion. The experiments show that the SQUID sensor, combined with the room temperature volume gradiometer, can effectively detect the signal generated by an RF source. In addition, the SQUID sensor efficiently rejects far-field noise. Furthermore, we successfully detected an FID signal using our custom-made ULF MRI setup, through a volume gradiometer and a low noise preamplifier. With an equivalent current noise of 2nA/Hz, the noise introduced by the preamplifier is expected to be two orders of magnitude greater than the SQUID's equivalent current noise. Therefore, we anticipate a significantly higher detected SNR when the SQUID is connected to the MRI.

Conclusions. ULF MRI is an emerging and promising technology that has yet to be fully explored. Based on our experimental results, an approximately 102 times higher SNR is expected when integrating the SQUID technology into our ULF scanner, hence envisioning clinical employment of MRI at such field regime.

References

[1] Busch S. et al. MRM, 67:1138–1145, 2012
[2] Clarke J. et al., Annu. Rev. Biomed. Eng., 9:389–412, 2007
[3] Zotev VS et al., JMR, 207:78-88, 2010
[4] Liu Y. et al., Nature Communications, 12, 7238, 2021
[5] Seton, HC et al., Cryogenics, 45:348-355

PT1-3

In-vivo and ex-vivo detection of Colorectal Cancer at ultra-low field using Fast Field-Cycling methods

Amnah Alamri[a], Nicholas Senn[a] , Graeme Murray[b], Leslie Samuel[b], George Ramsay[b] ,Lionel Broche[a]

[a]University of Aberdeen, Aberdeen, United Kingdom.
[b]Aberdeen Royal Infirmary, Aberdeen, United Kingdom.

Introduction: Worldwide, Colorectal Cancer (CRC) is the third most commonly diagnosed cancer and the second leading cause of cancer-related deaths [1]. An estimated 39% of these cancers are found in the rectum [2]. Colonoscopy is currently used for the early diagnosis of CRC. However, because a colonoscopy is an unpleasant and invasive procedure, many patients are unwilling to undergo such an examination [3]. Currently, CRC diagnosis is expanding beyond structural assessment, and evaluating tumour microenvironment using non-invasive imaging has gained increasing importance. Field-Cycling is a tool that measures changes in R_1 relaxation rate ($1/T_1$) with the magnetic field strength [4,5]. R_1 Nuclear Magnetic Relaxation Dispersion (NMRD) profiles, acquired with field cycling technique, can provide promising biological biomarkers non-invasively and without using contrast media, using ultralow-field magnetic resonance [6,7]. The aim of this pilot study was to explore potential biomarkers in colorectal cancer samples using the field cycling NMR Relaxometry and to test the feasibility of the whole body field cycling scanner to characterise rectal cancer.
Methods: Twenty-eight fresh resected tumour samples and corresponding peritumoral and healthy counterparts were obtained via the NHS Grampian Biorepository (tissue request-TR000068), with informed consent obtained from all patients. The dispersion profiles were acquired using a commercial Field Cycling NMR Relaxometry at a controlled temperature of 37^{o}C +/- 0.1^{o}C. Field-Cycling pre-polarised and non-polarised pulse sequences were used. For imaging work (study approval number 22/NS/0035), we scanned four patients diagnosed with rectal cancer by using an FCI scanner, with four evolution fields ranging from 0.2 T to 0.2 mT and five evolution times. The slice thickness was set to 10mm, TE of 21 ms, 20 kHz bandwidth, in-plane resolution of 4.3 mm, with a matrix size of 100 x 100. The duration of the FCI scan is approximately 45 minutes.
Results: The difference of R_1 values measured between healthy, peritumoral and tumour tissue samples is increased with the decrease of the magnetic field from 3.4 to 1.01 MHz and showed a significant difference ($p<0.0001$) between the tissue subtypes. The FCI scans were correlated to the clinical MRI images to delineate the ROIs, and multi-fields T_1 images were obtained (Fig 1). The in-vivo R_1 dispersion profiles showed clear contrast between tumour and healthy regions with different dispersion shapes.

Fig 1. Typical FCI data from a patient diagnosed with Locally Advanced Rectal Cancer (LARC). The evolution times are reported in ms along the columns, and the evolution fields in mT along the rows.

Discussion: This preliminary study provided the first insights into using FFC-NMR and FCI imaging to characterise colorectal cancer. The FFC-NMR measurements were able to discriminate tumours from peritumoral and healthy tissues in all 28 cases. This work was extended to in vivo imaging, and the preliminary results were reported. Although the primary source of the signals is not well defined yet, previous studies have reported that ($R_1 = 1/T_1$) is related to changes in molecular dynamics within tumour tissues, and the water exchange rate across the plasma membrane is a distinctive feature that distinguishes healthy from tumour cells [7,8].

Conclusions: This work showed a potential new biomarker of colorectal cancer based on R_1 dispersion curves -extended to low magnetic fields -below 3.4 MHz-. Furthermore, this work is extended to in vivo imaging, and we reported the preliminary results of using our whole-body 0.2 T FCI scanner to assess if FCI can characterise rectal lesions.

References

[1] Rawla, P. et al. Epidemiology of colorectal cancer: incidence, mortality, survival, and risk factors. Przegląd Gastroenterol. 14, 89–103 (2019).

[2] Sung, H. et al. Global Cancer Statistics 2020: GLOBOCAN Estimates of Incidence and Mortality Worldwide for 36 Cancers in 185 Countries. CA. Cancer J. Clin. 71, 209–249 (2021).

[3] J, N. & Jr, S. Colonoscopy quality: measuring the patient experience. Endoscopy https://pubmed.ncbi.nlm.nih.gov/29268293/ (2018).

[4] Steele, R. M. et al. New applications and perspectives of fast field cycling NMR relaxometry. Magn. Reson. Chem. 54, 502–509 (2016).

[5] Kimmich, R. & Anoardo, E. Field-cycling NMR relaxometry. Prog. Nucl. Magn. Reson. Spectrosc. 44, 257–320 (2004).

[6] Masiewicz, E. et al. Towards applying NMR relaxometry as a diagnostic tool for bone and soft tissue sarcomas: a pilot study. Sci. Rep. 10, 14207 (2020).

[7] Broche, L. M. et al. A whole-body Fast Field-Cycling scanner for clinical molecular imaging studies. Sci. Rep. 9, (2019).

[8] Ruggiero, M. R. et al. Relaxometric investigations addressing the determination of intracellular water lifetime: a novel tumour biomarker of general applicability. Mol. Phys. 117, 968–974 (2019).

PT1-4

Comparing different sampling approaches with data-driven reconstruction techniques for low-field fast MRI acquisitions

Reina Ayde[1,2], Najat Salameh[1,2], Mathieu Sarracanie[1,2]

[1] Center for Adaptable MRI Technology (AMT Center), Institute of Medical Sciences, School of Medicine, Medical Sciences & Nutrition, University of Aberdeen, Aberdeen, United Kingdom.
[2] Center for Adaptable MRI Technology (AMT Center), Department of Biomedical Engineering, University of Basel, Allschwil, Switzerland.

Introduction: Low magnetic field (LF) MRI is currently gaining momentum as a complementary, flexible, and cost-effective approach to MRI diagnosis [1]. A common limitation of LF MRI lies however in the lower available spin polarization yielding low Signal-to-Noise-Ratio (SNR) images. During the image acquisition process, multiple averages (NA) can be used to boost the SNR by roughly $\sqrt{\mathrm{NA}}$, although at the cost of prolonged acquisition times, compromising patient comfort and hindering the relevance of LF MRI for clinical routine. Lately, advanced reconstruction techniques based on deep learning have shown promising results accelerating acquisitions when combined with *k*-space down-sampling. Undersampling is commonly done using a binary sampling scheme (mask) usually favoring low spatial frequencies (i.e., defining contrast and the overall object shape) in an image, at the expense of high frequencies containing small features (i.e., details) [2]. Leveraging low (or very low) NA without omitting *k*-space information constitutes another means to accelerating acquisition times, yet with a direct penalty on SNR. In this case, deep-learning algorithms can be used to perform a denoising task [3, 4] to boost SNR. In this work, we evaluated those two different sampling strategies for accelerated MR acquisition at 0.1 T using a data-driven DL reconstruction technique.

Methods:

Sampling strategies

Maintaining constant acquisition time, 30% sampling of a full 3D *k*-space with a Gaussian probability density function was challenged with low averaging of a fully sampled *k*-space (Fig. 1). Details on the investigated sampling masks are given below:
A) Undersampling (US): it consists of a binary mask applied to the phase encode 1 and 2 directions (readout always fully sampled) following a gaussian-like sampling pattern. 30% of *k*-space is sampled and each sampled *k*-space line is acquired with a maximum number of averages N_{max}.
B) Uniform averaging: every *k*-space line is averaged equally N times = 0.3 x N_{max}.

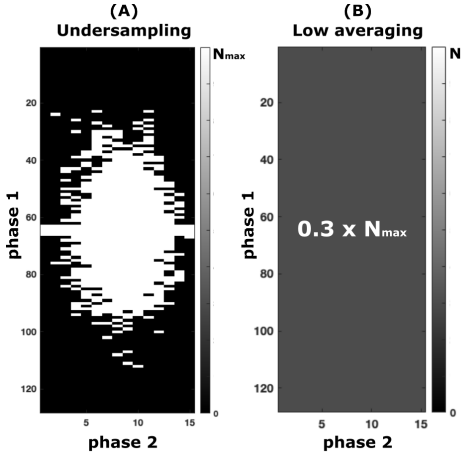

Figure 2: *Two down-sampling mask. (A) 30% of k-space lines are sampled with the maximum averaging N_{max}. (B) All the k-space lines are averaged equally: $0.3xN_{max}$. All scales are normalized number of averaging.*

Training

A total of 7 datasets of 3D MR *in-vivo* human wrist were acquired at 0.1 T (4.2 MHz) in a compact biplanar MRI system [5] after informed consent was obtained. The following acquisition parameters were used: matrix = [128 x 128 x 15], voxel size = [1 x 1 x 2.9] mm^3, TE/TR = 7/13.9 ms, and NA = 10 (acquisition time = 4min25s). Each average was individually stored in a fourth dimension, allowing retrospective manipulation of *k*-spaces to generate images according to different masks. The maximum SNR of the training set is 56.0 ± 7.0. Accelerated acquisitions by a factor of x3.3 were simulated according to the two sampling schemes described. Finally, two residual U-net models were trained on pairs of full and down-sampled MR images using the RMSProp optimizer with the mean squared error as a loss function. Data augmentation was applied to prevent overfitting.

Testing

The reconstruction performances of the two models were evaluated on two sets of data (30 2D MR images) of *in-vivo* human hand/wrist that were acquired with the same acquisition parameters described above with comparable overall maximum SNR of 56.9 ± 1.7. The reconstructed images were evaluated using the structure similarity index (SSIM), normalized root mean squared error (NRMSE) and Peak SNR (PSNR) as metrics.

Results: Figure 2 compares residual U-net reconstruction in a selected image sample in the human wrist. Despite an improvement in edge sharpness with DL reconstruction, US sampling inherently exhibits filtered high frequencies (i.e., blurring). In contrast, uniform sampling followed by a denoising model demonstrates higher details (edge) preservation and good fidelity to the reference image. Quantitatively, uniform averaging shows better metrics (cf. table 1).

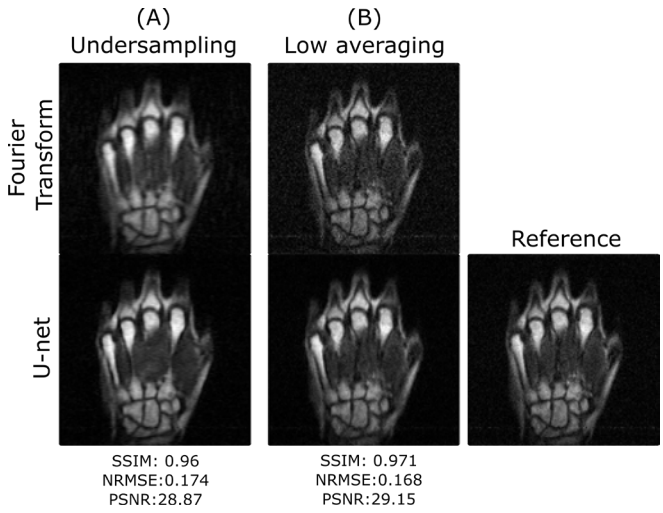

	Undersampling	Low averaging
SSIM	0.915±0.127	0.941±0.093
NRMSE	0.246±0.128	0.197±0.094
PSNR	28.465±2.879	30.219±3.295

Table 1: *Quantitative results of retrospectively 3.3-fold down-sampled test data using the two different masks and reconstructed with the corresponding residual U-nets.*

Figure 2: *Reconstruction performance of residual U-net on in-vivo human wrist MR data. The first row is the Fourier transform of retrospectively accelerated (x3.3) acquisition according to the two masks. The second row shows the reconstructed magnitude images using the corresponding trained models.*

Discussion: With a purely data-driven reconstruction approach, uniform low averaging appears to be more advantageous than undersampling omitting high spatial frequency lines in *k*-space. Data-driven approaches like the one used in this study (residual U-net) are typically useful for removing artifacts (aliasing, noise etc.). However, lost information such as high spatial frequencies cannot be fully recovered. Therefore, noisier, uniform sampling with low averaging seems more beneficial than US when a data-driven deep learning approach is used for reconstruction at low-SNR regimes.

Conclusions: This study examined two distinct down-sampling techniques, which were subsequently followed by a residual U-net deep learning reconstruction. The findings indicate that uniform sampling approach is more advantageous than undersampling when using a data-driven reconstruction approach.

Acknowledgements: Forschungfunds Grant from university of Basel (HIFI project). Swiss National Science foundation Grant No. 186861 and 198905.

References

[1] M.Sarracanie *et al.,* Front. Phys, 8 (2020). https://doi.org/10.3389/fphy.2020.00172
[2] Ayde *et al., Sci Rep* 12, 11394 (2022). https://doi.org/10.1038/s41598-022-14039-7
[3] Koonjoo *et al. Sci Rep* 11, 8248 (2021). https://doi.org/10.1038/s41598-021-87482-7
[4] Maosong *et al.* Medical Image Analysis, 55:165-180 (2019). https://doi.org/10.1016/j.media.2019.05.001
[5] Constantinesco *et al.,* Magnetic Resonance in Chemistry, 35 (1997). https://doi.org/10.1002/(SICI)1097-458X(199712)35:13%3CS69::AID-OMR198%3E3.0.CO;2-5

PT1-5

Automated segmentation and quantification of cerebral small vessel disease severity using field-cycling MRI

Nicholas Senn[a], Vasiliki Mallikourti[a], James Ross[a], Lionel Broche[a], Gordon Waiter[a] and Mary-Joan MacLeod[a]

[a] Aberdeen Biomedical Imaging Centre, University of Aberdeen, AB24 3FX, UK

Introduction: Cerebral small vessel disease (SVD) is associated with increased stroke risk and contributes to cognitive decline in ageing populations [1]. New clinically viable approaches are now needed to realise the potential of non-invasive imaging to routinely monitor changes to the severity of SVD in patients. Field-cycling imaging (FCI) is an emerging whole-body MRI technology being developed at the University of Aberdeen [2]. FCI provides unique access to underlying tissue features by varying the magnetic field during acquisition, at strengths up to 10,000 times lower than conventional fixed-field MRI. The low-field nature of FCI means that it has the potential to be developed towards a variety of accessible and impactful clinical applications. The aim of this preliminary work was to investigate the feasibility of FCI to quantify SVD severity when combined with a fully automated segmentation algorithm.

Methods: An automated segmentation approach has been developed to segment regions of white matter changes associated with SVD from surrounding white matter using R_1 images generated at 0.2 mT from FCI (see Fig. 1). Tissue label masks are created for brain tissue, ventricle, and small vessel disease. The automated approach was written in MATLAB (MathWorks, USA). A constrained k-means clustering based approach was implemented to utilise the inherent contrast between hypointense regions of R_1 corresponding to SVD white matter changes and hyperintense regions of R_1 corresponding to surrounding white matter (see Fig. 1: R_1 map). A multi-step process is used to generate additional tissue masks which are then used to differentiate SVD from cerebrospinal fluid (CSF) regions by accounting for the overlapping isointense R_1 values.

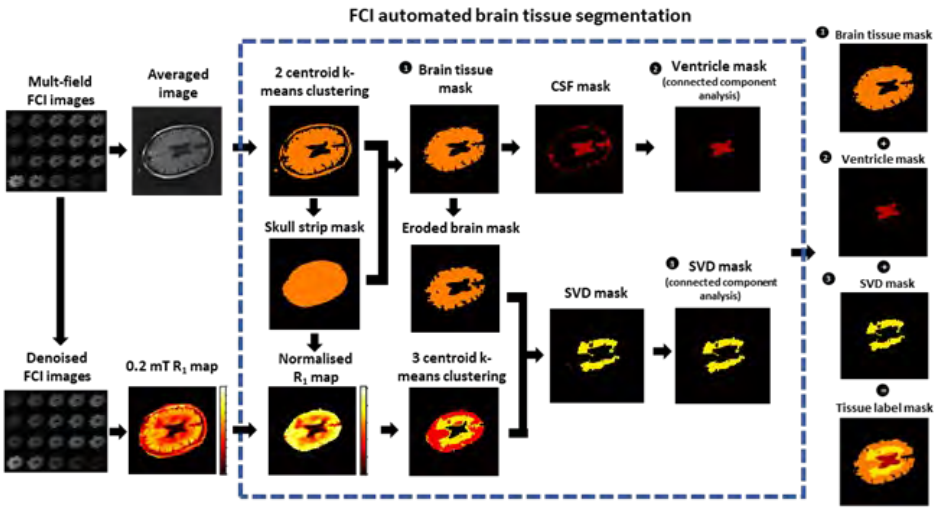

Fig. 1. Automatic segmentation overview: 1) Images are created from multi-field FCI data prior to automated tissue segmentation, 2) automated multi-step approach used to segment different brain tissue regions to extract final brain tissue label image.

The study was approved by the North of Scotland Research Ethics Committee (21/NS/0128). A total of 9 data sets were included from the first patients recruited to the study, who attended an initial 3T MRI (Philips 3T dStream) and FCI scan (N = 6) and repeated scans after 30 days (N = 3).

FCI images were acquired across four evolution fields of 0.2, 2, 20 and 200 mT, 5 logarithmically spaced evolution times, TE of 16 ms, matrix size of 90 x 90, in plane resolution of 3.1 mm, and slice thickness of 10 mm. Prior to generation of R_1 maps at each evolution field, FCI images were de-noised using a pretrained denoising convolutional neural network contained within MATLAB. A separate brain tissue label was generated from 3T MRI data using an existing automated approach to segment regions of white matter hyperintensity [3], and co-registered to FCI images using a landmark-based approach.

Results: Mean and range of Dice coefficients were obtained for brain matter inclusive of SVD (0.89, 0.86 – 0.93), ventricle (0.91, 0.81 – 0.95), and SVD only (0.52, 0.27 – 0.73), (See Fig. 2). Visual inspection of the SVD tissue label shows regions of both false positive and false negative disagreement. A significant Pearson correlation was obtained between SVD brain fractions (R = 0.861, P = 0.003).

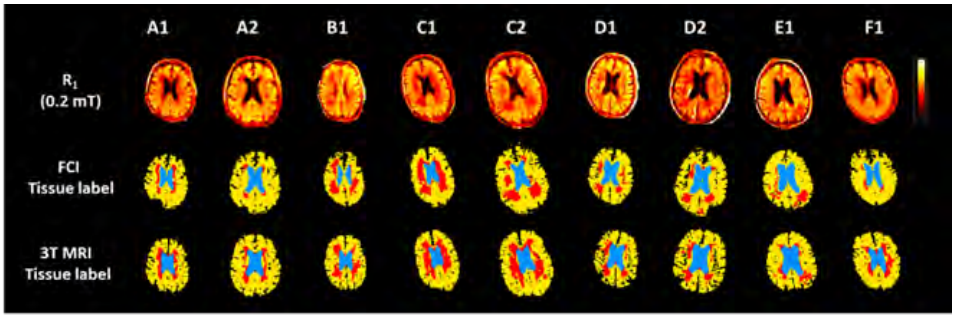

	A1	A2	B1	C1	C2	D1	D2	E1	F1
Dice Coeff. Brain Matter	0.895	0.915	0.867	0.927	0.903	0.882	0.859	0.908	0.891
Dice Coeff. Ventricle	0.915	0.942	0.807	0.920	0.900	0.940	0.946	0.923	0.917
Dice Coeff. SVD	0.667	0.390	0.657	0.732	0.518	0.563	0.512	0.378	0.274

Fig. 2. Comparison of generated tissue labels: A1 and A2 correspond to the initial and repeated scans from a single participant respectively. Row 1) R_1 maps generated at 0.2 mT. Row 2) Tissue label generated from FCI data with brain matter (yellow), ventricle (blue), and SVD (red). Row 3) tissue label generated from 3T MRI data. Row 4-6) Dice coefficients generated from comparison of row 2 and 3 label images for brain matter inclusive of SVD, ventricle and SVD only.

Discussion: FCI combined with an automated segmentation approach has the potential to inform radiological assessment of SVD severity and monitor disease progression. The preliminary results obtained from this study demonstrate the feasibility of FCI to differentiate SVD changes to white matter and inform automated segmentation of these regions. Differences between tissue labels generated from FCI and 3T MRI may partly be underpinned by different sensitivity of imaging approaches to underlying pathophysiological processes involved with SVD changes to white matter [4]. Future work is required to interrogate the sensitivity of FCI to underlying SVD processes and develop further the automated segmentation method presented here.

Conclusions: The preliminary results demonstrate the feasibility of FCI to inform automated segmentation of SVD brain changes and quantification of disease severity.

Acknowledgements: We would like to thank the participants who took part in this study. The study is funded by Chief Scientist Office research grant TCS/19/44. Nicholas Senn's research position is funded by University of Aberdeen Development Trust SCIO Fund.

References

1. L. Østergaard, et al. J Cereb Blood Flow Metab **36**(2), 302-25 (2016). **2.** L.M. Broche, et al. Sci Rep 9, (2019)
3. J.M.J Waymont, et al. J Int Med Res. **48**(2) (2020). **4.** M.S. Stringer, et al. Transl. Str. Res. **12**, 15–30 (2021)

PT1-6

Breast cancer imaging at low and ultra-low magnetic fields using Field Cycling Imaging: a clinical pilot study

Vasiliki Mallikourti[1], P. James Ross[1], Oliver Maier[2], Katie Hanna[3], Ehab Husain[4], Gareth R. Davies[1], Gerald Lip[4], Hana Lahrech[4], Yazan Masannat[5],6, Lionel M. Broche[1]

[1]Aberdeen Biomedical Imaging Centre, University of Aberdeen;
[2]Institute of Medical Engineering, Graz University of Technology, Graz, Austria
[3] Institute of Medical Sciences, University of Aberdeen
[4]University Grenoble Alpes, Inserm U1205, BrainTech Lab
[5]Breast Unit, Aberdeen Royal Infirmary
[6]School of Medicine, Medical Sciences and Nutrition, University of Aberdeen

Introduction: Standard clinical MRI in breast cancer has limitations in determining the tumour subtypes, and cannot detect tumour cell infiltration generally localised in tumour margins. Field-Cycling imaging (FCI) [1,2] is a novel modality that can image over a range of low magnetic field strengths through rapid switching between magnetic field levels. This allows measuring the field-depended changes of the longitudinal T_1 relaxation time (or $R_1=1/T_1$), known as nuclear magnetic relaxation dispersion (NMRD). NMRD profiles provide information on molecular dynamics exploiting novel biomarkers that recently have been shown in breast cancer and glioma models related to tumour invasion migration [3,4]. The goal of this clinical study is to define the specificity of FCI as medical imaging modality in breast cancer diagnosis and its precision in tumour delineation.
Methods: Twenty-six females with breast cancer were recruited from January 2019 to March 2022 (ethics approved by NoSREC, number 19/NS/0064). Ten patients completed the study and were diagnosed with Invasive Ductal Carcinoma (n=1), Ductal Carcinoma In Situ (DCIS, n=5), borderline phyllodes (n=1) and mixed phenotypes (n=3). One patient presented two distinct lesions at histology and each lesion was treated separately for the analysis (n=11 data in total).
FCI was performed with four evolution fields (200, 65.8, 22 and 2.3mT) using a single-slice inversion recovery spin echo sequence with five evolution times. The slice thickness was set to 10mm and the in-plane resolution to 2 to 4mm, depending on the FOV with matrix size of 128x128. The total duration of the FCI examination was 45min. Clinical imaging including ultrasound, mammography, and in some cases MRI at 1.5T were used for comparison. Histology analysis was considered here as gold standard imaging and was used for validation. Tumour sizes in FCI images were calculated using ImageJ. Tumour sizes were compared to histology, using the ratio of tumour size from image divided by tumour size from histology and reported in %.
Data analysis was done in MATLAB using in-house software [5]. R_1 quantification was obtained using the exponential model derived from the Bloch equations. The R_1 NMRD profiles were fitted using a power law model ($1/T_1=\alpha B^{-\beta}$) to derive the slope of the dispersion (β parameter) at fields below (β_L) and above (β_H) 22 mT. The amplitude of the quadrupolar peak at 65.8mT was estimated by subtracting the baseline provided from interpolation following the power law model. NMRD dispersions were extracted from three ROIs: tumour from the diseased breast, adipose and glandular breast tissue from the contralateral breast.
Results: The tumour region measured by FCI exhibited hyper-intense regions at low field strengths (Fig.1). FCI tumour sizes were found close to those obtained from histology (size measurement from histology: 37.0 ± 12.0, measurement ratio: 88.3±42.8% in mammography, 55.6 ± 42.7% in US, 92.6 ± 32.5% in MRI, 101.9 ± 20.1% in FCI). This was not the case for the other imaging modalities for which 6 out of 8 DCIS cases were severely under-estimated.
Tumour R_1 values were significantly lower from glandular and adipose tissue ($p<0.05$). The R_1 contribution from ^{14}N-^{1}H quadrupolar coupling at 65.8 mT was significantly larger in tumours than in adipose breast tissues (0.85 ± 0.44 VS -0.07 ± 0.49, $p<0.001$) (Fig.2a).

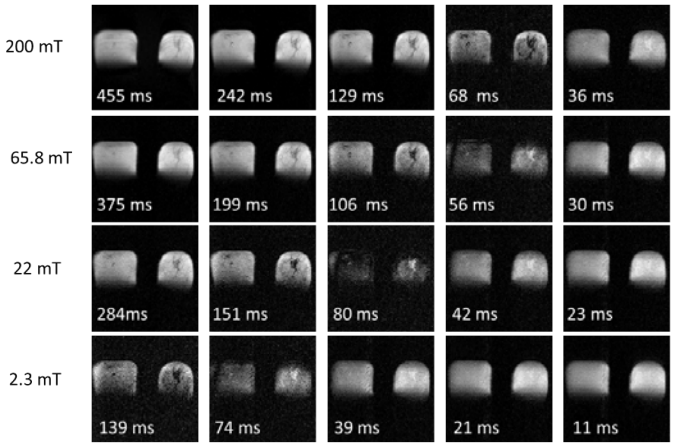

Fig. 1. **Typical FCI data** from a patient presenting with invasive lobular carcinoma mixed with DCIS. The evolution times are reported in ms along the columns and the evolution fields in mT along the rows.

Further segmentation of the tumour NMRD profiles showed significant differences between invasive and non-invasive tumours (Fig. 2b). These appear both in R_1 values at 2.3 mT (9.6 ± 1.8 in non-invasive vs 6.3 ± 2.4 in invasive, $p<0.05$) and in the low-field slope β_L of the R_1-NMRD (0.17 ± 0.07 in non-invasive vs 0.06 ± 0.08 in invasive, $p<0.05$.

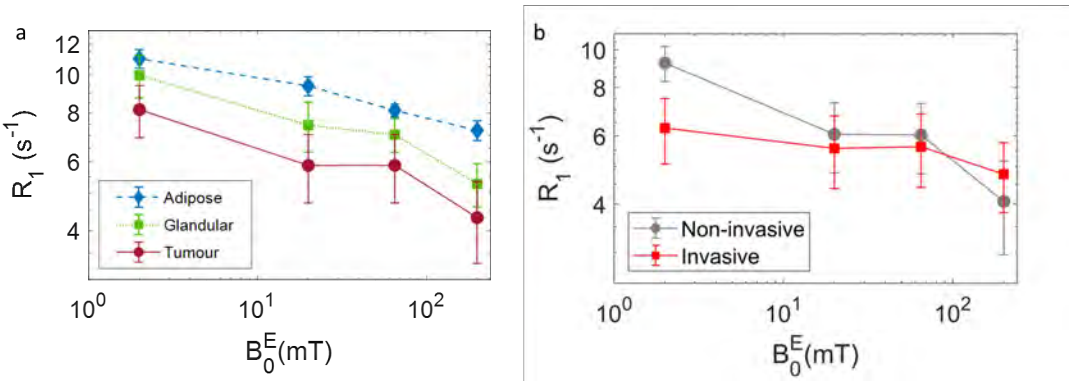

Fig. 2. Averaged R_1-NMRD for (a) all the patients (n=10), with ROIs taken in the adipose tissues (blues), glandular tissues (green) and tumours (red), and for (b) the ROIs in tumours, where invasive (n=4) and non-invasive tumours (n=6). are separated.

Discussion This is the first time that R_1-NMRD profiles are extracted from *in vivo* breast cancer patients. Despite the low spatial resolution, FCI located accurately the lesions and provided non-biased size estimates, as validated by histology. R_1- NMRD profiles successfully discriminated between tumours and healthy tissues. The slope of the dispersion and R_1 at 2.3 mT discriminated between invasive and non-invasive tumours suggesting rapid transmembrane water exchange and water molecular dynamics in case of invasion [3].

Conclusions: FCI shows high potential for breast tumour detection without contrast agent with potentially better delineation in DCIS. We also found potential biomarkers of breast cancer invasiveness, which is of high interest for surgery planning and could improve the outcome of patient treatment if confirmed.

References

[1] Lurie, D.J. et al. *Cr Phys*. **11**, 136-148 (2010), [2] Broche LM, et al. *Sci. Rep*. **9**(1):10402 (2019)., [3] Petit M, et al. *NMR Biomed*. **35**(6):e4677 (2022),[4] Ruggiero MR, et al. *Cancers* (Basel). **14**(17):4180 (2022),
[5] Broche LM, at al. *Magn. Reson. Imaging*.44:55-5 (2017).

PT1-7

African Experience with Ultra-low Field MRI on the REVAMP-TT Study: A Malawian perspective from a Nurse-Midwife and GATES-ISMRM UNITY Mentee

Harriet Kammayani [a], Maclean Vokhiwa [a], Saidon Banda [a], Adrian Tang [b]

a Training and Research Unit of Excellence, Blantyre, Malawi; Department of Public Health, School of Public and Global Health, Kamuzu University of Health Sciences, Blantyre, Malawi.

[b] Tangoscan Inc, Manchester, UK

Introduction: Infants born preterm, small for gestational age, or who face malnutrition, neglect, or other forms of adversity are at risk for delayed, impaired, or sub-optimal neurodevelopment. These risks are disproportionately represented in low- and middle-income countries such as Malawi where the availability of neuroimaging with conventional high field MRI scanners is extremely sparse. The very recent development of ultra-low field mobile scanners which are powered off standard domestic ring-mains power offers an affordable, scalable method for directly evaluating the efficacy of interventions to improve infant and child health and neurodevelopment [1]. ISMRM is collaborating with the Bill and Melinda Gates Foundation to optimise the design, implementation, and distribution of one such device specifically for use in low- and middle-income countries [3]. To facilitate these aims, a Mentor programme was introduced at the 2023 Annual Meeting in Toronto. We present and share the experience of one of these Mentees who is a nurse with additional midwife expertise and who routinely uses ultra-low field MRI to image infants in Malawi in the context of the REVAMP-TT trial [2,4,5]

Methods: The randomized controlled trial of the effect of intravenous iron on anaemia in Malawian pregnant women (REVAMP) is a two-arm confirmatory individually randomised trial set in Blantyre and Zomba districts in Malawi. The trial will randomise 862 women in the second trimester of pregnancy with a capillary haemoglobin concentration below 100.0 g/L. The study comprises two arms: (a) intravenous FCM (20 mg/kg up to 1000 mg) given once at randomisation, and (b) standard of care oral iron (65 mg elemental iron two times per day) for 90 days (or the duration of pregnancy, whichever is shorter) provided according to local healthcare practices. Recruited patients have neuroimaging as part of the neurodevelopment sub-study to provide baseline data from which to evaluate the effects of intervention.

Results: Study cohort includes 3- and 12-months old sleeping babies/infants. Harriet's roles with these babies and their mothers are diverse including: Obtaining Informed consent from participant to undergo MRI scanning. Signing consent forms for all the participants undergoing MRI. Assuring the mothers on the safety of the Hyperfine Machine. Preparing the babies to undergo scanning by putting them in a meg-vac immobilizer and conducting MRI Scans [Fig 1]. Positioning the babies in the Hyperfine Machine. Uploading the images after MRI assessment Assisting in EEG Assessment. Follow up on participants who missed the scheduled assessments. Completion of hard copy of case report forms after every procedure.

Discussion: Early experience with Hyperfine swoop was presented at the ISMRM-UNITY meeting in Toronto 2023 ISMRM annual meeting via results from an online questionnaire conducted by PATH [6]. Harriet's own experience adds significant and specific detail to this from a Malwian perspective with specific challenges identified as: Putting babies to sleep to conduct the MRI scans since we do not sedate them. The machine produces a loud noise which wakes the babies making it difficult to continue with the scans. The machine does not have power backup of which a minor power interruption causes the need to repeat the scan. Coil design is closed and does not allow ventilation which causes the babies to wake up. Getting used to the scanner and full training since it is a new machine to be used in Malawi.

Fig. 1. Patient positioning on the Hyperfine Swoop

Conclusions: Although Harriet was unable to take advantage of her funding to attend ISMRM 2023 (Toronto) in person, the UNITY mentor-mentee relationship has enabled her to share her experience with her mentor in the UK and through this collaboration, to submit the same experience to a wider audience through conference presentations in the UK and extend such collaboration and mutual exchange.

References

[1] https://hyperfine.io/about/partnerships
[2] https://true.mw/revamp-tt/
[3]https://www.kcl.ac.uk/news/europes-first-game-changing-portable-mri-machine-arrives-at-kings-health-partners
[4] Mwangi MN, Mzembe G, Moya E, Braat S, Harding R, Robberstad B, Simpson J, Stones W, Rogerson S, Biselele K, Chinkhumba J, Larson L, Ataíde R, Phiri KS, Pasricha SR. Protocol for a multicentre, parallel-group, open-label randomised controlled trial comparing ferric carboxymaltose with the standard of care in anaemic Malawian pregnant women: the REVAMP trial. BMJ Open. 2021 Nov 23;11(11):e053288. doi: 10.1136/bmjopen-2021-053288. PMID: 34815287; PMCID: PMC8611444.
[5] Pasricha SR, Mwangi MN, Moya E, Ataide R, Mzembe G, Harding R, Zinenani T, Larson LM, Demir AY, Nkhono W, Chinkhumba J, Simpson JA, Clucas D, Stones W, Braat S, Phiri KS. Ferric carboxymaltose versus standard-of-care oral iron to treat second-trimester anaemia in Malawian pregnant women: a randomised controlled trial. Lancet. 2023 May 13;401(10388):1595-1609. doi: 10.1016/S0140-6736(23)00278-7. Epub 2023 Apr 21. PMID: 37088092; PMCID: PMC10193370.
[6] https://www.linkedin.com/in/jaclyn-dela-rosa-2572b57/

PT2-1

Exploring the Potential of Quantitative Susceptibility Mapping (QSM) to Predict Plaque Rupture Risk: Ex Vivo Human Carotid Atherosclerotic Plaque QSM Pipeline Optimisation

Francesco Digeronimo[a,b], Brooke Tornifoglio[a,b], Alan J. Stone[c], Karin Shmueli[d], Caitríona Lally[a,b,e]

[a]Trinity Centre for Biomedical Engineering, Trinity College Dublin, Dublin, Ireland.
[b]Department of Mechanical, Manufacturing and Biomedical Engineering, Trinity College Dublin, Dublin, Ireland.
[c]Department of Medical Physics and Clinical Engineering, St. Vincent's University Hospital, Dublin, Ireland.
[d]Department of Medical Physics and Biomedical Engineering, University College London, London, United Kingdom.
[e]Advanced Materials and Bioengineering Research Centre (AMBER), Royal College of Surgeons in Ireland and Trinity College Dublin, Dublin, Ireland.

Introduction: Carotid artery disease (CAD) is a high-risk factor for acute ischaemic stroke (AIS), with plaque rupture estimated to account for 15-20% of AIS cases [1]. Current CAD clinical assessment relies on the quantification of stenosis percentage, an anatomical measure which may be insufficient to predict rupture risk [2]. Quantitative susceptibility mapping (QSM) can reconstruct magnetic susceptibility (χ) distribution maps via physics-based post-processing of the phase component of the MRI signal [3]. In porcine arterial tissue, χ is sensitive to the presence of collagen: a critical load-bearing microstructural component which may play a key role in plaque stability [4-5]. High-resolution and accurate plaque QSM can facilitate investigations into tissue microstructure which could inform rupture risk. However, robust QSM of heterogeneous tissues, such as atherosclerotic plaques, is challenging due to large intra- and inter-sample composition variability and the presence of both low-signal regions and strong χ sources. The quality and accuracy of χ maps is heavily influenced by the processing pipeline used [6]. Therefore, this study focused on optimising a QSM pipeline for *ex vivo* human carotid atherosclerotic plaque images acquired using an ultra-high field system.

Methods: Fresh atherosclerotic plaques (n=7) were obtained from carotid endarterectomy surgeries at St. James's Hospital, Dublin and cryopreserved. After thawing, specimens were imaged individually using a 7T system, with specifications and protocol summarised in Table 1. The samples presented in this study are part of a larger dataset, for which diffusion tensor imaging, mechanical and histological characterisation results were previously published [7]. Three plaques at different American Heart Association defined disease stages, type II, IV, and VI [8], were chosen for the QSM pipeline optimisation to account for morphological variability. A Two-Pass Masking (TPM) pipeline was used for QSM [9], see Fig. 1(a). Initial pipeline settings were defined based on a previous study [4]. The effects of different algorithms and settings were evaluated individually in a step-by-step process see Fig. 1(b). Where a particular method or parameter provided significant improvements in terms of reductions in streaking artefacts (SAs) and/or residual background fields (RBFs), the pipeline was adjusted to include this setting before proceeding to the next step. For example, Laplacian phase unwrapping performed best and was therefore adopted for all subsequent evaluations. For each step, images at each stage of the QSM pipeline were visually analysed and compared. χ difference maps were also compared for noise masking.

Table 1. Data Acquisition Specifications

IMAGING SET-UP	**Container**	15 mL Falcon Tube
	Temperature [°C]	20
	Surrounding Environment	Fresh Phosphate Buffered Saline (PBS)
SYSTEM SPECIFICATIONS	**Manufacturer**	Bruker (Ettingen, Germany)
	Model	BioSpec 70/30 USR
	Field Strength [T]	7
	Bore Type	Horizontal
	Bore Diameter [cm]	30
	Number of Coil Channels	8
ACQUISITION PARAMETERS	**Sequence Type**	T_2^*-w 3D Multi-Echo GRE
	Averages	4
	Echoes	4
	Repetition Time [ms]	150
	1st Echo Time [ms]	4.8
	Echo Spacing [ms]	7.68
	Flip Angle [°]	30
	Field of View [mm]	16 x 16 x 16
	Matrix Size [voxels]	128 x 128 x 128
	Resolution [µm]	125 x 125 x 125
	Acquisition Time	2 h: 44 min

Results: Optimisation results are summarised in Fig. 1(b) below. Using the mean of the inverse noise map distribution as the noise masking threshold provided the least amount of SAs and no visible discontinuities. Mask erosion caused unwanted map discontinuities without reducing SAs. Both PRELUDE 3D and Laplacian were able to successfully unwrap the images; however, Laplacian was much faster. PRELUDE 2D showed signal discontinuities in higher-noise regions. LBV outperformed PDF and SHARP, with no visible RBFs. MEDI and Iterative Tikhonov both showed minimal SAs for the type II and IV datasets, but Iterative Tikhonov was more stable with the higher-noise (type VI) dataset.

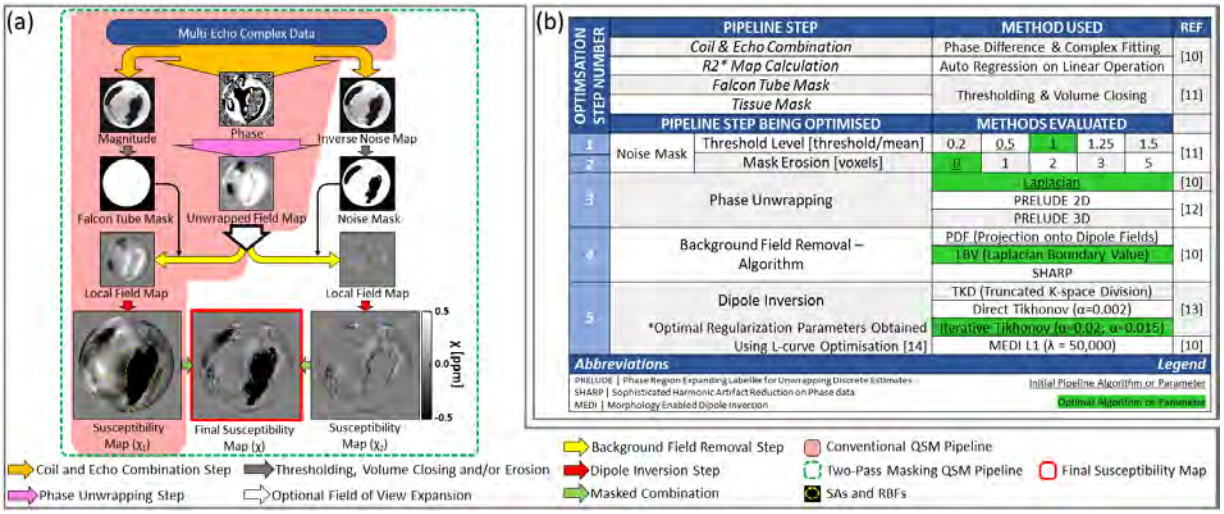

Fig. 1. Overview of methods and results: (a) TPM QSM pipeline overview. Conventional [10] vs TPM pipeline. Central axial slice of a plaque is shown for each step. TPM reduces SAs and RBFs; (b) Overview of optimisation steps summarising algorithms and parameters explored as well as final pipeline [10-14].

Discussion: The TPM QSM pipeline used provided noticeable SA reduction and was computationally efficient, specifically for an advanced type VI plaque [9]. Increasing the noise mask threshold level reduced the level of SA caused by low-signal regions; however, if the threshold was set too high the χ map presented large discontinuities as the mask was not solely localised to the regions of high-noise. As previously reported in the literature, Laplacian provided more stable and computationally efficient unwrapping compared to PRELUDE, most notably for the advanced plaque [15]. Using the presented pipeline, optimised for *ex vivo* plaques at various stages of disease, the χ values within fibrous tissue, calcification and intra-plaque haemorrhage are comparable to available data in the literature [16].

Conclusions: A robust QSM pipeline was developed for the analysis of *ex vivo* human carotid atherosclerotic plaque. The pipeline and optimisation process developed in this study are transferrable for other *ex vivo* QSM studies involving heterogeneous tissues. Current work is focusing on investigating the χ maps in the context of mechanically relevant microstructural components which could be improved biomarkers for 'vulnerable' plaques.

Acknowledgements: This project is funded by the Centre for Doctoral Training in Advanced Characterisation of Materials and Science Foundation Ireland under award REF: 18/EPSRC-CDT/3581.

References: [1] S. Dossabhoy, et al. Seminar Vasc Surg. **34**(1), 3-9 (2021). [2] L. Saba, et al. JVS Vascular Science. **2**, 149-158 (2021). [3] K. Shmueli, Quantitative Susceptibility Mapping, in N. Seiberlich, et al., Advances in Magnetic Resonance Technology and Applications, V1:819-838, Academic Press, Cambridge, MA (US), 2020. [4] A. J. Stone, et al. Magn Reson Med. **86**(5), 2512-2527 (2021). [5] R. D. Johnston, et al. Acta Biomater. **124**, 291-300 (2021). [6] QSM Challenge 2.0 Organization Committee, et al. Magn Reson Med. **86**, 1241-1255 (2021). [7] B. Tornifoglio, et al. Biomech Model Mechanobiol. (2023). [8] H. C. Stary, et al. Circulation. **92**(5), 1355-74 (1995). [9] A. Karsa and K. Shmueli, ISMRM Annual Meeting Abstract Number: 2462, London, 2022.[10] MRI Research Lab Cornell. MEDI toolbox: http://weill.cornell.edu/mri/pages/qsm.html. [11] MATLAB: Image Processing Toolbox. [12] FSL PRELUDE: http://fsl.fmrib.ox.ac.uk/fsl. [13] MRI Group, University College London. Susceptibility Calculation Methods: https://xip.uclb.com/product/mri_qsm_tkd. [14] P. C. Hansen, et al. SIAM SISC. **14**(6), 1487-1503 (1993). [15] S. D. Robinson, et al. NMR in Biomedicine. **30**(4), 3601 (2017). [16] M. Azuma, et al. AJNR Am J Neuroradiol. **41**(2), 310-317 (2020).

PT2-2

Magnetic resonance imaging measurement of colon length in adults with functional constipation and healthy controls

Faiz Alqarni[1,2,3], Caroline L. Hoad[4], Robin C. Spiller[1,2], Penny A. Gowland[4], Moira Taylor[5], Guru Aithal[1,2] and Luca Marciani[1,2]

[1] Translational Medical Sciences, Nottingham Digestive Diseases Centre, School of Medicine, University of Nottingham
[2] National Institute for Health and Care Research (NIHR) Nottingham Biomedical Research Centre, Nottingham University Hospitals NHS Trust, and University of Nottingham
[3] King Saud medical city, ministry of Health, Saudi Arabia
[4]Sir Peter Mansfield Imaging Centre, School of Physics and Astronomy, University of Nottingham
[5] School of Life Sciences, University of Nottingham

Background:
Over the last few years, gastrointestinal (GI) magnetic resonance imaging (MRI) has provided unprecedented insights into functional gastrointestinal diseases (FGIDs), with much more still to be discovered. Despite this organ's relatively large size and pathophysiological significance, MRI of colonic function remains a largely unexplored area. Recent work from our group has investigated colon volumes and motility in adult functional constipation (FC) but very little is known about colon length in health and FC. We aimed to develop colon length measurements and hypothesised that there would be differences in total and regional colonic length between adults with functional constipation and healthy controls.

Methods:
The colon length measurement methods were developed on the commercial platform Enterolytics provided by UK specialist company Motilent, with whom we collaborate. Briefly, the colon was visualised in a three-dimensional space, and the operator manually defined the centre line of each segment (ascending, transverse, descending and sigmoid) (Fig1), which was then quantified. A retrospective series of MRI images were then retrieved [1, 2]. The MRI scans were taken at the morning baseline after an overnight fast. Images were acquired using a whole-body 1.5T scanner (Achieva, Philips Medical System, Best, The Netherlands) in the supine position, using a 16-element abdominal coil. A coronal dual-echo gradient echo sequence was used. It acquired 24 contiguous slices with one expiration breath hold of 15 s (TR / TE1 / TE2 = 157 / 2.30 / 4.60 ms, 256 × 256 reconstructed matrix, voxel size 1.76 × 1.76 × 7 mm 3). The set was acquired with an expiration breath-hold of approximately 13 seconds. The participants from those studies attended repeated visits, thus also allowing assessment of individual colon length variability between visits. The MRI scans covered the entire undisturbed, unprepared colon. Preliminary results presented here are from n=20 adult participants, of whom n=15 were patients with FC and n=5 were healthy controls. Intra-operator variability was first assessed by measuring colon segments on the same datasets six times on different occasions. Intra-operator and intrasubject variability were appraised by using the coefficient of variation (CoV). The CoV is commonly used, and low values (e.g. less than 10%) are generally accepted as reflecting a dependable and sufficiently consistent measurement. Secondly, all colon segments were measured in both groups and compared.

Results:
The intra-operator CoV for total colon length was 2% and ranged between 2% and 6% for individual colon segments. The CoV for intraindividual variability between repeated visits was higher, with an average of 4% for total colon length and between 5% and 19% for individual colon segments. Total

colon length in patients with FC was significantly longer, 114±23cm (mean±SD), than in healthy controls, 88±9 cm, $p<0.05$.

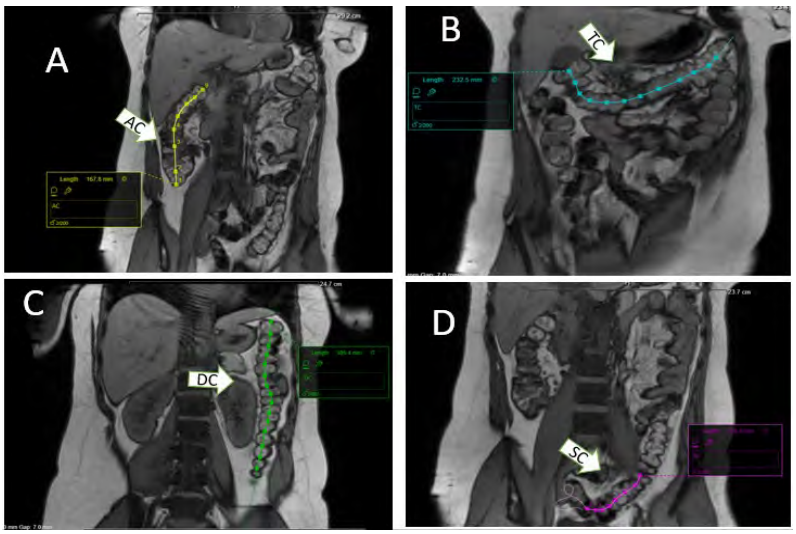

Fig.1. Measurements of separate colon anatomical segments (A, is ascending colon (AC); B, transverse colon (TC); C, descending colon (DC) and D, sigmoid colon (SC)). The figure displays one image plane of the multislice stack with the three-dimensional measuring line overlayed.

Discussion:
This initial work was successful and showed that the new colon length measure was accurate and that participants' physiological variability between different days was higher than the intra-operator variability, most likely reflecting a natural variation of colon lengths across different days. All colon segments were longer in constipated patients. The rectal region proved to be more difficult to assess and optimised imaging could mitigate this difficulty. Future work will add further data to this initial series and will also develop better MRI scanning protocols to help three-dimensional visualisation of the more distal colon, which could allow for more accurate measurements.

Conclusion:
New colon length information together with other measurable endpoints such as colon volumes and transit in FC may help improve our understanding of functional gut diseases and the mode of action of drugs.

References
1. Gunn, D., et al., Psyllium reduces inulin-induced colonic gas production in IBS: MRI and in vitro fermentation studies. Gut, 2022. 71(5): p. 919-927.
2. Krishnasamy, S., et al., Processing apples to puree or juice speeds gastric emptying and reduces postprandial intestinal volumes and satiety in healthy adults. The Journal of nutrition, 2020. 150(11): p. 2890-2899.

PT2-3

Identification of Distinct Prognostic Groups of Paediatric Brain Tumours using Unsupervised Learning

Timothy Mulvany[a], Daniel Griffiths-King[a], Lara Worthington[b,c], Richard Tunney[a], Theodoros N Arvanitis[b,d], Andrew Peet[b,d], John Apps[b,d], Jan Novak[a]

[a] Aston University, College of Health and Life Sciences, Birmingham, England
[b] Birmingham Children's Hospital, Department of Oncology, Birmingham, England
[c] University Hospital Birmingham NHS Foundation Trust, RRPPS, Birmingham, England
[d] University of Birmingham, Institute of Cancer & Genomics Sci, Birmingham, England

Introduction: Central nervous system (CNS) tumours account for 25% of all paediatric cancer cases in England [1] and have the highest mortality rate of any group of childhood tumours with a 5-year survival rate of 74% in England [1]. Predicting prognosis in paediatric brain tumours is a complex problem due their high degree of biological variability and heterogeneity, the patient's overall health and stage of development, and a variety of possible treatment paths. Increased data availability and the rich nature of MRI have incentivised the combined use of radiomics and machine learning in medical image analysis to tackle this problem. Previous studies have shown the power of radiomics and machine learning in predicting diagnosis in childhood brain tumour [2, 3, 4], and has seen some success in predicting prognosis with multi-modal MRI [5, 6]. This study aims to evaluate the prognostic performance of unsupervised learning methods in the context of childhood brain tumours, focusing specifically on the combination DWI features with patient demographics.

Methods: This study utilised retrospective clinical data from 84 paediatric brain tumour patients with long term-survival information made available via the Children's Cancer & Leukaemia Group's long term functional imaging study established in 2004 [7]. A set of 24 first order radiomic features were extracted from ADC maps, generated using DWI data acquired at 1.5T across four scanners located at Birmingham Children's Hospital using two b-values of 0 and 1000 s/mm^2. Features were generated using the whole tumour regions of interest specifically excluding cystic tissue and oedema. Additionally, survival status, age at diagnosis and gender were collected from patient records. The data is comprised of 41 male and 43 female patients, with an age range at diagnosis of 0.33 to 16.3 years. 19 patients were deceased as a direct result of tumour progression with all others still alive.

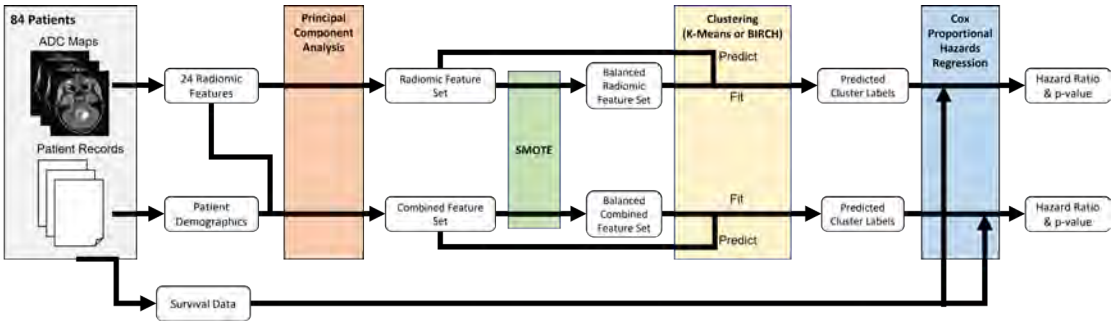

Fig. 1. Data workflow showing the various stages of data processing, clustering and survival analysis

Fig. 1 outlines the workflow for constructing two dimensionality-reduced feature sets, each class-balanced and fed into clustering models. The resulting cluster predictions were then evaluated to determine the prognostic significance of fitted clusters. Dimensionality reduction was performed using Principal Component Analysis (PCA) with 6 components explaining 95% of variance. K-Means and Balanced Iterative Reducing and Clustering using Hierarchies (BIRCH) clustering models were each initialised to find 2 clusters. Models were fitted using the Synthetic Minority Over-sampling Technique (SMOTE) balanced feature sets to compensate for class imbalance and evaluated using the unbalanced feature sets. Hazard Ratios were calculated using Cox Proportional Hazards Regression.

Results: K-Means clustering was unable to identify any significant groups. BIRCH successfully identified two clusters with significant prognostic value ($p<0.05$) for both feature sets. With ADC features alone, this method distinguished two clusters of notably different risk, obtaining a hazard ratio of 4.71($p=0.0383$). With the inclusion of patient demographics, the resulting hazard ratio is raised to 9.83 ($p=0.0262$). The Kaplan Meier curves in Fig. 2 show the long-term survival for each set of clusters found using BIRCH.

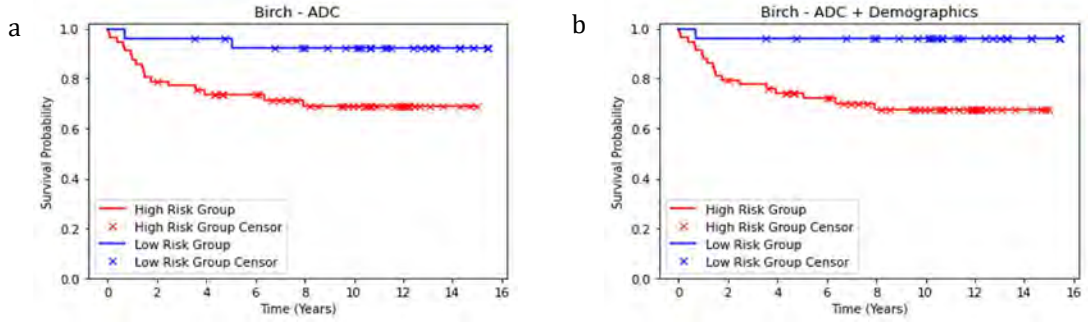

Fig. 2. Kaplan Meier curves showing long term survival for each set of groups found through BIRCH clustering of a) radiomic feature set, b) radiomic + patient demographic feature set.

Discussion: BIRCH identified two significant prognostically divergent clusters in both feature sets, with the inclusion of age at diagnosis noticeably improving risk differentiation. This established existence of two divergent patient groups through unsupervised methods alone, implies an unexplored underlying relationship between prognosis and the distribution of extracted features warranting further investigation. The failure of K-Means clustering may be a result of overdependence on outliers and instability near cluster of resulting clusters. This study did not enforce a minimum survival threshold or set diagnosis criteria during patient selection, each of which may have increased complexity of prognostic trends, yet significant prognostic groups were still identified exhibiting the potential of simple first order radiomics in a complex and noisy prediction space in.

Conclusions: ADC radiomic features have been shown to provide prognostically powerful and statistically significant results, identifying low and high-risk patient groups. Further validation with larger datasets is required to evaluate the generalisability of these findings. Correlation with pathological diagnosis, histopathological characteristics and WHO tumour grade will be important to determine underlying physical mechanisms and the potential added value of identification of adverse radiomic features in low grade tumours and good prognosis radiomic features in high grade tumours. It has also been shown that demographic features such as age at diagnosis can act as powerful aids to radiomic features for prognostic prediction, improving the differentiation between low and high-risk paediatric patients.

References

[1] L. Irvine and C. Stiller, “Childhood Cancer Statistics, England,” Public Health England, 2018.
[2] J. T. Grist, “Distinguishing between paediatric brain tumour types using multi-parametric magnetic resonance imaging and machine learning: A multi-site study,” NeuroImage: Clinical, 2020.
[3] J. Novak, “Classification of paediatric brain tumours by diffusion weighted imaging and machine learning,” Scientific Reports, vol. 11, no. 1, p. 2987, 2021.
[4] G. Cui, “Machine-learning-based classification of Glioblastoma using MRI-based radiomic features,” in Medical Imaging 2019: Computer-Aided Diagnosis, 2019.
[5] M. Wilson, “Magnetic resonance spectroscopy metabolite profiles predict survival in paediatric brain tumours,” European Journal of Cancer, vol. 49, no. 2, pp. 457-464, 2013.
[6] J. Grist, “Combining multi-site magnetic resonance imaging with machine learning predicts survival in pediatric brain tumors,” Scientific Reports, vol. 11, no. 1, p. 18897, 2021.
[7] CCLG, “Childhood Cancer and Leukaemia Group,” [Online]. Available: https://www.cclg.org.uk/.. [Accessed 2023].

PT2-4

T1 Dark, Bright or Fright? : Clinical Fat Saturation techniques in the lateral neck from a Medicolegal perspective

Sunthus Amrez[a], Adrian Tang[a]

[a] Faculty of Biology, Medicine and Health, The University of Manchester

Introduction: Unlike in some areas of the body eg. Liver and kidney, cystic lesions in the lateral neck are rarely simple and not infrequently malignant. Ultrasound is often the first modality used to investigate lumps in the head and neck at which unilocular lipoma and simple cysts can look similar [1] In such cases, characterisation of such lesions would typically defer to MRI with which discrimination of fat and water is typically trivial and unequivocal [3]. This poster presents an incidental lesion in the lateral neck first and mistakenly described as fat which several years later led to medicolegal proceedings. A brief review of contrast mechanisms in complex cystic lesions of the lateral neck is made along with a summary of different fat suppression techniques available to clinical radiologists and their relative strengths and weaknesses.

Methods: Anonymised case presentation of a focal lesion in the lateral neck with imaging from index MRI at which it was presumed to be fat-containing. Subsequent clinical evolution and imaging with repeated ultrasound, CT then repeat MRI with review of the original MRI sequences illustrating a clinical pitfall when using inversion recovery to supress fat in complex cystic lesions.

Results: An incidental left lateral neck mass was seen at MRI of the brain for unrelated clinical indication. This lesion was located at level 2 in the left lateral neck and hyperintense at T1 with complete suppression at STIR and described unequivocally as a lipoma (Fig 1). Over the next 3 years, the patient received 3 ultrasound scans. The first two were for reasons unrelated to the left level 2 lipoma whose earlier MRI diagnosis was not challenged. Despite identical appearances on a third ultrasound scan, an alternative differential of Branchial cleft cyst was suggested and ultimately confirmed following excision. The patient subsequently made a claim for medicolegal negligence for failing to make the correct diagnosis on the earlier 2 ultrasound scans.

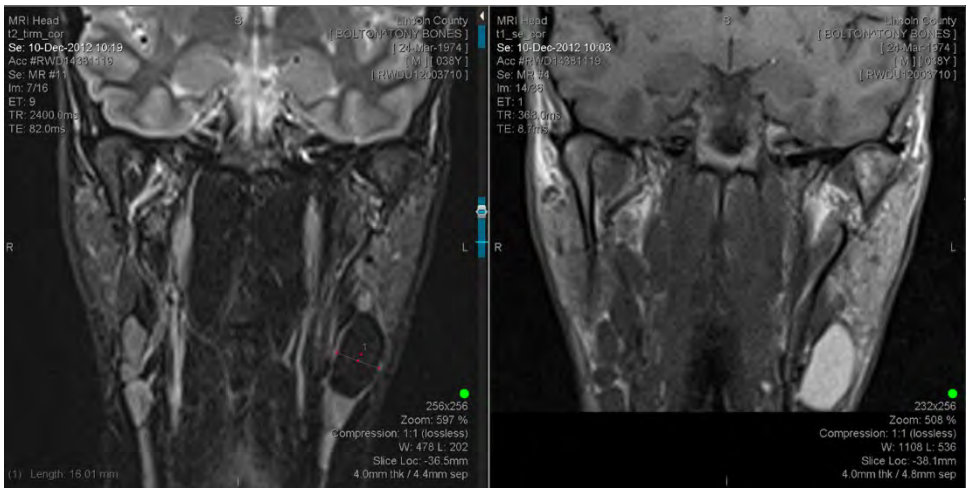

Fig. 1.

Discussion: Cystic lesions in the head and neck are common but are not so often simple and benign that they should be readily dismissed. Pure fat containing lesions are rare in the head and neck but are typically trivial to differentiate with standard clinical MRI sequences such as T1 TSE, STIR and

Chemical Shift Suppression (CHESS). Under certain conditions, fluid containing cysts in the lateral neck can mimic fat on STIR sequences and errors can be made in clinical interpretation can be made if fat specific suppression sequences using chemical shift are not also acquired. Or, if they are acquired but not reviewed when reporting as in the current case. Reporting errors on subsequent ultrasound and CT are reviewed, categorised and discussed along with how these can lead to medico-legal action and how breach of duty is considered and determined when writing expert medical opinion. The additional fact of homogenous hypo intensity on TSE T2 is presented along with suggestions (and invitations) to explain the underlying contrast mechanism accounting for this in vivo [2].

Conclusions: Cystic lesions in the head and neck are common and not infrequently malignant. Some cysts can be complex and lead to mischaracterisation as fat if the incorrect fat suppression technique is used. Often, histological diagnosis requires sampling with fine needle aspiration or excision biopsy [4]. Poor patient outcomes and ensuing medicolegal action is a risk of inaccurate imaging diagnosis which can occur years down the line. We discuss the relative advantages of clinically available fat suppression techniques with MRI, consider and invite hypotheses to explain co-incidental homogenous t2 signal void and review how breach of duty is determined when writing expert witness reports in clinical radiology.

References

[1] Rico F, Hoang D, Lung J, Puccio O, Brito M, Nazim MH, Sbar A. Substernocleidomastoid Muscle Neck Lipoma: An Isolated Case Report. Case Rep Surg. 2019 Jun 19;2019:4936357. doi: 10.1155/2019/4936357. PMID: 31321112; PMCID: PMC6607698.

[2] Kato H, Kawaguchi M, Ando T, Kaneko Y, Hyodo F, Matsuo M. Hypointense head and neck lesions on T2-weighted images: correlation with histopathologic findings. Neuroradiology. 2020 Oct;62(10):1207-1217. doi: 10.1007/s00234-020-02483-z. Epub 2020 Jun 20. PMID: 32562036.

[3] Sira J, Makura ZG. Differential diagnosis of cystic neck lesions. Ann Otol Rhinol Laryngol. 2011 Jun;120(6):409-13. doi: 10.1177/000348941112000611. PMID: 21774450.

[4] Vazquez Salas S, Pedro K, Balram A, Syed S, Kotaka K, Kadivar A, Eke BO, McFarland M, Sung M, Behera N, Dubner BG, Maleki Z. Head and Neck Cystic Lesions: A Cytology Review of Common and Uncommon Entities. Acta Cytol. 2022;66(5):359-370. doi: 10.1159/000525144. Epub 2022 Jun 17. PMID: 35717936.

PT2-5

Liver Magnetic Resonance Imaging, Non-Alcoholic Fatty Liver Disease and Metabolic Syndrome Risk in Pre-Pubertal Mexican Boys

Elizabeth Shumbayawonda[a*], Benito de Celis Alonso[b*], Cayden Beyer[a], Silvia Hidalgo-Tobon[c,d], Briseida López-Martínez[e], Pilar Dies-Suarez[c], Miguel Klunder-Klunder[f], América Liliana Miranda-Lora[g], Eduardo Barragán Pérez[h], Helena Thomaides-Brears[a], Rajarshi Banerjee[a], E. Louise Thomas[i], Jimmy D Bell[i], Po-Wah So[j]

a. Perspectum Ltd., Oxford, UK
b. Faculty of Physical and Mathematical Sciences, Benemérita Universidad Autónoma de Puebla, Puebla, Mexico
c. Imaging Department, Children's Hospital of Mexico Federico Gómez, Mexico City, Mexico
d. Physics Department, UAM Iztapalapa, Mexico City, Mexico
e. Sub direction of Research, Children's Hospital of Mexico Federico Gómez, Mexico City, Mexico
f. Department of Community Health Research, Children's Hospital of Mexico Federico Gómez, Mexico City, Mexico
g. Epidemiological Research Unit in Endocrinology and Nutrition, Children's Hospital of Mexico Federico Gomez, Mexico City, Mexico
h. Neurology Department, Children's Hospital of Mexico Federico Gómez, Mexico City, Mexico
i. Research Centre for Optimal Health, University of Westminster, London, UK
j. Department of Neuroimaging, Institute of Psychiatry, Psychology and Neuroscience, King's College London, London, UK
* Joint first authors

Introduction: Global paediatric obesity rates have tripled in the last 50 years and are closely linked with increasing incidence of non-alcoholic fatty liver disease (NAFLD), non-alcoholic steatohepatitis (NASH) and metabolic syndrome (MetS). Not only is early NAFLD asymptomatic and liver function tests insensitive to mild disease, but assessment by liver biopsy has increased risk of complication in children. Multiparametric MRI (mpMRI) metrics of liver fat (proton density fat fraction [PDFF]) and disease activity (fibro-inflammation, iron-corrected T1 [cT1]) can characterise and monitor chronic liver disease, but hitherto, have not been used to investigate BMI, NAFLD and MetS relationships in young pre-pubertal children with potentially asymptomatic disease. Male Hispanic populations tend to have both a higher prevalence of NAFLD/NASH and a greater likelihood of developing cirrhosis. Our aim was to determine the clinical usefulness of mpMRI for assessing NAFLD in asymptomatic male Hispanic children who are at risk of having or developing advanced liver disease.

Methods: Pre-pubertal boys (n=81) aged 7 to 9 years of varying Body-Mass Index (BMI) (: 17.4 ± 3.5 kg/m^2) were recruited in Mexico City. Anthropometric, plasma metabolic and liver health data were collected prior to non-contrast mpMRI at 3T Shortened modified look-locker inversion (shMOLLI) and multi-echo spoiled gradient-echo sequences were used to measure liver T1 and iron/PDFF, respectively [1]. PDFF was calculated using IDEAL, and cT1 following correction for iron using T2*. Non-parenchyma structures such as bile ducts, large blood vessels and image artifacts were excluded from image analysis. MetS risk was assessed using the Identification and prevention of Dietary- and lifestyle-induced health EFfects In Children and infantS' (IDEFICS) criteria. Participants were trichotomised into three groups: NAFLD, PDFF ≥5%; NASH, PDFF ≥5% and cT1 ≥800ms; and high-risk NASH (NASH score of ≥4 and fibrosis stage (F) ≥2), PDFF ≥5% and cT1 ≥875ms [2].

Results: At recruitment, and prior to the non-contrast mpMRI scan (**Fig 1**), all participants were asymptomatic and did not have any reported/existing liver disease. Most children (81%) had liver transaminases within the normal upper limit, 38% had high BMI and 14% had ≥3 MetS risk factors.

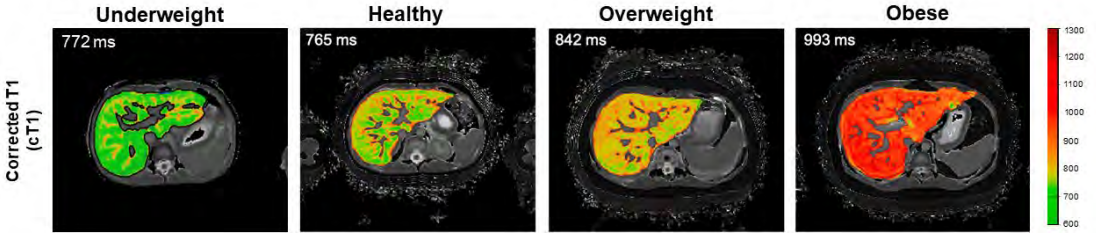

Fig. 1. *Typical transverse corrected T1 (cT1) maps for underweight, healthy, overweight and obese participants calculated from multiparametric magnetic resonance imaging (mpMRI) data collected using LiverMultiScan (Perspectum Ltd, Oxford, UK) image acquisition protocol and MRI scanning sequences.*

Applying mpMRI thresholds, 12%, 7% and 4% had NAFLD, NASH and high-risk NASH respectively. Participants with ≥3 MetS risk factors had higher cT1 (834ms vs. 737ms, p=0.004) and PDFF (8.7% vs. 2.2%, p<0.001) compared to those without risk factors (**Fig 2**). Those with elevated cT1 tended to have both high BMI and abnormal metabolic measurements including insulin (p=0.005) and leptin (p<0.001).

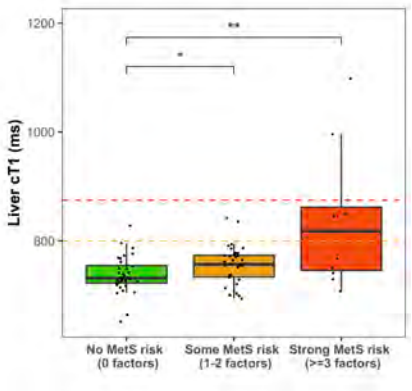

Fig. 2. *The relationship between corrected T1 (cT1) and increasing metabolic syndrome (MetS) risk groups.*

Discussion: The increasing prevalence of paediatric obesity has been strongly linked with rising global rates of NAFLD. This prospective study has demonstrated that elevated cT1 and PDFF, indicating liver dysfunction, are correlated with higher BMI and a greater risk of MetS. The significant association between increased risk of MetS and abnormal mpMRI, particularly cT1, highlights that cT1 has similar utility as reported in adult management.

Conclusions: Liver cT1 measurement has clinical utility in routine paediatric NAFLD screening programs, especially of high risk (high BMI and high MetS risk score) children, to assess NAFLD and its severity, alongside fibrosis markers for those with advanced liver disease. This would support early disease detection and stratification of young asymptomatic children at increased risk of developing NAFLD for therapeutic intervention.

References

[1]. Bachtiar, V. et al. Repeatability and reproducibility of multiparametric magnetic resonance imaging of the liver. *PLoS One.* **14,** e0214921; 10.1371/journal.pone.0214921 (2019)

[2]. Andersson, A. et al. Clinical utility of MRI biomarkers for identifying NASH patients' high risk of progression: A multi-center pooled data and meta-analysis. *Clin. Gastroenterol. Hepatol. Off. Clin. Pract. J. Am. Gastroenterol. Assoc*. **20,** 2451–2461; 10.1016/j.cgh.2021.09.041 (2021).

PT2-6

Improving the patient experience for paediatrics in Magnetic Resonance Imaging through Play Therapy

Charlotte Swain[1], Carolyn Costigan[1], Selene Rowe[1].

[1]Nottingham University Hospitals,
Queens Medical Centre,
MRI Department,
A-Floor, West Block,
Derby Road,
Nottingham, NG7 2UH.

Introduction - With Magnetic Resonance Imaging (MRI) being the gold standard for diagnosis, treatment planning and follow-up for many conditions, the number of MRI requests is only ever increasing. This is especially true for paediatrics who can be a challenging patient group, frequently with additional needs [1, 2]. Often the answer has been to scan younger children under general anaesthetic (GA), however this comes with associated risks and additional costs [1, 2]. Attending for a GA scan can be traumatic for not only the patient, but also for the parents/carers [3]. Hospitals can be frightening places with lots of new people and scary equipment and seeing your child go undergo an unfamiliar procedure, often when poorly can be very difficult for some [3]. We have tried a new method to reduce the need for a GA, and in turn, save money and improve the patient experience.

Play therapy had been used in our trust to help prepare children for their GA-MRI scan. It was suggested that with enough time, the correct preparation and support from the play specialists, it would be possible for children to have MRI scans awake. After reviewing the Paediatric MRI pathway and liaising with the children's hospital, a successful bid was made to the hospital charities to fund a full-time play specialist for 12 months, which has then continued due to initial success.

Methods - We began with a small but successful trial of 8 children, with 7 children completing their scans with diagnostic images. Only 1 had to return for a scan under GA due to noise sensitivity. After this positive outcome we began booking one Play Therapy List (6-8 patients) per week.

Initially we started with children aged between 3-12years for non-contrast scans, but have expanded this slightly for older children with additional needs and for some well-behaved younger children. We now also scan those who require contrast, including a much larger proportion of those on the waiting list. When a potentially suitable patient is identified, the parents/carers are called to explain this new service and to discuss whether their child may be able to have an awake scan.

We currently run one list a week due to scanner capacity, each appointment slot has additional time for preparation with the play specialists and bookings are also overlapped so one can be scanned whilst the next is being prepped.

Each session with a play specialist is tailored to the patient so is different every time. Everyone is individual so may need more or less support and reassurance. After building a rapport with the child and their parents/carers, a simple explanation is given - They need to lie down and stay very still, it will be very noisy and will take about 30 minutes, but they can watch a film through a mirror above their head and wear headphones. Whilst you have to provide reassurance, support and make it fun; most importantly you need to be honest. "It doesn't hurt, but it will be noisy".

From a Radiographers point of view, we use slightly adapted protocols with as few sequences as possible, scanning the most important first, and noisiest last. Motion controlled sequences are also used where possible. We do work closely with the Play Specialists so it's important to be patient, but also have a sense of humour.

In addition, we were lucky enough to have a new section of the department built with children in mind; a colourful and fun waiting room with toys, books and films, an animation comparing the MRI process to a space journey, a kitten scanner for younger children to play with and a screen with a DVD player in the scan room. All which have greatly helped the Play Specialists to work their magic.

Results - The first 14 months of Play Therapy lists have been analysed for success. Out of those who were given a play therapy appointment, 95% of patients managed to have their scan awake. The main reasons for children not being able to go through with their scan is being too scared, or anxious, having had a traumatic experience with the cannulation beforehand or being noise sensitive. The majority of children were between 4-13yrs old, some older children with additional needs and a few very well behaved 3yr olds.

Diagnostic images are the main aim of any scan. When all awake scan reports were reviewed for comments on motion artefact, 1% were undiagnostic, 4% were heavily degraded-but still diagnostic, 7% moderate and 12%. 76% had no noteworthy motion artefact showing the success of this new pathway.

Going forward we will continue to analyse the data in more depth to include more detailed feedback from children/parents/carers, reduction levels of waiting lists and any difficulties the play specialists have. Difficulties included limited scanner capacity and a lack of both Play Specialists and Radiographers leading to only one list per week. Children picking up on parents' anxieties leading to additional preparation and time being needed for some parents too. Delays due to difficult cannulations and waiting for Drs to attend to give contrast.

Discussion - Play Therapy is not a new concept within healthcare, but with funding from charities and support through the play specialist team, setting up this new service within MRI has been extremely beneficial. Focussing on not only the patient experience, but also the experience of the parent/carer has led to increased attendance rates and a more positive overall outcome for all involved.
With no relative risk when compared to a scan under GA, less traumatising for the children, and 95% of successful scans having diagnostic images, this new service is certainly advantageous. Not only for the patient/parent, but also for the trust as money is saved due to expensive equipment and specialist staff not being needed, and waiting lists being reduced faster.
Whilst the role of the Radiographer has not changed a great deal, being involved with these Play Therapy Lists has helped to develop our own practice through improved communication and interpersonal skills. Observing and assisting the Play Specialists has highlighted alternative techniques which we can adopt when scanning paediatrics at other times, not only during these specialist lists. The ability to adapt our approach to each individual patient is essential for providing the best care possible.

Conclusion - Play Therapy has been an excellent addition to the options available for paediatric patients needing an MRI scan. Not only is it safer for the child, less traumatic and occasionally enjoyable, but it is a more pleasant and less stressful time for the parents. A relatively simple service to implement, it is cheaper for the trust and has helped to reduce the paediatric waiting list considerably; allowing those who do need a scan under GA to have this sooner.

Acknowledgements: Nottingham Childrens Hospital: The Big Appeal. NUH WAVE Team. Nottingham Hospital Charity.

References

[1]Harrington, S.G. et al. (2022) 'Strategies to perform magnetic resonance imaging in infants and young children without sedation', Paediatric Radiology, 52(2), pp. 374–381. doi:10.1007/s00247-021-05062-3

[2]McGuirt, D. (2016) 'Alternatives to Sedation and General Anaesthesia in Paediatric Magnetic Resonance Imaging: A Literature Review', Radiologic technology, 88(1), 18-26. PMID: 27601689

[3]Sullivan, V., Sullivan, D.H. and Weatherspoon, D. (2021) 'Parental and Child Anxiety Peri-operatively: Relationship, Repercussions, and Recommendations', Journal of peri-anesthesia nursing : official journal of the American Society of Peri-Anesthesia Nurses, 36(3), pp. 305–309. doi:10.1016/j.jopan.2020.08.015.

PT2-7

Hemispheric dominance during comforting sound at various intensity levels: Evidence from BOLD fMRI

Farahnaz Ahmad Anwar Bashah[a,b], Ahmad Nazlim Yusoff[b*], Noor Alaudin Abdul Wahab[c], Hamzaini Abdul Hamid[d]

[a]Centre for Medical Imaging, Faculty of Health Sciences, Universiti Teknologi MARA, Bandar Baru Puncak Alam, 42300, Kuala Selangor, Malaysia
[b]Center for Diagnostic, Therapeutic and Investigative Studies, Faculty of Health Sciences, Universiti Kebangsaan Malaysia, Jalan Raja Muda Abdul Aziz, 50300, Kuala Lumpur, Malaysia
[c]Center for Rehabilitation and Special Needs Studies, Faculty of Health Science, Universiti Kebangsaan Malaysia, Jalan Raja Muda Abdul Aziz, 50300, Kuala Lumpur, Malaysia
[d]Department of Radiology, Faculty of Medicine, Hospital Canselor Tuanku Muhriz,Universiti Kebangsaan Malaysia, Bandar Tun Razak, Cheras, 56000, Kuala Lumpur, Malaysia

Introduction: Natural environmental sound such as the sound of flowing water offers a therapeutic element for balancing emotional and mental states. This is because the sound of flowing water possesses comforting and relaxing qualities to human listeners [1][2]. However, evidence reporting hemispheric dominance in the presence of comforting sound, particularly in auditory working memory (AWM) area, remains limited. A recent study utilising a noisy background confirmed changes in the lateralization of AWM during stochastic resonance (SR) mechanism leading to enhanced cognitive performance [3].

Methods: In this study, functional magnetic resonance imaging (fMRI) was used to examine the effects of comforting sound on working memory (WM) through a word reversal task. Thirty-three healthy male non-musicians (Mean age = 21 years) participated in the study. Participants were required to listen to a series of words presented auditorily and repeat them in reverse order. The auditory stimuli were presented at an intensity level of 60 dB with comforting sound embedded at 45, 50, 55 and 60dB as background noise. Six regions of interest (ROIs) related to AWM were investigated, namely the bilateral superior temporal gyrus (STG), medial frontal gyrus (MFG) and superior frontal gyrus (SFG). Data were analysed using Statistical Parametric Mapping (SPM) version 12.0 and MATLAB R2021b. Individual participant's activation was obtained via a fixed-effects analysis (FFX) at a corrected threshold at pFWE < 0.05. The number of activated volume (NAV) was extracted from the designated ROIs for each participant using the WFU-Pickatlas [4] and plotted using MS Excel to obtain the inverted "U" curve.

Results: Mean WRT score plotted across all intensity levels revealed an inverted "U" shape curve, indicating the presence of SR phenomenon as shown in Figure 1. The mean NAV for right hemisphere of STG, MFG, SFG are higher compared to left hemisphere within the same ROI. Brain activity exhibited a sinusoidal pattern, which peaks at 45dB and 55dB and trough at 50dB and 60dB depicted in Figure 2 which describes the mean NAV plotted against 45, 50, 55 and 60dB for right and left hemispheres in each ROI.

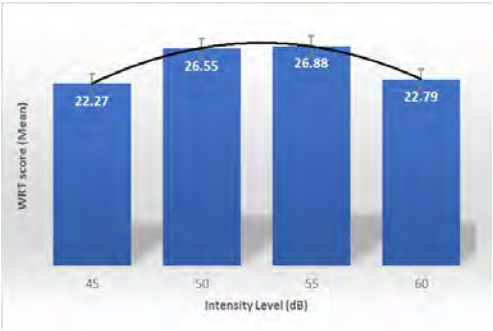

Fig. 1. WRT score during comforting sound at four intensity levels.

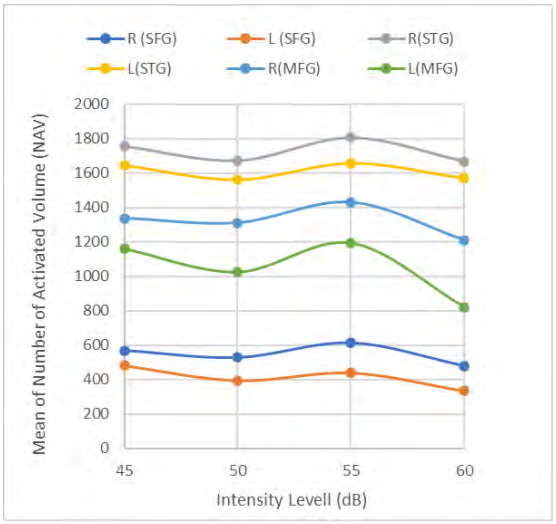

Fig. 2. Scatterplot depicting the mean NAV of bilateral ROIs in AWM area.

Discussion: In the presence of comforting sound at 55dB, AWM performance was improved in all participants indicated by the mean across all ROIs ($Mean_{ROIs}$= 1190.5) and mean WRT score (M_{score}= 26.88). Brain activation during comforting sound reached its peak at 55dB for all ROIs in both hemispheres, with higher activation observed in STG, MFG and SFG respectively. The finding also demonstrated dominance in the right hemisphere. Comforting sound was found to have the potential to enrich neural processing of STG, MFG and SFG during task execution. However, the study did not observe the SR phenomenon to the same extent as with white noise through the brain activation especially for SFG area[3]. Nonetheless, listening to comforting sounds not only exudes relaxed state but also has the capacity to improve cognitive performance.

Conclusions: Hemispheric asymmetry was observed with dominance in the right hemisphere under the presence of comforting sound during processing of series of words in reverse order resulting in a sinusoidal pattern of brain activity in non-musician young adults.

Acknowledgements: This project was funded by Universiti Kebangsaan Malaysia (UKM) under research grant GGP-2020-002. A special gratitude to Ministry of Higher Education, Malaysia and Universiti Teknologi MARA (UiTM) for the continuous support.

References

[1] Z. Tian, B. Y. Kim, and M. J. Bae, "Study on acoustic analysis of Cleveland Dam waterfall sound," *Int. J. Eng. Res. Technol.*, vol. 13, no. 6, pp. 1159–1164, 2020, doi: 10.37624/ijert/13.6.2020.1159-1164.

[2] H. Jo, C. Song, H. Ikei, S. Enomoto, H. Kobayashi, and Y. Miyazaki, "Physiological and psychological effects of forest and urban sounds using high-resolution sound sources," *Int. J. Environ. Res. Public Health*, vol. 16, no. 15, 2019, doi: 10.3390/ijerph16152649.

[3] E. A. Othman, A. N. Yusoff, M. Mohamad, H. Abdul Manan, A. I. Abd Hamid, and V. Giampietro, "Hemispheric Lateralization of Auditory Working Memory Regions During Stochastic Resonance: An fMRI Study," *J. Magn. Reson. Imaging*, vol. 51, no. 6, pp. 1821–1828, 2020, doi: 10.1002/jmri.27016.

[4] J. A. Maldjian, P. J. Laurienti, R. A. Kraft, and J. H. Burdette, "An automated method for neuroanatomic and cytoarchitectonic atlas-based interrogation of fMRI data sets," *Neuroimage*, vol. 19, no. 3, pp. 1233–1239, Jul. 2003, doi: 10.1016/S1053-8119(03)00169-1.

PT3-1

Quantitative Dixon imaging and MR spectroscopy to characterise early alterations in liver fat in a novel model of diet-induced Metabolic Associated Fatty Liver Disease.

Christopher Ball[1,4], Z.S.Low[2], J.Yaligar[1], S.Verma[1], N.B.E Sahib[2], H.S. Cheng[2], Y.S.Yip[2], J.Y.H.Lee[2], D.Lim[2], W.Wahli[2], H.Poptani[4], A.Tan[2,3], S.Velan[1].

1. Agency for Science, Technology and Research, Singapore
2. Lee Kong Chian School of Medicine, Singapore
3. Nanyang Technological University, Singapore
4. University of Liverpool, UK

Introduction: Metabolic-associated fatty liver disease (MAFLD) occurs in 25% of the population and is comprised of a spectrum of increasingly pathological states: steatosis (lipid accumulation) to steatohepatitis (inflammation and fibrosis) and finally cirrhosis (parenchymal replacement) [1]. Proton density fat fraction (PDFF) imaging provides quantitative information about liver fat and permits in-vivo longitudinal assessment of disease progression [2]. We have developed a novel murine model of LIver Disease Progression Aggravation Diet (LIDPAD), which matches all physiological alterations present in human MAFLD. The current study was performed to characterise this MAFLD model using Dixon imaging and MR spectroscopy.

Methods: 8-week-old, C57BL/6 mice were fed the high-fat LIDPAD or control diet for up to 48 weeks. Using a 9.4 T MR system and a multi-gradient eight-point Dixon imaging sequence, hepatic and abdominal fat was quantified from 4-, 8- and 16-week diet fed mice. Sequence parameters; TEs 1.85, 2.08, 2.32, 2.56, 2.80, 3.04, 3.27, 3.51ms; TR 12ms, flip angle 5°, 30 slices, 1mm thickness; 256x256 image size with 40x40mm FOV. PDFF maps calculated using Fat-Water Toolbox [3]. 3350mm^3 ROIs were placed in each liver. Water unsuppressed single voxel PRESS sequence was used to measure the lipid/water ratio in a 3mm^3 voxel using 128 averages, TE 17.8ms and TR 4500ms. In vivo MRS results were confirmed with high-resolution magic angle spinning nuclear magnetic resonance (HRMAS-NMR) with 10uL TMS reference using 30mg of the liver tissue. Samples were spun at 5KHz in a 4mm ZrO2 rotor at 277K using 16 scans, receiver gain of 16, a recycle delay of ten seconds and a spectral width of 14.027ppm. Spectral peaks were assigned according to published literature and integrated for comparison against the TMS peak. Fat fraction was calculated using the total lipid and water integral values.

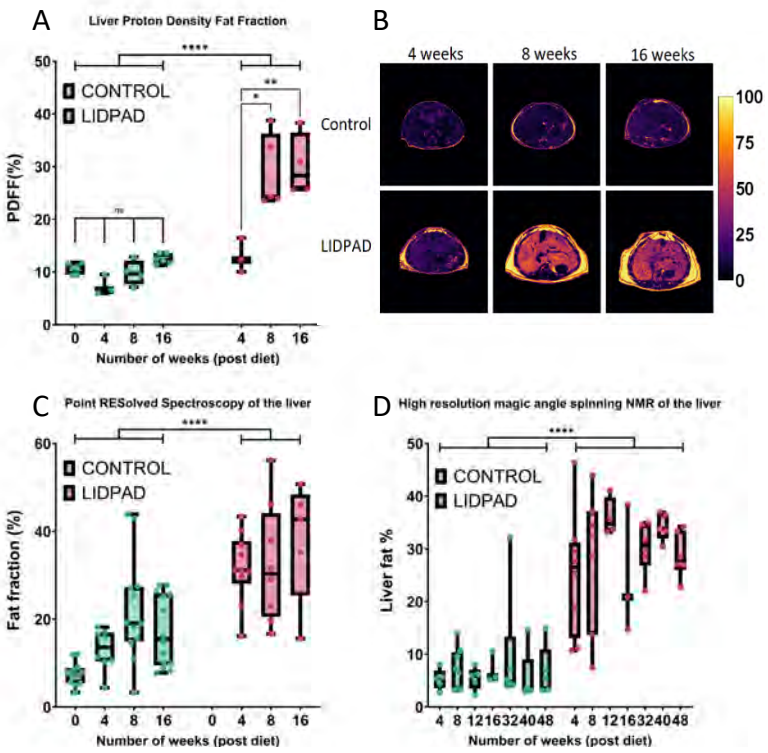

Figure 1. 1A and 1B show *in-vivo* quantification of hepatic fat through Dixon imaging. Spectroscopic techniques, *in-vivo PRESS* (1C) and *ex-vivo HRMAS-NMR* (1D) were also used for confirmation and timepoint extension.

Results: LIDPAD-fed liver PDFF ranged from 12.6% to 28.3% and was significantly increased over control PDFFs (6.6-12.3%) at all

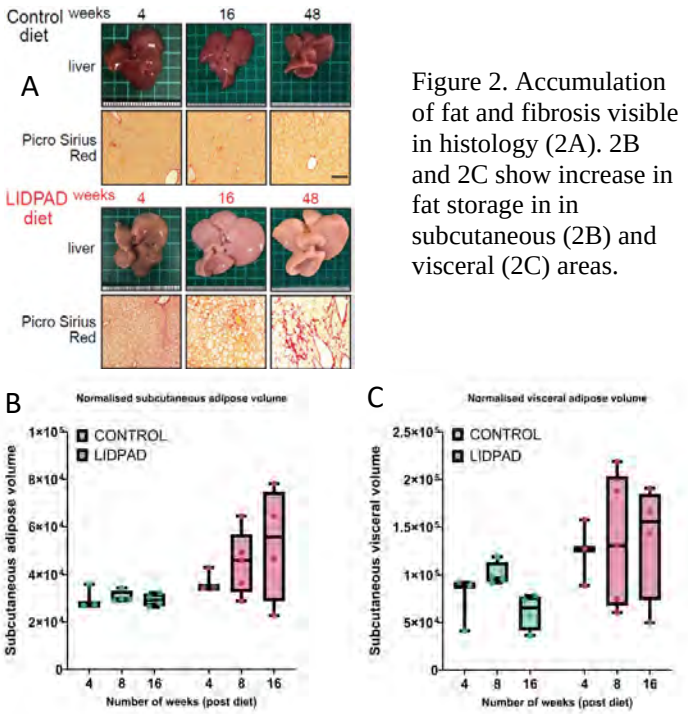

Figure 2. Accumulation of fat and fibrosis visible in histology (2A). 2B and 2C show increase in fat storage in in subcutaneous (2B) and visceral (2C) areas.

timepoints (p=<0.01 for all) (figure 1A, 1B). A near-10-fold increase in lipids between 4 and 8 weeks occurred (2.9% to 28.9%, p=0.02), but fat aggregation slowed at the last timepoints. HRMAS-NMR confirmed a swift hepatic lipid accumulation at early time points of the LIPAD diet, followed by a plateau; 12- and 40-week livers had similar lipid content (p=0.9) (Figure 1D). A reduction in the median LIDPAD lipid concentration (34.2% to 27.5%) was detected between the 40th- and 48th-week. After four weeks of LIDPAD feeding, histological alterations in the liver were consistent with steatosis and heavy fibrotic deposition by 16 weeks (figure 2A). Outside of the liver, lipid accumulation was also detected in the abdominal area, both viscerally and subcutaneously. Although not significant, the mean visceral fat volume increased 2.3-fold at 16-weeks post-diet initiation between control and LIDPAD mice. Similarly, mean subcutaneous fat volume was nearly double at 16 weeks in LIDPAD mice (figures 2B and 2C).

Discussion: Dixon imaging provides an assessment of global fat accumulation, allowing for visual representation of fat deposits throughout the liver. Imaging permits the diagnosis of steatosis in humans when the average fat percentage is above 5% [4]. LIDPAD-fed mice demonstrated steatosis, with an early and significant rise in hepatic lipids within the first four weeks, which continued to rise until the sixteenth week. LIDPAD-fed mice displayed increased abdominal fat volumes in both the visceral and subcutaneous compartments. Human MAFLD patients often present with obesity and adiposity, which is reflected in this model. Mice fed the LIDPAD diet displayed shifts in genetic expression suggestive of lipid dysregulation and demonstrated fibrotic processes, changes presented in human MAFLD disease progression, confirmed histologically [4]. *In-vivo* spectroscopy results correlated well with Dixon fat measurements, albeit from a single voxel. While Dixon imaging allows for fat fraction assessment, it is unable to distinguish between lipid types. HRMAS-NMR analysis from samples both early and late time points of the LIDPAD diet confirmed the in vivo findings and the changes in lipid metabolism.

Conclusions: The LIDPAD model accurately mirrors the morphological and metabolic changes seen during human MAFLD pathology, with MR techniques being an ideal tool for assessing disease progression.

Acknowledgements: I would like to thank Dr Mahon Maguire, Dr Mohesh Moothanchery, Dr Le Thi Thu Giang, Kavita Kaur, Tareq Alrashidi and Non Gash.

References

1. Mitra, S., De, A. & Chowdhury, A. Epidemiology of non-alcoholic and alcoholic fatty liver diseases. Transl. Gastroenterol. Hepatol. 5, (2020).
2. Caussy, C., Reeder, S. B., Sirlin, C. B. & Loomba, R. Non-invasive, quantitative assessment of liver fat by MRI-PDFF as an endpoint in NASH trials HHS Public Access. Hepatology 68, 763–772 (2018).
3. ISMRM Workshop on Fat-Water Separation: Insights, Applications & Progress in MRI. https://www.ismrm.org/workshops/FatWater12/data.htm.
4. Dyson, J. K., Anstee, Q. M. & McPherson, S. Non-alcoholic fatty liver disease: a practical approach to diagnosis and staging. Frontline Gastroenterol. 5, 211–218 (2014).

PT3-2

^{1}H MR spectroscopy to evaluate the effect of a choline kinase inhibitor and temozolomide therapy in a mouse model of glioblastoma

Tareq Alrashidi[a], Sourav Bahduri[a,b], Elisabeth Non Gash[a], Nooradean Ahmad[a], Mohesh Moothanchery[a], Christopher Ball[a], Harish Poptani[a]

[a] Centre for Pre-Clinical Imaging Depart. University of Liverpool, Crown Street, Liverpool, L69 3BX
[b] Symbiosis Centre for Medical Image Analysis, Symbiosis International (Deemed University), Lavale, Pune, 412115, India

Introduction: An overexpression of choline kinase α (ChoKα) is a hall mark of tumour progression[1]. Total choline (tCho) has been proposed as a pharmaco-dynamic marker for monitoring response to ChoKα inhibition in rodent models of glioblastoma (GBM)[2]. Previous studies from our group have reported MRS findings assessing inhibition of ChoKα in a rat model[3] and in mouse models of breast cancer[4]. Temozolomide (TMZ) used as a standard of care chemotherapy in the treatment of GBM, especially when combined with other therapeutics[5]. However, its efficacy in combination with ChoKα inhibition has not been reported. This study was therefore conducted to explore the synergistic effect of Mn58b along with TMZ on GL261 mouse model of GBM and to evaluate whether ^{1}H MRS can detect the metabolic changes.

Methods: C57BL6 mice were injected intracranially with 5x10^{5} GL261 GBM cells in the right cortex. Once the tumours were observed on T2 weighted MRI (>3 mm in diameter), animals were divided into 4 groups and treated for five consecutive days: 1) Sham saline control (n=12, intraperitoneal injection), 2) i.p injection of 4 mg/kg MN58b (n=12), 3) 50mg/kg TMZ via oral gavage (n=7), and 4) Mn58b+TMZ (n=7). Imaging was performed on days 0 (baseline), 3 (during treatment), and 6 (end of treatment). Single voxel (2x2x2 mm3) MRS spectra were acquired from the tumour region using a PRESS sequence: TR = 2000 ms, TE1 = 9.13 ms and TE2= 7.37 ms, number of averages= 200, complex points = 2048 and spectral width =4401 Hz. Metabolite amplitude ratios (tCho/NAA, Glx/Cr and mI/Cr) were calculated and using QUEST algorithm[2] in jMRUI software.

Results: Figure 1.A shows a representative T2-weighted image of a mouse bearing the GL261 tumour with the MRS voxel placement displayed as an inset. Representative in vivo MR spectra from the tumour region of mice treated with saline, Mn58b, TMZ and combination, respectively are shown in Fig. 1B. No significant change in tumour volume (Fig. 2A) between any group was observed across all time points. On day_6, a significant reduction in the percentage change in tCho/NAA ratio with respect to baseline was observed in combination treatment group compared to control tumour-bearing mice (p=0.04, Fig. 2B). A significant reduction was also observed in mI/Cr ratio (p=0.02, Fig. 2C) between

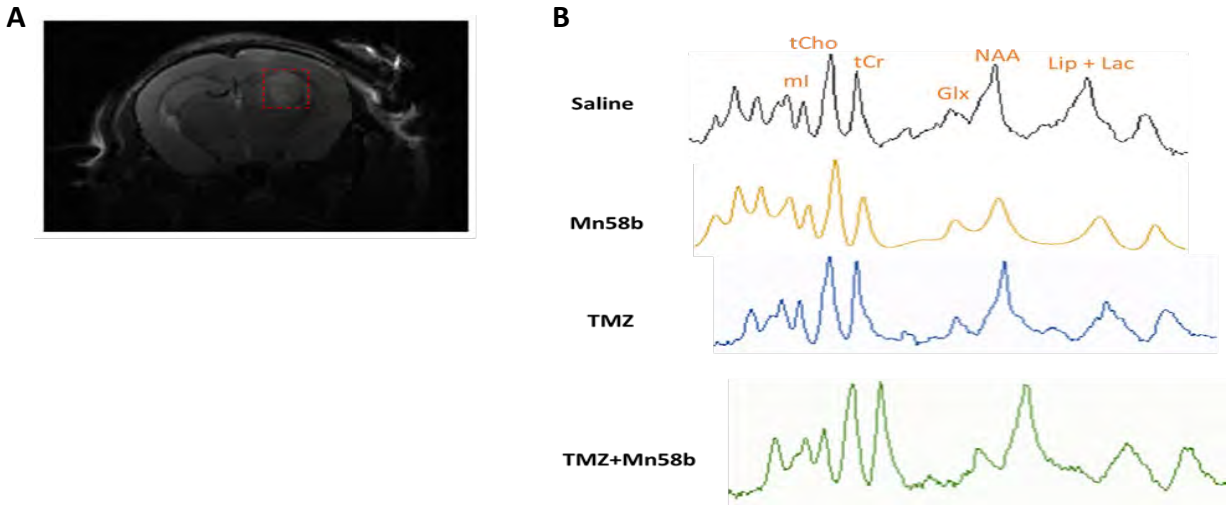

Fig. 1. A_B. ^{1}H MR spectra (voxel overlaid on T2 weighted image (A) comparing treatment response on day_6 in 4 different groups with GBM (Saline, Mn58b, TMZ and combination, respectively) showing Lip + Lac, NAA, Glx, tCr, tCho and mI peaks from the tumour region (B).

combination cohort and saline control group at the end of treatment. Combination and TMZ alone groups have also demonstrated a significant decline in GLX/Cr on days 3 and 6 (Fig. 2D). No other metabolites such as Cho/Cr or NAA/Cr demonstrated significant changes with treatment. Although trends in reduction of Cho/NAA and mI/Cr during treatment (day 3, Fig 2) were also observed, they were not significant. While MN58b or TMZ alone also demonstrated a decrease in these metabolite ratios, they did not induce significant reduction in comparison to saline controls (except for GLx/Cr in TMZ alone group). Although not significant, Fig. 2 shows that TMZ alone induced larger reductions in metabolite ratios (Cho/NAA, mI/Cr) than MN58b.

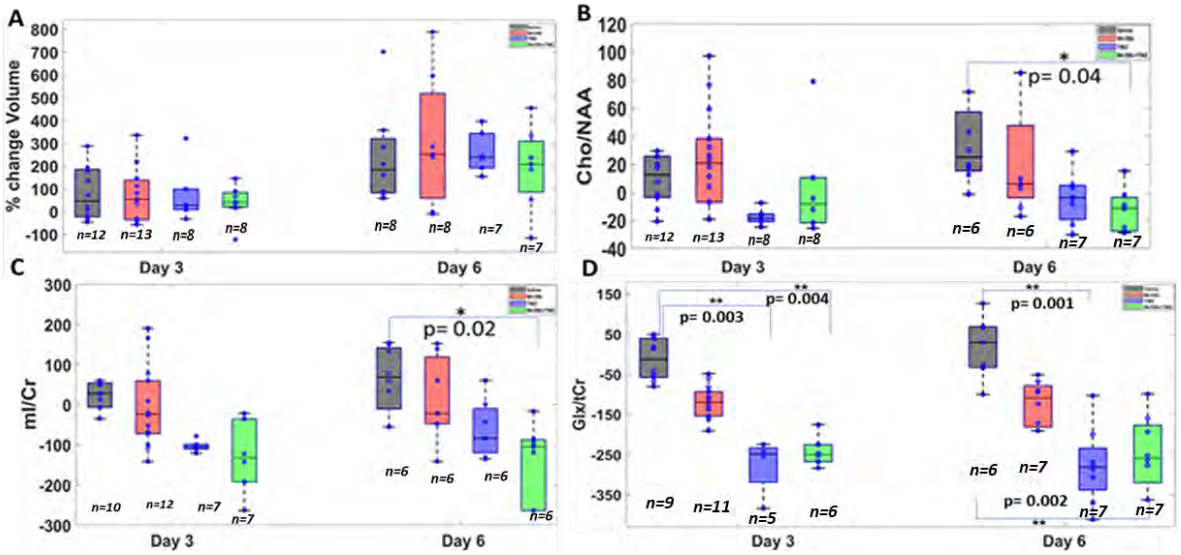

Fig. 2. A-D. Box plots comparing percentage change (with respect to baseline) in tumour volume and 3 amplitude ratios (tCho/NAA, mI/Cr and Glx/Cr) between 4 groups of mice with GL261 mouse GBM treated with different therapeutics. Asterisk indicate that the difference between groups reached a significance level of 0.05. n denotes the number of samples used for quantification.

Discussion: We observed synergistic effects of Mn58b and TMZ in the treatment of GBM in this study. tumour progression. tCho/NAA has been used extensively in clinical and preclinical studies for brain tumour grading and to assess treatment response. A significant reduction suggests ChoKα inhibition leading to an arrest in cellular proliferation[3] by Mn58b as well as the extensive DNA damage induced by TMZ triggered programmed cell death (apoptosis) in cancer cells[5]. A significant reduction in mI/Cr is similar to the earlier report in a rat model of GBM[2] suggesting a treatment response as high level of myo-inositol has been correlated with high-grade gliomas[6]. Glx/Cr ratio has also significantly declined in the combined and TMZ alone treatment groups. Such reduction has been reported in the aforementioned rat study, however a study conducted by Subramani et al. using IDH1 mutant glioma mouse models reported an increase in Glx[7] metabolism post TMZ therapy. This discrepancy in results might be due to the different GBM models used in these studies.

In conclusion, ^{1}H MRS is a powerful tool that can noninvasively monitor metabolic induced changes in gliomas in response to multiple therapeutic approaches. Concurrent targeting of ChoKα (by Mn58b) and the tumour itself (by TMZ) promise to be an alternative in the treatment of GBM.

References

[1] Glunde K, Bhujwalla ZM, Ronen SM. Nat Rev Cancer. 2011 Nov 17;11(**12**):835-48.
[2] Bhaduri S and Kelly CL, at al. NMR Biomed. 2022 Oct 21
[3] Kumar M, et al. Mol Cancer Ther. 2015 Apr;14(**4**):899-908
[4] Arlauckas SP, et al. Oncotarget. 2017 Mar 7;8(**10**):16518-16530.
[5] Park J, etal. OncoImmunology. 2018 Oct 16;8(**1**).
[6] Jaroch K, Modrakowska P, Bojko B. Metabolites. 2021, 11, 315.
[7] Subramani et al. Cancer Res; 80(22) November 15, 2020

PT3-3

Transmembrane water exchange in cellular metabolism and its role on T_1 relaxation at low field: towards an invasion/migration theranostic imaging

Hana Lahrech[a,b] and François Berger[a]

[a] Univ. of Grenoble Alpes Inserm U1205, BrainTech Lab, Bât BioB, 2280 rue de la piscine 38610 Gières, France.
[b] Univ. of Aberdeen, Biomedical Imaging Centre, Biomedical Physics Building, Foresterhill, AB25 2ZD, U.K.

Introduction: Since the early applications of the nuclear magnetic resonance (NMR) in biomedicine, the longitudinal T_1 relaxation has been reported to differentiate cancer from healthy tissues, at low magnetic fields [1]. However, low NMR sensitivity was a substantial obstacle which was overcome by the introduction of Fast-Field-Cycling NMR (FFC-NMR) technology, commercially available for physics/chemistry research around the 2000s by Stelar company. The main objectives of our recent studies were to explore the potential of FFC-NMR relaxometry at very low-field (< 2 mT) to characterize tumour heterogeneities, their phenotype and microenvironment. Our investigations were focused on glioma invasion/migration mechanisms, which are poorly diagnosed and considered a significant cause of treatment failure. New biomarkers of water molecular dynamics that connect brain tumour features to relaxation changes have been identified, in particular, T_1 relaxation at low and very low field was demonstrated sensitive to the transmembrane water exchange [2-4]. On the basis of this valuable relationship, one of our objective now, is to decipher and understand the pathophysiological processes that lead to T_1 changes and to connect them to the transmembrane water exchange in order to evaluate new theranostic strategies. In case of glioma, three main processes of invasion/migration: hypoxia, H_2O_2 redox function and water-channel aquaporins (AQP1 and AQP4) have been shown to modulate T_1 at low field as well as transmembrane water exchanges [2]. Here, our goal is focused to assess T_1 sensitivity under the effects of pharmaceutical drugs that could inhibit the pathophysiological functions of the AQP4. We focused on the bumetanide drug, a NKCC1 inhibitor [5] of sodium, potassium and chloride cellular influx. Interestingly, the bumetanide was already approved for patients and was shown to inhibit the excess expression of AQP4, that slowdowns the invasion/migration process [6]. Knowing that AQP4 interacts with several other proteins and channels, we hypothesize that treatments with bumetanide should be more beneficial than those that target water channels specifically such as AQP4 SiRNA and/or ShRNA.

Methods: FFC-NMR was used to measure T_1 at very low field and to acquire R_1-NMRD profiles ($R_1 = 1/T_1$ versus magnetic field). This technology was developed to solve the crucial problem of NMR sensitivity at low-fields. It is the only NMR technique that permits T_1 measurements at low (< 0.2 T) and very low-fields (< 20 mT), covering several decades of the frequency [10 KHz- 40 MHz], with the same relaxometer. The mathematical Power-Law model was applied to NMRD profiles by exploiting two parameters: the power-weight A_P and the power-component β, both probing tissue water dynamics. The intracellular water lifetime (τ_{IN}) that characterizes the kinetic of the transmembrane water exchange, was measured *in vitro* on glioma cells and *in vivo* on glioma models, according to methods described in references [2-4]. Two experimental glioma mouse models of invasion/migration, Glio6 and Glio96 and their corresponding cells were used. Their phenotypes were characterized by MRI (T_{2w} and DTI), HE histology, Ki-67 immunohistochemistry (IHC) and CXCR4 RT-qPCR and compared to U87, a standard glioma mouse model of high proliferation [3-4]. The effects of the bumetanide drug on NMRD profiles, on R_1 relaxation rate at very low field and on transmembrane water exchange, was evaluated on U87 glioma cells under stimuli of 5 μM H_2O_2. The bumetanide was added into the cells at a concentration of 1µM, and then the cells were put in incubation at 37 °C for approximately 18H. In preliminary experiments, a dose study has been performed using the Boyden chamber assay approach, selecting the doses that significantly slowdowns cell migration.

Results: Herein, we show that R_1 at very low fields and τ_{in} both measured *in vitro* on U87 glioma cells are sensitive to hypoxia and to H_2O_2 redox signalling. Indeed, we observed a significant decrease of R_1 and τ_{in}. Also we show that these two parameters are sensitive to invasion/migration *in vitro* and *in vivo* by comparing Glio6 and Glio96 to U87. Using IHC, we showed that AQP1 and AQP4 are up-regulated in invasion/migration, highlighting the role of these aquaporins to modulate transmembrane water-exchange that in turn modulates T_1 relaxations. All these outcomes will be clearly presented and have been already published [3-4].

The proof of the concept of the bumetanide effect was evaluated on U87 stressed with H_2O_2. R_1 relaxation rates at very low field were found higher, attempting to reach control values of U87 cells without H_2O_2 stimuli (Fig. 1), a result that suggests the slowdown of the transmembrane water exchange under the effect of the bumetanide drug that is in line with our hypothesis.

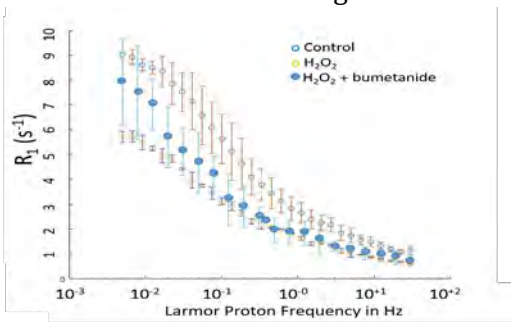

Fig. 1. Comparison of the mean R_1-dispersion between Control, H_2O_2, and H_2O_2 treated with Bumetanide (n = 6)

Discussion: The effect of the bumetanide was evaluated on U87 cells, stressed with H_2O_2 in order to mimic the characteristics of invasion/migration process and were used because they have a rapid growth than Glio6 and Glio96 (3 weeks versus 3 months). Transmembrane water exchange measurements on U87 cells and on Glio6 and Glio96 under bumetanide are works in progress and should confirm our findings. Our results stipulate the major role of FFC-imaging (FCI) and MRI at very low field to visualize the entire invasion/migration volume noninvasively and to evaluate the efficiency of innovative therapies that target transmembrane water exchange. This may impact the medical community since delineation and efficient therapies of cancer invasion/migration remain both challenging by any medical imaging modality. Our results suggest that FCI, in combination with bumetanide, may be a promising strategy in the treatment of human glioma.

Conclusions: NMR at low field appears appropriate to evaluate the effect of drugs that can target transmembrane water exchange which is connected in case of glioma to the pathophysiology of invasion/migration, namely, hypoxia, H_2O_2 signaling redox and AQP1 and AQP4 functions, opening thereby a relevant invasion/migration theranostic method, that can be extended to different cancers. Here we show the potential of the bumetanide as an anti-invasive drug and we underline the determinant role of FCI technology to evaluate its efficiency, in patients noninvasively.

Acknowledgements: We thank Y Ben-Ari for useful discussion, P.H. Fries and A. El-Gady for helping in FFC acquisitions and M. El-Atifi in cell culture.

References

[1] R. Damadian Science. **171(3976)**, 1151-3 (1971).
[2] M. R. Ruggiero, S. Baroni, S.Pezzana, G. Ferrante, S. Geninatti Crich and S. Aime *Angewandte Chemie – International.* ***57***(**25**), 7468–7472 *(*2018).
[3] M. Petit, M. Leclercq, S. Pierre, M. R. Ruggiero, M. El Atifi, J. Boutonnat, P.H. Fries, F. Berger and H. Lahrech NMR Biomed. **35(6)**, e4677 (2022).
[4] M.R. Ruggiero, H. Ait Itto, S. Baroni, S. Pierre, J. Boutonnat, L.M. Broche, S. Aime, F. Berger, S. Geninatti Crich and H. Lahrech Cancers (Basel). **29**, 14(17)- 4180 (2022).
[5] M. Zhang, Z. Cui, Cui H, Y. Cao, C. Zhong and Y. Wang BMC Neurosci. **17**, 60- (2016).
[6] M. M. Reed and B. Blazer-Yost Cell Physiol Biochem. **56(S2)**,12-30 (2022).

PT3-4

Investigating the effects of hypoxia on tumour host-vasculature relationship in a chick chorioallantoic (CAM) model of glioblastoma using MRI

Elisabeth N. Gash[1], Sarah Barnett[1], Mahon Maguire[1], Sonia Rocha[3], Judy Coulson[1], Harish Poptani[1]

1 University of Liverpool, Molecular and Clinical Cancer Medicine, Institute of Systems, Molecular & Integrative Biology, University of Liverpool, Liverpool, United Kingdom
2 University of Liverpool, Technology, Infrastructure & Environment Directorate; Faculty of Health & Life Sciences, University of Liverpool, Liverpool, United Kingdom
3 University of Liverpool, Molecular Physiology & Cell Signalling, Institute of Systems, Molecular & Integrative Biology, University of Liverpool, Liverpool, UK, Liverpool, United Kingdom

Introduction: Glioblastoma (GBM) is an aggressive brain tumour characterized by aberrant vasculogenesis and hypoxia, promoting tumour growth and treatment resistance [1].The chick chorioallantoic membrane (CAM) is a time- and cost-effective alternative to rodent models of cancer. The CAM has a well-developed vascular network, enabling tumour cells to readily engraft, and is amenable to *in vivo* imaging, making it ideal for studying vascularization (Ribatti et al., 2022). This study was performed to evaluate the effects of hypoxia on tumour/ host vasculature in the GBM-CAM model using MRI.

Methods: Tumour xenografts were generated by implanting $2x10^6$ U251 cells onto the CAM on embryonic day 7 (E7). For hypoxic tumours, cells were conditioned in a hypoxia chamber at $1\%O_2$ for 72 hours prior to implantation according to methods previously described (Al-Mutawa et al., 2018). On E13, non-tumour bearing control and xenografted CAMs were imaged *in ovo* using brightfield (BF) microscopy and MRI. For MRI, eggs were placed in a custom-built cradle with an actively decoupled 20 mm diameter surface coil placed above the site of the tumour, while an 86 mm volume coil was used as a transmitter. 3D T2-weighted (TurboRARE) images were acquired to assess the tumour volume as well as the vascular volume feeding the tumour.

Results & discussion: All tumours formed vascularized nodules with a high engraftment rate (90%). BF microscopy revealed distinct differences in CAM vasculature between GBM- and control CAMs. In GBM-CAMs, blood vessel morphology appeared to change from linear branching to a radial "spoke-like" pattern around the tumour (Fig 1A). Control CAM vessels appeared thicker, while GBM-CAMs had a greater number of small diameter vessels, suggesting angiogenesis to supply the tumour. Hypoxic GBM-CAMs demonstrated more abundant vasculature, with more blood escaping into the CAM, suggesting leaky blood vessels. These findings suggest significant vascular remodelling in the presence of GBM xenografts. MRI revealed vessels penetrating the nodules, not visible by BF microscopy. Quantification of MR images revealed a trend towards increased blood vessel volume in tumour-bearing CAMs compared to control CAMs (P= 0.1506). While tumour volume remained similar between the two groups (P= 0.7519), a trend towards greater blood vessel volume was observed in hypoxic compared with normoxic tumour-bearing CAMs (P= 0.3138).

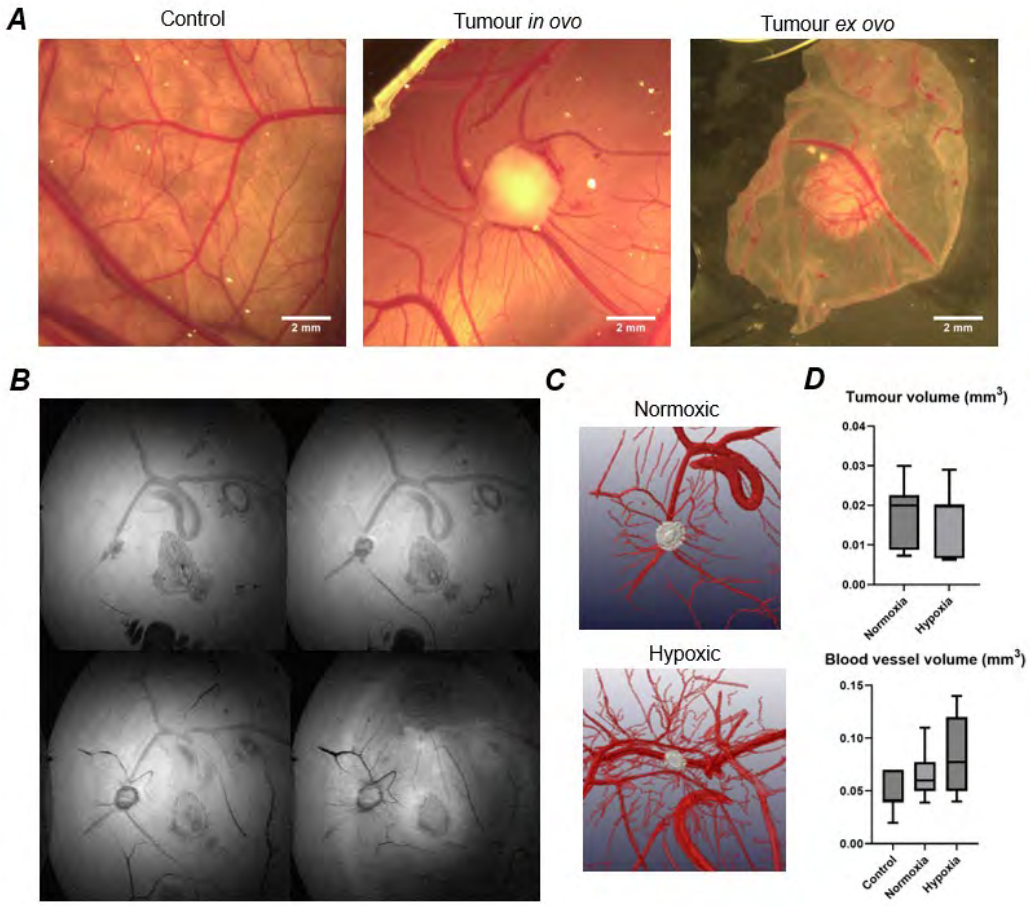

Fig. 1. GBM tumour nodules remodel CAM vasculature and hypoxic preconditioning increases vascular volume. A, Brightfield microscopy images of control non-tumour bearing CAM, GBM-CAM *in ovo* and dissected GBM-CAM tumour *ex ovo*. B, MR images of GBM-CAM. C, 3D-rendered reconstruction of tumour and its feeding and surrounding vasculature in representative Normoxic and hypoxic GBM-CAM. D, Box plots of tumour volume in normoxic (n=8) vs hypoxic (n=7) conditions; and blood vessel volume in control (n=7) vs normoxic (n8) =and hypoxic (n=8) GBM-CAMs.

Conclusions: Hypoxic preconditioning enables better recapitulation of GBM tumours in the CAM model with a trend towards increased blood vessel volume. MRI and BF microscopy enable visualization of intra- and extra-tumoural blood vessels on the CAM surface, while MRI provides additional 3D information through the layers of the CAM. In combination these provide comprehensive assessment of tumour/ host vasculature and demonstrate the potential of GBM-CAM to study anti-vascular therapies.

References

Al-Mutawa YK, Herrmann A, Corbishley C, Losty PD, Phelan M, Sée V. Effects of hypoxic preconditioning on neuroblastoma tumour oxygenation and metabolic signature in a chick embryo model. Biosci Rep. 2018 Aug 29;38(4):BSR20180185. doi: 10.1042/BSR20180185. PMID: 30026261.

[2] Ribatti D. The chick embryo chorioallantoic membrane as an experimental model to study in vivo angiogenesis in glioblastoma multiforme. Brain Res Bull. 2022 May;182:26-29. doi: 10.1016/j.brainresbull.2022.02.005. PMID: 35143927.

[1] Rosińska S, Gavard J. Tumor Vessels Fuel the Fire in Glioblastoma. Int J Mol Sci. 2021 Jun 17;22(12):6514. doi: 10.3390/ijms22126514. PMID: 34204510.

PT4-1

Lung ventilation ^{19}F-MRI using FLORET ultrashort echo time imaging.

Dominic Harrison[1,2], Mary Neal[1,2], Charlotte Holland[1,2], Matthew Clemence[3], Kieren G Hollingsworth[1,2], Pete Thelwall[1,2]

[1]*Newcastle Magnetic Resonance Centre, Newcastle University, Newcastle upon Tyne*
[2]*Translational and Clinical Research Institute, Newcastle University, Newcastle upon Tyne*
[3]*Philips Healthcare, UK*

Introduction: ^{19}F-MRI of inhaled thermally polarized perfluoropropane (PFP) is an accessible and scalable imaging technique that can quantify lung ventilation properties[1]. A challenge of inhaled PFP is its short in vivo ^{19}F T_2^* (approx. 1.8 ms). Our current ^{19}F studies[2] have used a spoiled gradient echo sequence (SPGR) with a TE of 1.7 ms, where approximately 60% of the ^{19}F signal has decayed at acquisition. The FLORET sequence is an efficient 3D trajectory based on a Fermat's spiral[3] (Figure 1). We have tested the ability of the FLORET ultrashort echo time (UTE) sequence[4] to minimize T_2^* decay, raising the SNR of lung images and thus improve scan spatial and/or temporal resolution compared to the established SPGR sequence.

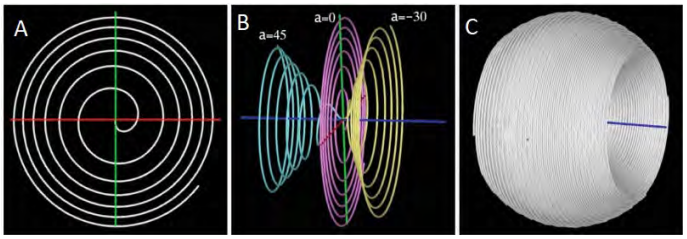

FIG.1.a. A base 2D Fermat spiral trajectory with variable radial sampling. **b.** The trajectory is shaped in 3D to follow a 3D cone. **c.** Multiple trajectories. [3]

Methods: Scans were performed on a healthy male volunteer, during breath holds after deep inhalation of 79% PFP/ 21% oxygen gas mixture. ^{19}F-MRI scans comprised a 14 s coronal 3D ^{19}F spoiled gradient echo sequence (field of view (FOV)=400x330x250 mm^3, TR= 7.5 ms, TE= 1.7 ms, flip angle= 50°, resolution= 10x10x10 mm^3, NSA= 3 and bandwidth= 500 Hz/pixel) and ^{19}F FLORET UTE sequences (FOV= 400 mm isotropic; TR= 7.5 ms, TE= 0.07 ms, flip angle= 45°). All scans were performed on a Philips Achieva 3T scanner. Table 1 shows FLORET scan parameters.

FLORET params	Isotropic resolution/ mm	NSA	Scan time/ s	FLORET hubs	FLORET alpha	FLORET interleaves
Scan 1	10	5	14	3	45°	8
Scan 2	7.5	3	16	3	45°	21

Table 1. Varied parameters of the two chosen ^{19}F-MRI FLORET UTE sequences.

Results: Figure 2 shows a single coronal slice from 3D lung scans: **A.** SPGR, **B.** FLORET UTE 10 mm isotropic, **C.** FLORET UTE 7.5 mm isotropic. Calculated SNR of each is 7.8, 14.2 and 7.2 respectively.

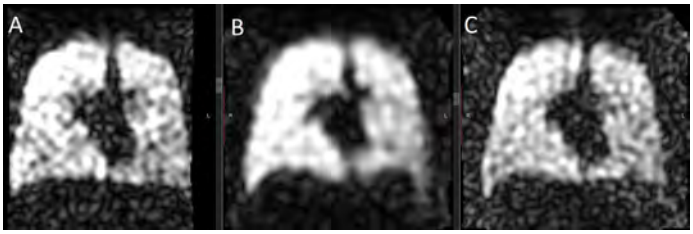

FIG.2.**a.** Central slice of SPGR sequence, resolution:10 mm isotropic. ***b/c.*** Central slice of a FLORET UTE sequence, resolution: ***b.*** 10 mm isotropic ***c.*** 7.5 mm isotropic.

Discussion: Our data show that the FLORET UTE sequence provides a 2-fold increase in SNR compared to current SPGR scans, due to reduction of T_2^* relaxation effects on signal loss. FLORET UTE at 7.5 mm isotropic resolution has comparable SNR to the 10 mm isotropic resolution SPGR sequence. The FLORET sequence allows for improved assessment of lung ventilation properties via higher spatial resolution and/or shorter duration scans.

Conclusions: This study demonstrates the reduction of T_2^* signal loss afforded by FLORET UTE sequences compared to conventional gradient echo scans, allowing for improvement of scan SNR and spatial resolution. We plan comparison of FLORET with other UTE methods such as radial, and application of ^{19}F-MRI UTE scans to measurement of lung functional and structural properties in studies of respiratory diseases.

Acknowledgements:

The authors thank the NMRC Radiographers for their assistance with this study. The FLORET sequence and reconstruction was implemented and provided by Philips Healthcare clinical science.

References

1. Couch, M.J., et al., *(19) F MRI of the Lungs Using Inert Fluorinated Gases: Challenges and New Developments.* J Magn Reson Imaging, 2019. **49**(2): p. 343-354.
2. Neal, M.A., et al., *Dynamic susceptibility contrast (19) F-MRI of inhaled perfluoropropane: a novel approach to combined pulmonary ventilation and perfusion imaging.* Magn Reson Med, 2020. **83**(2): p. 452-461.
3. Pipe, J.G., et al., *A new design and rationale for 3D orthogonally oversampled k -space trajectories.* Magnetic Resonance in Medicine, 2011. **66**(5): p. 1303-1311.
4. Willmering, M.M., et al., *Implementation of the FLORET UTE sequence for lung imaging.* Magn Reson Med, 2019. **82**(3): p. 1091-1100.

PT4-2

Age Related Changes in Peripheral Muscle Metabolism

Mehrsa Jafarpour[a], Damian J Tyler[a], Ladislav Valkovič[a,b]

[a]Oxford Centre for Clinical Magnetic Resonance Research (OCMR), University of Oxford, Oxford, UK
[b]Institute of Measurement Science, Slovak Academy of Sciences, Bratislava, SVK

Introduction: Mitochondrial function plays a vital role in regulating the metabolic activity of the cell, and so the proper function of mitochondria is important for skeletal muscle healthy ageing. However, mitochondrial impairment during ageing is poorly understood and a better understanding of skeletal muscle metabolism during ageing is required to guide research in many fields (1). Skeletal muscle phosphorus (^{31}P) magnetic resonance spectroscopy (MRS) can provide non-invasive insight into the metabolic activity, pathophysiology and oxidative state of muscle tissue. In particular, the kinetics of phosphocreatine (PCr) recovery following exercise can provide a direct quantification of the rate of mitochondrial adenosine-triphosphate (ATP) synthesis, since PCr resynthesis after exercise is purely oxidative. Previous work found larger PCr depletion in a group of elderly participants during exercise, whilst showing similar PCr recovery rate constants to those observed in a group of young volunteers (2). However, this study used global “pulse-acquire" spectroscopy without localisation to a specific muscle group, while only looking at a single bout of exercise. To build on this work, we have used a localised ^{31}P acquisition which should isolate the acquired data to that from the actively working muscle. In addition, we have utilised a second bout of exercise shortly after the first bout, to potentially reveal new biologically important differences between the young and the elderly, to better understand the changes that occur in metabolic response mechanisms with ageing.

Methods: A total of 24 healthy volunteers, 13 young (28 ± 6 years) and 11 elderly (70 ± 6 years) were enrolled to this study. All scanning was performed using a Siemens Prisma 3T MRI system with an MR compatible ergometer and a dual tuned ^{31}P/^{1}H surface coil. The workload was set to 25% of the individual participant’s maximum voluntary contraction (MVC) and an exercise protocol consisting of 1 min of rest for baseline data, followed by plantar flexion exercise at 0.5 Hz for 4 min and then 7 min of recovery was undertaken (Fig 1). Depth-resolved *in vivo* spectroscopy (DRESS) data was continuously acquired during this period with the following parameters (TR 2s, Pulse Length 600 µs, Flip angle 42^{o}, bandwidth 2000 Hz, slab thickness 20 mm, positioned obliquely over the gastrocnemius medialis muscle (3)). Following a further 7-minute rest period where no data was acquired, the dynamic ^{31}P protocol was repeated a second time (Fig 1).

Fig. 1. MRS acquisition protocol for localised DRESS sequence on the gastrocnemius muscle

Data analysis was undertaken using the OXSA toolbox (4). After applying saturation correction factors, metabolite concentrations of PCr, Pi, and PDE were calculated using the γ-ATP peak as an internal concentration reference, assuming a stable cellular ATP concentration of 8.2 mM (5). The intramyocellular pH was calculated according to the modified Henderson–Hasselback equation, based on the chemical shift of PCr and Pi signals. The time constant of PCr resynthesis (tau) was calculated by undertaking a mono-exponential fit of the PCr recovery curve. The maximal rate of oxidative phosphorylation (Qmax) was calculated according to the adenosine diphosphate (ADP)-based model of Michaelis and Menten (6). Datasets were excluded based on the pre-defined exclusion criteria: tau >250 s, PCr drop < 15%. Statistical analysis (Student’s t-test followed by Bland-Altman plots) was

undertaken in Excel, to assess the levels of agreement between the young and elderly volunteers and between the first and second bouts of exercise.

Results: The PCr measurements show no significant difference between exercise 1 and 2, and when comparing young to elderly. The Tau and Qmax also show no significant difference between exercise 1 and 2. Bland Altman graphs show a good agreement between the first and second exercise, in both age groups (Fig. 2).

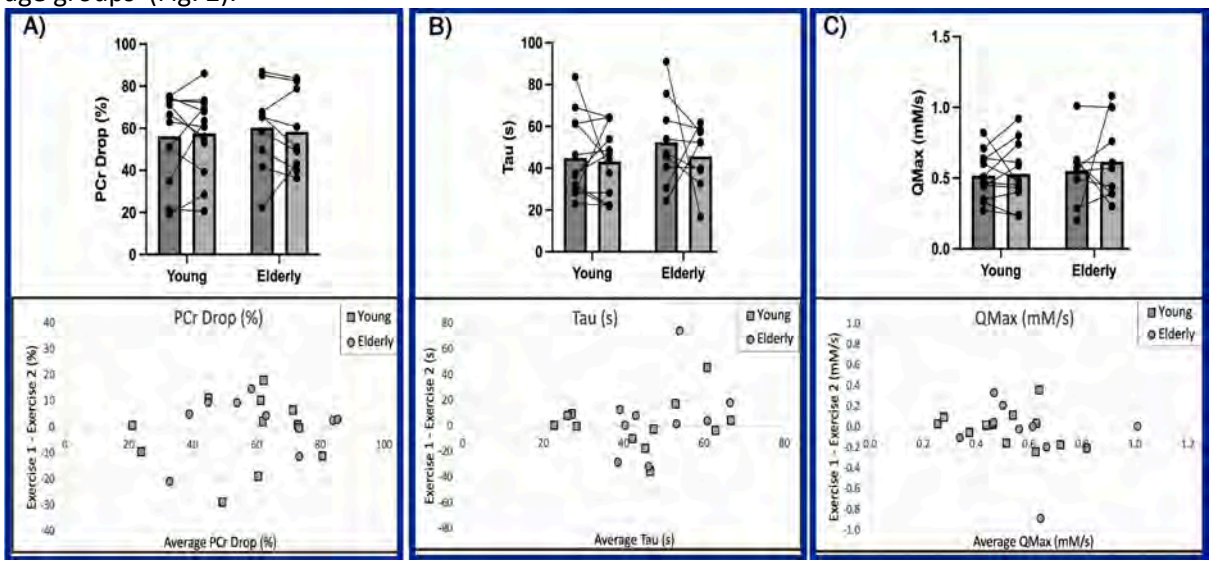

Fig. 2. Graphical representations of the ^{31}P-MRS data for both young and elderly participants, before and after exercise. Box plots and Bland Altman graphs are shown, with letters A (Tau), B (PCr drop), and C (QMax).

Discussion: In our study, we found no significance difference between exercise 1 and 2, for both age groups, when looking at PCr drop (%), Tau (s), and Qmax (mM/s). However, a previous study by Wray et al. showed a greater drop in PCr following exercise in the elderly compared to the young (2). This difference may be because we have used a localised MRS approach or because we standardised the workload to 25% of the individual subjects MVC rather than specifying a set workload (~5W in the study by Wray *et al*). Furthermore, we have looked at two consecutive bouts of exercise instead of just one, allowing us to further investigate the recovery of young and elderly participants following a metabolic stress. Through this work, we have demonstrated that overall oxidative capacity in our healthy elderly population does not appear to be blunted. This finding is supported by the work of Wray *et al* (2), where they showed that the time constant (τ) of PCr recovery did not differ between the young and old.

Conclusions: In our study, the metabolic parameters (PCr depletion, Tau and Qmax) were shown to have no significant differences between two sequential bouts of exercise in either young or elderly volunteers. Our results show that healthy elderly participants have a similar biological response to dynamic exercise when that exercise is scaled to the individuals MVC. In further work, we are exploring patient groups to assess how peripheral muscle metabolism is affected by disease.

References

[1] Scheuermann-Freestone, et al. *Circulation*. **107(24)**, 3040-6. (2003).
[2] Wray DW, et al. *J Gerontol A Biol Sci Med Sci*. **64(9)**, 968-74. (2009).
[3] Valkovič L, et al. *NMR Biomed*. **27(11)**, 1346-1352. (2014).
[4] Purvis et al. *PLoS ONE* **12(9)**, e0185356. (2017).
[5] Taylor et al., *Mol Biol Med*. **1**, 77-94 (1983).
[6] Kemp, G.J., et al. *NMR Biomed*., **6**, 302-310. (1993).
[7] Krumpolec P, et al. *Front Physiol*. **11**, 644 (2020).

PT4-3

T1ρ imaging for detecting takotsubo cardiomyopathy

Liene Balode[a], Robert Kelly[a] David Gamble[a], Dana Dawson[a], James Ross[a]

[a] University of Aberdeen, Aberdeen, UK

Introduction: In addition to conventional parametric mapping that use the spin-lattice (T1) and spin-spin (T2) relaxation mechanisms, a new native image parametric mapping method using spin-lattice relaxation in the rotating frame (T1ρ) has been recently described. T1ρ contrast can be acquired when the magnetization is prepared with the spin-lock (SL) pulse and is followed by the image acquisition sequence. T1ρ relaxation is sensitive to the low-frequency (Hz-kHz) ^{1}H motion; therefore, it can be used to investigate the exchange of protons between water and macromolecules [1]. We aimed to investigate the use of T1ρ MRI for detecting myocardial changes in acute takotsubo cardiomyopathy patients. Takotsubo cardiomyopathy is a temporary and severe left ventricular dysfunction caused by extreme emotional or physical stress [2], that confers significant mortality and morbidity.

Methods: After informed consent, takotsubo cardiomyopathy patients (n=51) and healthy volunteers (n=15) were scanned using a 3.0 T MRI scanner (Achieva dStream, Philips, Amsterdam, Netherlands). An electrocardiogram (ECG) triggered imaging sequence starts with a SL pulse (90_x-SL_y-180_y-SL_{-y}-90_{-x}) which is followed by a breath-held single-shot balanced steady-state free precession (bSSFP) image acquisition to acquire equidistant short axis images of basal, mid, and apical segments of the left ventricle. Takotsubo cardiomyopathy patients had a follow up scan after 12 weeks. The quantitative analysis of the T1ρ maps was performed using the Philips IntelliSpace Portal software. The regions of interest were selected manually by defining the endocardial and epicardial borders of the myocardium.

Results: Figure 1 shows T1ρ-weighted images with different SL times within a single breath-hold and acquired corresponding T1ρ map. The quantitative analysis of T1ρ maps showed that compared to healthy controls, in takotsubo cardiomyopathy patients, there was a significant increase in T1ρ during acute presentation, which improved at 12 weeks from baseline but remained significantly increased at both mid-cavity and apical levels of the left ventricle (Figure 2).

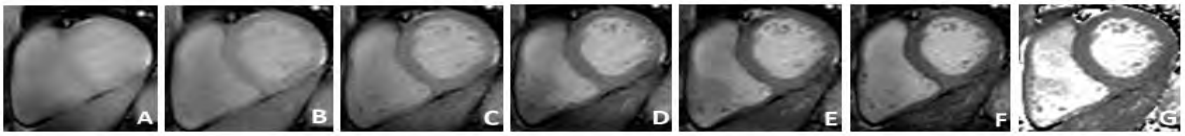

Fig. 1. Images of myocardium acquired with different SL times: (A)-(F) 0.75 ms, 8 ms, 16 ms, 24 ms, 32 ms, 40 ms and (G) the corresponding T1ρ map.

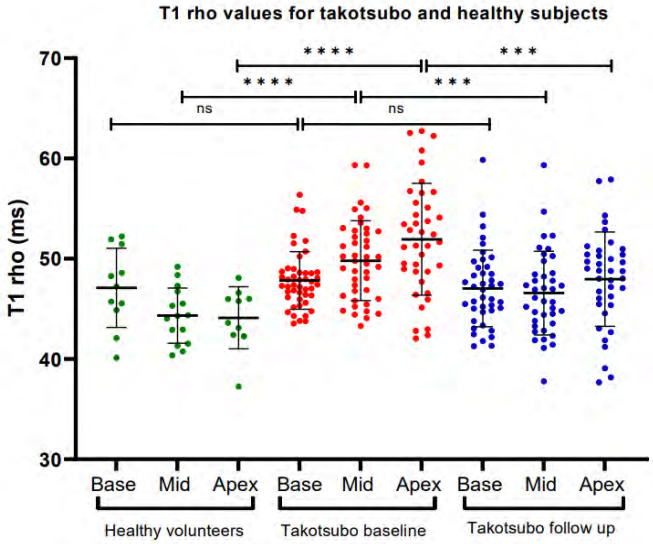

Fig. 2. Comparison of T1ρ values for the base, mid and apical segments for takotsubo patients and healthy volunteers (ns ($p>0.05$), *($p\leq0.05$), **($p\leq0.01$), ***($p\leq0.001$)).

Discussion: Takotsubo cardiomyopathy is associated with myocardial oedema in the mid and apical segments. T1ρ mapping is also able to detect this myocardial oedema, which is intense at presentation and shows part-recovery after 12 weeks follow-up in the mid and apical segments compared to healthy volunteers.
Conclusions: T1ρ MRI has a potential to detect left ventricular myocardial oedema.

References

[1] Wang P, Block J, Gore JC. Chemical exchange in knee cartilage assessed by R1ρ (1/T1ρ) dispersion at 3T. Magn Reson Imaging. 2015;33(1):38-42
[2] Singh T, Khan H, Gamble DT, Scally C, Newby DE, Dawson D. Takotsubo Syndrome: Pathophysiology, Emerging Concepts, and Clinical Implications [published correction appears in Circulation. 2022 May 17;145(20): e1053

PT4-4

Identifying Brain Calcifications in Down Syndrome Patients: An Analysis Using ZTE-Derived Pseudo-CT Imaging

Teodora Diana Catargiu[a,b], Fedal Saini[c], Mina Idris[c], André Strydom [c,d], Steve CR Williams[a], Tobias C Wood[a]

[a]Department of Neuroimaging, Institute of Psychiatry, Psychology and Neuroscience, King's College London, UK
[b]School of Biomedical Engineering & Imaging Sciences, King's College London, London, United Kingdom
[c]Department of Forensic & Neurodevelopmental Sciences, Institute of Psychiatry, Psychology and Neuroscience, King's College London, UK
[d]South London and Maudsley NHS Foundation Trust, London, United Kingdom

Introduction: Zero echo-time (ZTE) MRI is an advanced imaging method that reduces the time between radiofrequency excitation and data collection to near zero. ZTE can hence capture signals from short-T2 tissues before they decay. Its fast imaging times, silent scanning, and resistance to artifacts make it ideal for imaging cortical bone without the need for ionizing radiation. ZTE MRI can be a feasible alternative to CT scans, providing a 'one-stop-shop' solution for imaging both hard and soft tissues and reducing the need for multiple scans. This study used ZTE to obtain CT-like images from ZTE MRI in a Down's Syndrome (DS) study and identify calcifications within the choroid plexus, basal ganglia, and pineal gland which are known to occur from CT [1]

Methods: Pseudo-CT images were generated from proton density weighted ZTE images acquired from 37 patients and 12 healthy controls. The ZTE images were obtained with a matrix size of 200x200, a voxel size of 1.5x1.5x1.5 mm3, a TR of 588.04 ms and a bandwidth of ±62.5 kHz. Following Wiesinger et al., after bias field correction, normalization, and registration to MNI space, the images were segmented into three categories: bone, soft tissue, and air. This was achieved through thresholding and morphological refinements. Standard Hounsfield replacement values were assigned for air (-1000 HU) and soft tissue (+42 HU), while a continuous linear mapping technique was used for bone [2]. The analysis further involved ROI masking, voxel counting, and statistical analysis. We used masks from the Automated Talairach Atlas project for the basal ganglia (ATAG), the probabilistic atlas for the pineal gland derived by Razavi et al. [3] and the Harvard Oxford Lateral Ventricle atlas from FSL for the choroid plexus. Voxel counting was performed with a threshold of 43. A two-proportion z-test was used for the statistical analysis, comparing the proportions of calcifications in patients and controls.

Results: The obtained ZTE-derived pseudo-CT images resemble true CT images and calcifications, where present, are visible. (Fig.1). 35% of the patients present with pineal gland anomalies/calcifications ($p = 0.047$), 18% with choroid plexus calcifications ($p=0.102$), and none with calcification within the basal ganglia. Only one control presented with pineal gland calcification, and none with choroid plexus or basal ganglia calcifications.

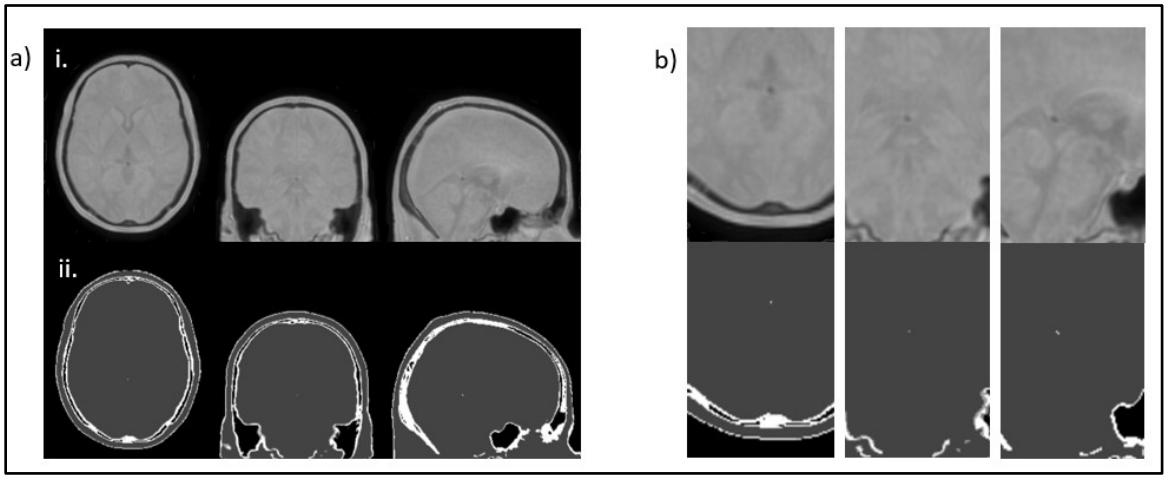

Fig. 1. a) i. ZTE image of DS patient; ii. pseudo-CT image obtained from ZTE data for the same patient before brain extraction. b) Enlarged ZTE and pseudo-CT images showing pineal gland calcification

Discussion: The results indicate a statistically significant higher incidence of pineal gland anomalies/calcifications in the patient group, while choroid plexus calcifications were not significantly different, and no calcifications were observed within the basal ganglia.

The method used for creating pseudo-CT images and identifying calcifications seems to be effective, as it allowed the detection and quantification of calcifications in the desired regions of the brain. However, a comparison with a previous CT study of Down's syndrome, reveals some discrepancies in the location and frequency of calcifications. In particular, the CT study reported a high incidence (10.7%) of bilateral calcification of basal ganglia in Down's syndrome, which was not detected in our pseudo-CT images [1]. This may be due to the different imaging modalities, insufficient sensitivity in the ZTE pCT sequence, the different age groups of the patients, or the different methods of calcification detection and quantification.

Conclusions: The method described enables MR to pseudo-CT image conversion in DS patients, in a robust, and fast manner, allowing for the detection of potential calcifications. However, differences to CT in terms of the location and frequency of calcifications, especially in the basal ganglia warrants further investigation and validation with larger and more diverse samples. Data collection in the control group is ongoing, which may increase the significance levels of our comparisons.

References

[1] Ieshima, A., et al. “A morphometric CT study of Down's syndrome showing small posterior fossa and calcification of basal ganglia” Neuroradiology (1984). doi: 10.1007/BF00342687

[2] Florian, E., et al. " Zero TE-based pseudo-CT image conversion in the head and its application in PET/MR attenuation correction and MR-guided radiation therapy planning” British Journal of Radiology (2018). doi:10.1259/bjr.20220059

[3] Razavi, F., et al. “A Probabilistic Atlas of the Pineal Gland in the Standard Space” Frontiers in Neuroinformatics (2021). doi:10.3389/fninf.2021.554229

PT4-5

Rapid In-Vivo Quantitative Conductivity Mapping in the Human Brain Using a Multi-Echo EPI Sequence

Oriana Arsenov[a], Anita Karsa[a], Oliver C. Kiersnowski[a], Patrick Fuchs[a], Simon Arridge[b], Karin Shmueli[a]

[a]Department of Medical Physics and Biomedical Engineering, University College London, London, UK;
[b]Centre for Medical Image Computing, University College London, London, UK

Introduction: Quantitative conductivity mapping (QCM) is a non-invasive MRI technique used to calculate maps of electrical tissue properties from multi-echo gradient-echo (GRE) phase images. Multiple-echo echo-planar imaging (ME-EPI) has proved useful for rapid quantitative susceptibility mapping [1]. Therefore, we investigated the applicability of ME-EPI for accelerated QCM. The phase of our ME-EPI data suffered from slice-to-slice inconsistencies: here, we tested three methods to remove these inconsistencies.

Methods: We acquired 2D ME-EPI brain images using a sequence with multi-echo capability [2] in one healthy volunteer on a 3T Siemens Prisma using eight combinations of multiband and GRAPPA acceleration: MB=1,2,3,4 and R=2,4. Each acquisition had 15 repeated volumes with 1.6 mm isotropic resolution, matrix size=150x144x120, BW= 1852 Hz/Pixel, FA=90°, 4 TEs, TE1/ΔTE=12.80/39.80 ms and TR=5440 to 21700 ms for R=2, and TE1/ΔTE=15.20/21.25 ms and TR=3218 to 12811 for R=4. A 3D ME-GRE image of the same volunteer was acquired as a reference, with 1 mm isotropic resolution, matrix size=192x256x176, BW= 280 Hz/Pixel, FA=15°, 5 TEs, TE1/ΔTE=4.92/4.92 ms, TR=30 ms, and R=3.

QCM was performed using a surface-integral-based pipeline optimized for the GRE sequence, that provides accurate conductivity (σ) for low-SNR images [3]. The phase offset at TE=0 (φ_0) was extrapolated from a non-linear fit of the complex data [4] over all echoes from the 5th volume. φ_0 wraps were removed using SEGUE [5]. Brain masks were calculated using BET [6] on the third-echo magnitude images and eroded by 2 voxels. QCM used large kernels (differentiation kernel: [11,11,11], surface integral kernel: [20,20,20]) with magnitude weighting and segmentation-based edge preservation [7,8]. The third-echo and first-echo magnitude images were used for magnitude-weighting and segmentation of gray matter (GM), white matter (WM), and cerebrospinal fluid (CSF) using FSL [9], respectively.

To try to remove slice-to-slice inconsistencies in the unwrapped EPI φ_0, we: 1) subtracted the average φ_0 in each axial slice, 2) used a phase inconsistency correction [10], and 3) subtracted a 2D in-plane linear fit in each slice.

Results and Discussion: Similar φ_0 inconsistencies have been observed for this sequence [11], which may be caused by the coil-combination method as it allows multiband acceleration. Figure 1 shows the effect of the different φ_0 inconsistency correction techniques. Correction 1) substantially reduced the inconsistencies including the bright band inferior in the brain while 2) and 3) were not effective.

The conductivity maps obtained from all the φ_0 maps were compared using the percentage of voxels in the brain mask with positive conductivities ($P_{\sigma>0}$). For the EPI data, the percentages were averaged over the 8 EPI images with different combined acceleration factors. QCM from uncorrected EPI φ_0 had unphysical $\sigma<0$ in many areas ($P_{\sigma>0}$=59.8.0%). After correction 1), EPI QCM had $P_{\sigma>0}$=75.7%, lower than GRE QCM ($P_{\sigma>0}$=89.9%). Corrections 2) and 3) did not improve QCM.

Figure 2 shows boxplots comparing corrected EPI (correction 1) and GRE σ in GM, WM, and CSF. Tissue probability maps for the segmentations were thresholded at 0.5 to exclude voxels with large partial volume contributions. The resulting segmentations were eroded by 1 voxel and negative values and outliers were removed. The mean CSF and WM σ in the corrected EPI QCM are closer to literature values [12] than those in the GRE QCM. A t-test between EPI and GRE σ was computed for the 3 regions. In all three regions, EPI and GRE σ were significantly different ($p<0.001$).

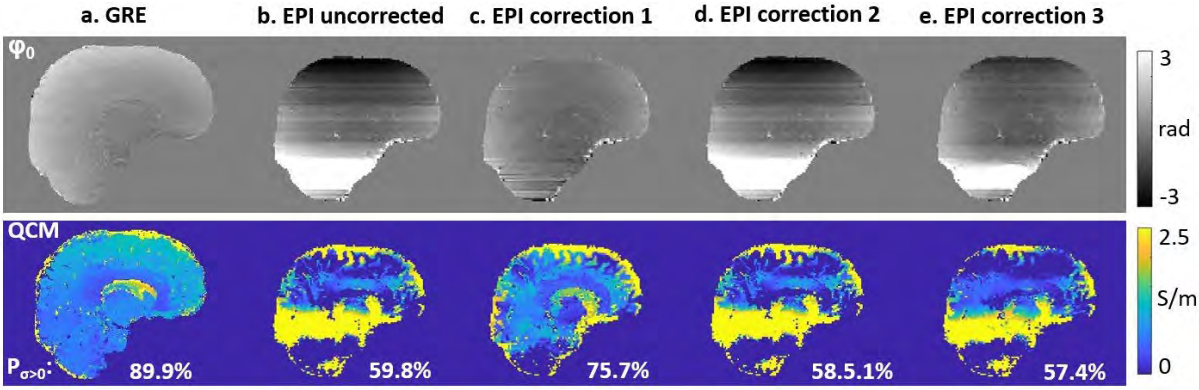

Fig. 1. Unwrapped φ_0 (top), and corresponding QCM (bottom), acquired using GRE (a) and uncorrected EPI (MB =1, R=4) (b) and showing the effect of subtracting the slice average φ_0 from each axial slice (c), applying a phase inconsistency correction (d), or subtracting a 2D linear fit from each slice (e) to correct for slice-to-slice inconsistencies.

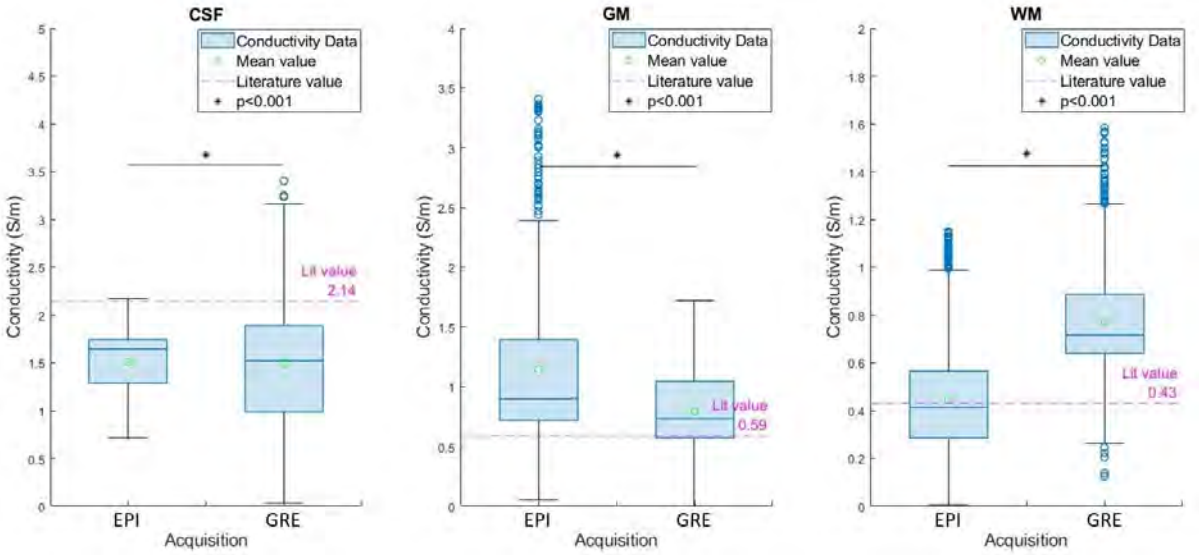

Fig. 2. Conductivity distributions in three regions, CSF, GM, and WM, in QCM from corrected EPI (correction 1, MB=1, R=4) and reference GRE acquisitions. The mean conductivity and the literature value measured ex-vivo [12], are shown in green and pink, respectively. The results of t-tests between EPI and GRE σ in the 3 regions are also displayed, * (p<0.001).

Conclusions: We have performed conductivity mapping on phase data acquired using multi-echo gradient-echo EPI with different acquisition parameters. A simple method to correct for slice-to-slice inconsistencies in EPI φ_0 maps increased the percentage of voxels with positive conductivity values ($P_{\sigma>0}$) by 15.9% on average (across all MB and R). QCM with the highest $P_{\sigma>0}$=77.4% was obtained for the ME-EPI acquisition with MB=1 and R=4, which still contained more unphysical σ values than the reference GRE result ($P_{\sigma>0}$=89.9%). In the three regions, WM, GM, and CSF, ME-EPI conductivity values were significantly different from GRE conductivity values, with the mean CSF and WM σ closer to ex-vivo values. This rapid ME-EPI QCM technique could facilitate clinical applications in the future.

References

[1] O. C. Kiersnowski et al, *ISMRM&SMRT 2022*. [2] CMRR, https://www.cmrr.umn.edu/multiband/ (2022). [3] A. Karsa et al, *ISMRM&SMRT 2021*. [4] T. Liu et al, *Magn Reason Med*, 69(2):467–476 (2013). [5] A. Karsa et al, *IEEE Transactions on Med Imag*, 38(6):1347–1357 (2018). [6] S M Smith (2002), *Hum Brain Map*, 17(3):143-155. [7] J. Lee et al, *Magn Reson in Med*, 76(2):530–539 (2016). [8] U. Katscher et al, *ISMRM 2012*. [9] *M. Jenkinson et al, NeuroImage, 62:782-90* (2012). [10] P. Spincemaille et al, *4th Int Workshop in MRI Phase Contrast & QSM*, 145 (2016)**.** [11] CMRR C2P, https://github.com/CMRR-C2P/MB/issues (2022). [12] S. Gabriel et al, *Physics in Med & Biology*, 41(11):2251 (1996).

PT4-6

A High-Performance Clustered Dictionary Search Engine using GPUs

Gabriel Zihlmann[a,b], Najat Salameh[a,b], Mathieu Sarracanie[a,b]

[a]Center for Adaptable MRI Technology (AMT Center), Institute of Medical Sciences, School of Medicine, Medical Sciences & Nutrition, University of Aberdeen, Aberdeen, United Kingdom.
[b]Department of Biomedical Engineering, University of Basel, Hegenheimermattweg 167c, 4123 Allschwil, Switzerland

Introduction: Magnetic resonance fingerprinting (MRF) [1] is a technique to simultaneously obtain multiple MR parameter maps from a single acquisition. This acquisition consists of multiple images obtained with t varying flip angles (FA) and repetition times (TR) resulting in a signal matrix $S \in \mathbb{C}^{M\times t}$ for the M voxels in the object, which contains the recorded magnetization for each FA and TR pair. In its simplest form, the reconstruction of MRF data then involves voxel-wise pattern matching of the recorded signal vectors to a dictionary $D \in \mathbb{C}^{N\times t}$ of signals covering the N MR-parameter combinations of interest, precomputed via Bloch equations. The result of the pattern matching step is the dictionary entry that maximizes the magnitude of the complex inner product with the voxel signal, and its parameter values are then assigned to that voxel.

MRF is highly flexible and allows to encode a multitude of parameters beyond relaxation times, such as static off-resonance δB_0, relative transmit-field strength B_1^+, among others [2]. However, the number of entries in the dictionary N grows exponentially with the number of parameters, which can lead to pattern matching becoming a bottleneck of MRF reconstruction.

Previous proposals to accelerating the dictionary search included compression in the time dimension by singular value decomposition (SVD) [3] or grouping dictionary entries by similarity, performing SVD-compression group-wise [4] and then only searching within the most promising groups. While these approaches showed promising results, efficient implementations harvesting the full potential of current graphics processing units (GPUs) are rare. In this work, we extended Faiss [5], a highly optimized library for large scale similarity search to be compatible with complex vectors and applied its grouped search to MRF-based OPTIMUM [2] for low-field multiparametric MRI.

Methods: Complex-vector support was added to the Flat and IVFFlat index types of Faiss. The Flat index corresponds to an exhaustive brute-force dictionary search based on matrix multiplication, whereas the IVFFlat index performs k-means-based clustering on the dictionary atoms to form groups of similar entries of which only a subset is considered during a search. The IVFFlat-index search strategy is thus like the one described by Cauley *et al.*[4], but without employing SVD within groups. Clustering must be performed once on the dictionary before the clustered search may be used.

The grouped search has two parameters: the number of groups k to form during clustering, and the number of most similar groups p to probe during search. We evaluated our search engine by performing a survey of the parameters k and p. The value for k was chosen proportional to $\sqrt{N}$, while the values of p were progressively incremented from $p = 1$ leading to slower but more accurate searches. Incrementing p was stopped when brute-force search duration was approached.

We identified optimal operating points based on a metric F computed as the fraction of voxels for which the approximate search returned a different dictionary entry than the brute-force search, constrained to those voxels for which the brute-force search exceeded an inner product magnitude threshold. This thresholding served to ignore voxels that only contain noise. An operating point is considered optimal if there exists no faster one reaching an equal or lower value for F.

Our evaluation dataset was acquired with a 3D bSSFP-based optimized MRF sequence (OPTIMUM) at 100 mT in a healthy volunteer, after informed consent was obtained. The dataset size was of 90×81×15 (109350 voxels) with $t = 18$ per voxel for a 8.5 min total acquisition time.

Two dictionaries with parameters T_1, T_2, δB_0 and B_1^+-fraction with different resolutions were used having 4.4 and 35 million entries, respectively. All results were obtained on a computer with an Intel i9-10920X 12-core CPU, 128 GiB of RAM and an Nvidia RTX 3090 GPU.

Results: Brute force dictionary search required 15 s, and 123 s for the two dictionaries. Thresholding

of the brute force results leads to roughly 20000 voxels remaining for calculating the F metric. The optimal operating points for the clustered search are summarized in Fig. 1. The larger dictionary affords significantly higher acceleration for all evaluated tolerance values with peak acceleration factors roughly 3 to 4 times higher for the larger dictionary.

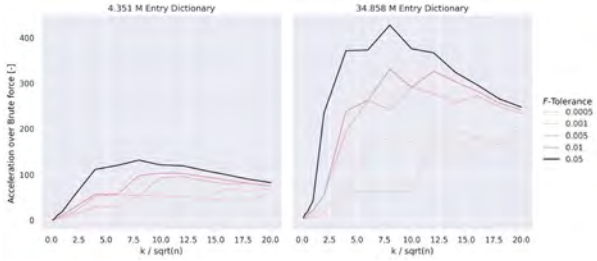

Fig. 3 Fastest configurations meeting the specified error tolerance as a function of the number of clusters k given in units of $\sqrt{N}$. Colors indicate the different tolerance of F achieved by the plotted configuration.

The T_1 and T_2 parameter maps reconstructed with the brute force search in the larger dictionary are displayed in Fig. 2, together with the errors introduced from the accelerated search. No different voxels are apparent in the shown slice for an acceleration factor of 183, while there are 5 isolated voxels with single-step errors at 292× acceleration, and 78 at 429× (not all are visible in the figure as some of the errors differences were exclusively in the omitted δB_0 and B_1^+ parameters).

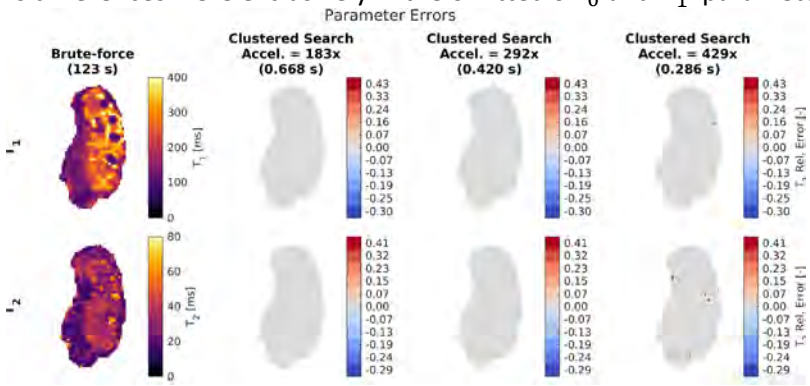

Fig. 4 Central axial slice from the in-vivo hand data reconstructed with different search parameter configurations. The increasing acceleration factors correspond to error tolerances of 0.0005, 0.005 and 0.05. The color scales of the errors are discretized in dictionary steps and show 5 steps in both directions. The error values for T_2 that exceed the color scale in the fourth column are 2.0, 0.5 and -0.4.

Discussion: Our proposed search engine allows significant acceleration of dictionary search with greater acceleration potential for larger dictionaries. Up to two orders of magnitude acceleration was achieved with virtually identical parameter maps. Further accelerations are possible at a cost of larger parameter errors. Our approach only addresses search speed and does not reduce memory requirements, however the compatibility with global SVD-compression is maintained. Further, a one-time clustering step is required prior to search. The matching engine was evaluated on comparably short MR fingerprints as produced by our balanced MRF implementation, and potential benefits for longer fingerprints and other sequence designs will be subject to future research.

Conclusions: We demonstrated a software implementation of an approximate MRF dictionary search engine that can effectively harness the computational power offered by modern GPUs. Our engine translates the benefits of group matching [4] into the age of GPU-computing.

Acknowledgements: We are grateful to the Swiss National Science Foundation for funding this work (Grant No. 186861 and 198905).

References

[1] Ma, D. *et al. Nature* **495**, 187–192 (2013).
[2] Sarracanie, M. *Invest. Radiol.* (2021).
[3] McGivney, D. F. *et al*. *IEEE Trans. Med. Imaging* **33**, 2311–2322 (2014).
[4] Cauley, S. F. *et al. Magn. Reson. Med.* **74**, 523–528 (2015)
[5] Johnson, J., Douze, M. & Jégou, H. *IEEE Trans. Big Data* **7**, 535–547 (2021)

POSTER ABSTRACTS

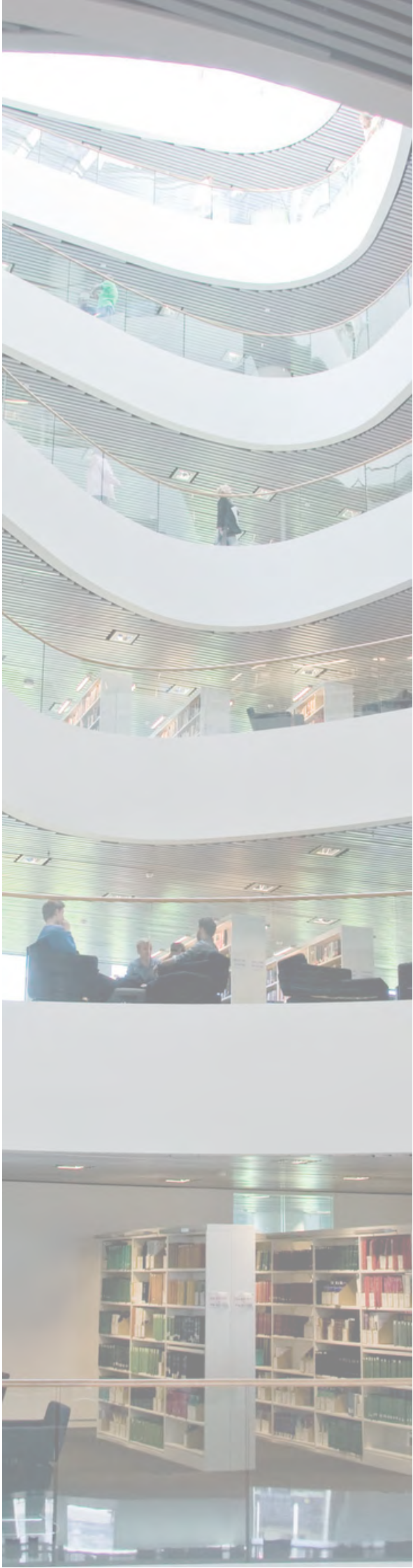

P-01

Fast Field Cycling Nuclear Magnetic Resonance: A Novel Tool for the Detection and Characterisation of Breast Cancer

Katie Hanna[a], Ehab Husain[b], Yazan Masannat[b], Rasha Abu-Eid[a], Valerie Speirs[a] and Lionel Broche[a]

[a]University of Aberdeen, Aberdeen, United Kingdom
[b]Aberdeen Royal Infirmary, Aberdeen, United Kingdom

Introduction: Fast field-cycling nuclear magnetic resonance (FFC-NMR) relaxometry is a low-field technique that can provide unique insights into molecular dynamics of biological samples, with potential translation to *in vivo* applications [1]. FFC relaxometers can rapidly switch between different strengths of an applied magnetic field to facilitate the measurement of the longitudinal relaxation time, T_1, or rate, R_1 ($1/T_1$), as a function of magnetic field strength, which is plotted as an NMR dispersion (NMRD) profile. This profile is sensitive to changes in tissue architecture, which is one of the key events that lead to cancer development and metastatic progression. Therefore, the physical information contained within the NMRDprofile may prove to be a rich source of diagnostic and prognostic information. The aim of this study is to describe the physical features of R_1 NMRD profiles from human breast tissue samples (cancerous and normal) and use mathematical models to investigate how numerical parameters, derived from these profiles, could potentially serve as biomarkers for breast cancer detection and relapse risk stratification.

Methods: A total of 148 fixed tissue samples were acquired, with ethical approval, from the tumour, peritumoral zone and distant normal regions (non-adipose and adipose) from twenty female breast cancer patients at the Aberdeen Royal Infirmary, Scotland. The pathology reported included Nottingham Prognostic Index (NPI) scores for each patient. The NPI is an internationally validated clinicopathological tool that is used for risk stratification in breast cancer patients and based on the score, patients can be grouped into one of five prognostic categories: excellent, good, moderate I, moderate II and poor. The patients in our study belonged to the latter three categories. NMRD profiles were acquired from each tissue sample using the benchtop relaxometer (SMARtracer; Stelar S.r.l., Mede, Italy). Each sample was scanned with 30 different evolution fields in the 0.001-8 MHz proton Larmor frequency range. The analysis of R_1-dispersion profiles was achieved using the software, Fitlike2 [2]. R_1-dispersion profiles were analysed by curve fitting, using the 2-segment power model (Fig. 1) and the following model parameters were exported: slope at low (α_{low}) and high (α_{high}) fields, the transition frequency between the segments (ν) and the vertical off-set of the whole dispersion profile (A). All statistical analysis was performed using GraphPad Prism v9.0 and model parameters were evaluated between different regions of breast tissue and different NPI categories using a One-way ANOVA/Kruskal-Wallis test (significance $p<0.05$, 95% confidence interval).

Results: Clear and distinct dispersion profiles were observed when sampling each of the individual regions of breast tissue (Fig. 2). Tumour tissue could be significantly distinguished from that of the peritumoral zone by A ($p<0.05$) and ν ($p<0.0001$); tumour tissue could be significantly distinguished from the distant normal tissue by A ($p<0.0001$) and ν ($p<0.0001$) and peritumoral tissue could be significantly distinguished from the distant normal tissue by α_{high} ($p<0.05$) and ν ($p<0.001$). We were also able to quantify differences between the dispersion profiles of patients within different prognostic categories when the distant normal adipose tissue was sampled. It appeared that α_{low} was significantly smaller in Moderate I compared to poor patients ($p<0.05$). Furthermore, a reduction in both α_{low} and A appeared to correspond to a worse prognosis, although this was only significant for the latter (Pearson $r = -0.3669$, $n= 36$, $p= 0.0277$).

Discussion: Based on an initial qualitative analysis of tissue dispersion profiles, it was demonstrated that field-cycling relaxometry could distinguish normal and cancerous breast tissue at low fields, which has previously been demonstrated [3-6]. These NMRD profiles represent the average water dynamics in the both the intracellular and extracellular microenvironments. At the lowest magnetic fields, $< 10^5$

Hz, tumours displayed shorter relaxation times compared to patient-matched normal breast tissue. However, for magnetic fields > 10^5 Hz, tumour relaxation times became longer than that of the normal tissue. Based on quantitative analysis, our study demonstrated the utility of a variety of numerical parameters, derived from NMRD profiles, to assist with breast tumour detection, demarcating surgical margins and informing on patient prognosis. NMRD profiles from the normal adipose tissue were significantly different depending on the patients' NPI score. This finding suggests that the earliest biophysical changes related to disease progression may occur in the periphery rather than the tumour itself.

Conclusions: This study is the first step to systematically establish quantification of differences in the NMRD profiles obtained from breast cancer tissue samples. Overall, we have shown that NMRD profiles may house novel quantitative diagnostic and prognostic biomarkers of breast cancer. Whilst our study has employed the benchtop relaxometer to study *ex vivo* tissue samples, our findings may have translational potential when combined with Field-cycling imaging that has been developed at the University of Aberdeen. The first *in vivo* T_1 measurements from breast cancer patients will be presented by another member of our team (Dr Vasiliki Mallikourti).

References

[1] Broche LM, Ross PJ, Davies GR, et al. A whole-body Fast Field-Cycling scanner for clinical molecular imaging studies. Sci. Rep. 2019;9(1):10402.

[2] Fitlike2 code freely available from GitHub: https://github.com/ManuIdentiFY/FitLike2

[3] Wang Y, Cooperman H, Rao V, et al. A nuclear magnetic relaxation dispersion profile of normal breast and tumor tissues. Magn. Reson. Imaging. 1984;2(3):235.

[4] Broche LM, Zampetoulas V, Ross PJ, et al. Detection of tissue remodelling by fast field-cycling methods. Magn. Reson. Mater. Physics. Biol. Med. 2015;28(S1):s43-s44.

[5] Ruggiero MR, Baroni S, Pezzana S, et al. Evidence for the Role of Intracellular Water Lifetime as a Tumour Biomarker Obtained by In Vivo Field-Cycling Relaxometry. Angew. Chemie – Int. Ed. 2018;57(25):7468-7472.

[6] Bitonto V, Ruggiero M, Pittaro A, et al. Low-field nmr relaxometry for intraoperative tumour margin assessment in breast-conserving surgery. Cancers (Basel). 2021;13(16):4141.

Figure 1: 2-segment power model equation

$$R_1(B_0) = \begin{cases} A\left(\frac{\gamma}{2\pi}B_0\right)^{\alpha_{low}}, & \frac{\gamma}{2\pi}B_0 < \nu_{high} \\ A\left(\nu_{high}\right)^{\alpha_{low}-\alpha_{high}}\left(\frac{\gamma}{2\pi}B_0\right)^{\alpha_{high}}, & \nu_{high} \leq \frac{\gamma}{2\pi}B_0 \end{cases}$$

Figure 2: Average R_1 dispersion curves (log/log scale), with standard deviation error bars, from breast tissue, obtained from the region of the tumour (n= 33), peritumoral zone (n= 38) and normal regions (both non-adipose (n= 25) and adipose (n= 36)).

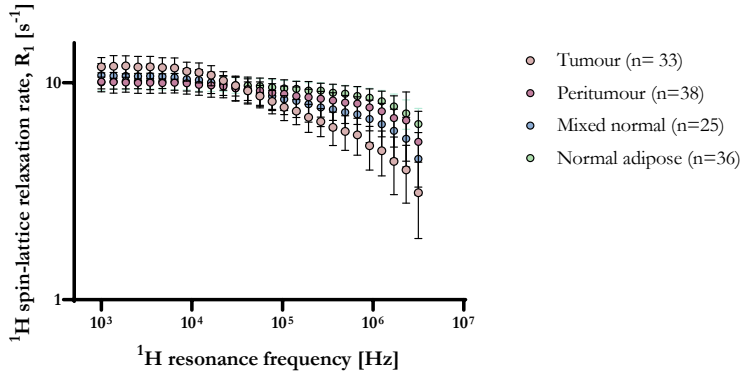

P-02

Fast Field-Cycling imaging identifies prostate cancer at magnetic field strength below 200 mT: a study on ex vivo prostate cancer

Vasiliki Mallikourti[a], Amnah Alamri[a] , Jenna Gregory[b], Sinclair Dundas[c], Lionel M. Broche[a]

[a]University of Aberdeen, Aberdeen, United Kingdom.
[b]Institute of Medical Sciences, University of Aberdeen, Aberdeen, United Kingdom.
[c]Pathology Unit, Aberdeen Royal Infirmary, Aberdeen, United Kingdom.

Introduction: Prostate cancer (PCa) is the second most common cancer in men and accounts for 7.1% of all cancer cases globally [1]. In the United Kingdom, prostate cancer is projected to become the most commonly diagnosed of all cancers, and it is predicted that could be around 85,100 new cases of prostate cancer every year by 2038-2040 [2]. Survival largely depends on detecting early-stage tumours, which often have an indolent course and may require minimal treatment. However, prostate screening by digital rectal examination (DRE) and prostate-specific antigen (PSA) measurement may lead to overdiagnosis and results in over-treatment. It is estimated from two largest prostate screening trials that between 17% and 50% of prostate cancers are overdiagnosed [3]. The challenge is differentiating between cancers that may never have become evident without screening from clinically significant tumours requiring treatment. Improved imaging technology could lead to better earlier detection of clinically significant tumours, improve staging and better inform appropriate treatment and follow-up. The aim of this study is to explore potential biomarkers in prostate cancer using the novel Field Cycling Imaging (FCI).

Methods: This prospective study was approved by the Grampian biorepository scientific committee (tissue request- TR000283) with the informed consent of all patients. From April 2022 to February 2023, we scanned 17 *ex vivo* prostates surgically removed as a standard of care for prostate cancer. The excised prostates were scanned fresh using a vertical solenoid coil for R.F. transmission and signal detection. For each sample, 20 single-slice images were acquired using a field cycling saturation sequence at four evolution fields (200, 20, 2 and 0.2 mT) and five evolution times. The slice thickness was set to 10mm and the in-plane resolution to 1.55 mm, depending on the FOV, with a matrix size of 90 x 90. The total duration of the FCI examination was 45 min. Histology analysis will be used for validation. Data analysis was done in MATLAB using in-house software [4]. The images were filtered by using the BM3D image denoising method [5]. R_1 ($1/T_1$) quantification was obtained using the exponential model derived from the Bloch equations. The fitting of R_1 NMRD profiles and the histology validation work is still in progress at the time of writing this abstract.

Results:

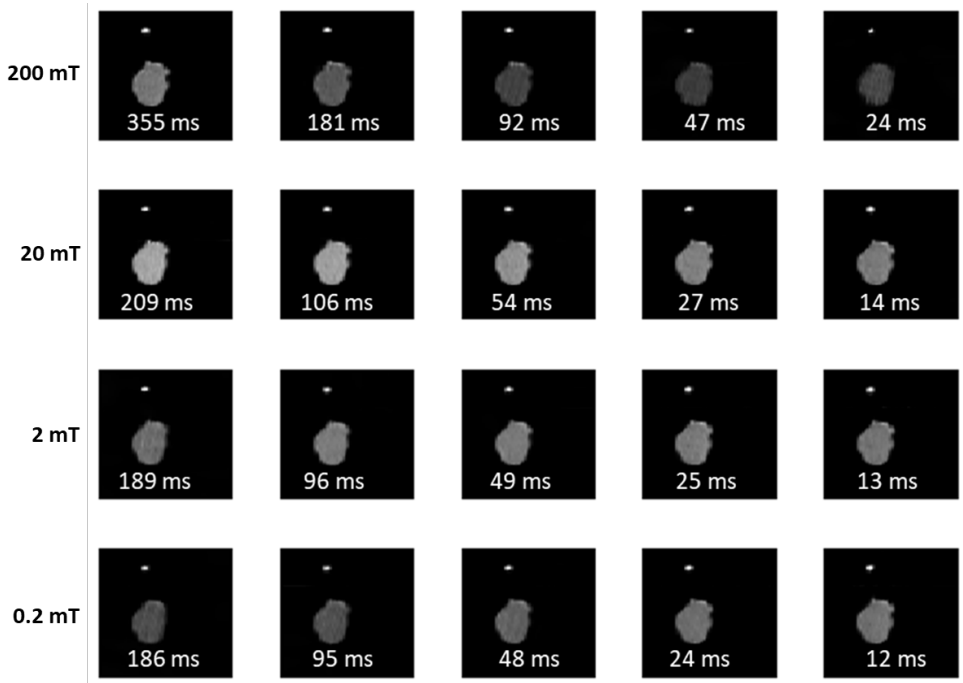

Fig. 1. **Typical FCI data** from excised prostate gland from a patient presenting with prostate cancer. The evolution times are reported in ms along the columns, and the evolution fields in mT along the rows.

Discussion: This is the first-ever measurement of R_1 dispersion in patients with prostate cancer. The preliminary results showed that FCI can have a possibility to differentiate between prostate tumours and healthy tissue without the use of contrast agent at low field strengths. However, these results will be validated by comparing the contrast in R_1 maps with the histological diagnostic sections. Correlating FCI data of whole explanted prostate glands with anatomical and histopathological features observed on routinely prepared histology sections will allow us to define FCI-generated characteristics of prostate cancers and map these with tumour localisation, tumour volume, Gleason grade and pathological stage.

Conclusions: This work showed a potential new biomarker of prostate cancer based on R_1 dispersion maps -extended to low magnetic fields -below 200 mT-. Further investigation is ongoing to contribute to a deeper understanding of prostate cancer characterisation using ultra-low field technique.

Acknowledgements: This study has received funding from NHS Grampian Endowments.

References

[1] Sung, H. et al. Global Cancer Statistics 2020: GLOBOCAN Estimates of Incidence and Mortality Worldwide for 36 Cancers in 185 Countries. C.A. Cancer J. Clin. 71, 209–249 (2021).

[2] Prostate cancer statistics. Cancer Research U.K. https://www.cancerresearchuk.org/health-professional/cancer-statistics/statistics-by-cancer-type/prostate-cancer (2015).

[3] Va, M. Screening for prostate cancer: U.S. Preventive Services Task Force recommendation statement. Annals of internal medicine 157, (2012).

[4] Broche, L. M., Ross, P. J., Davies, G. R. & Lurie, D. J. Simple algorithm for the correction of MRI image artefacts due to random phase fluctuations. Magnetic Resonance Imaging 44, 55–59 (2017).

[5] Image Denoising by Sparse 3-D Transform-Domain Collaborative Filtering. https://ieeexplore.ieee.org/document/4271520/.

P-03

Comparison of pre-processing strategies to inform data-driven classification of small vessel disease patients using field-cycling MRI

Graeme Stewart[1], Vasiliki Mallikourti[2], James Ross[2], Lionel M. Broche[2], Gordon D. Waiter[2], Mary-Joan MacLeod[2], Nir Oren[1, ǂ], Nicholas Senn[2, ǂ]

ǂ Indicates joint last author, [1] School of Natural and Computing Sciences, University of Aberdeen, UK
[2] School of Medicine, Medical Sciences and Nutrition, University of Aberdeen, UK

Introduction: Small vessel disease (SVD) results in white matter (WM) changes, affecting cognitive ability, and in severe cases, can lead to forms of dementia and stroke. New non-invasive imaging approaches have the potential to facilitate routine monitoring of SVD progression. Field-cycling imaging (FCI) is an emerging whole-body low-field MRI technology being developed at the University of Aberdeen [1]. FCI seeks to uncover more information regarding WM changes by acquiring multidimensional data sets at varied magnetic field strengths. By applying data-driven AI analysis approaches, we seek to learn patterns in the multi-field FCI data on what features constitute presence of SVD. The aim of this preliminary work was to compare pre-processing strategies to inform AI-based classification of SVD.

Methods: Data sets were included from the first 20 participants recruited into an ongoing study with clinically confirmed moderate or severe SVD (N=10) and age-matched healthy volunteers (N=10). Participants underwent 3T MRI (Philips 3T dStream) and FCI scans. For each participant, 20 FCI images were acquired for a single slice across 4 magnetic field strengths of 0.2, 2, 20 and 200 mT and 5 logarithmically spaced evolution times, resolution of 3.1 x 3.1 x 10 mm^3. The magnitude of image contrast between regions of WM and SVD was compared across the multi-field FCI images, using co-registered WM and WM hyperintensity (WMH) regions of interest generated from 3T MRI data [2]. A selection of 4 pre-processing pipelines were applied, seeking the most effective to run AI-based classification [3]. Each pipeline was evaluated by training accuracy. Saliency maps were used to provide insight into which aspects of FCI images the AI was using to inform classification.

Results: There was a significant difference between image contrast values obtained from the 20 FCI images (Friedman Test, $P < 0.001$), (Fig.1). Images obtained at 0.2 mT, 75.3 ms and 20 mT, 158.2 ms yielded greatest image contrast between WM and SVD regions (Fig.2). Training accuracy was not increased between use of original images (67%) and denoised images (67%). Use of skull-stripping yielded lower training accuracy for both original (56%) and denoised images (50%). Visual assessment of saliency maps appears to show more highlighted regions within brain tissue for use of denoised data (Fig.2).

Conclusions: This study demonstrates the potential of data-driven analysis to be used to interrogate field-cycling MRI brain imaging data. Future studies will use larger data sets to investigate the performance of different AI-based classification models using FCI data.

Acknowledgements: We would like to thank the participants who took part in this study. The study is funded by Chief Scientist Office research grant TCS/19/44.

References

1. L.M. Broche, et al. Sci Rep 9, (2019) **2.** J.M.J. Waymont, et al. J Int Med Res. 48(2) (2020) **3.** H. Zunair, et al. MICCAI 2020 International Workshop on PRedictive Intelligence In MEdicine (PRIME) (2020)

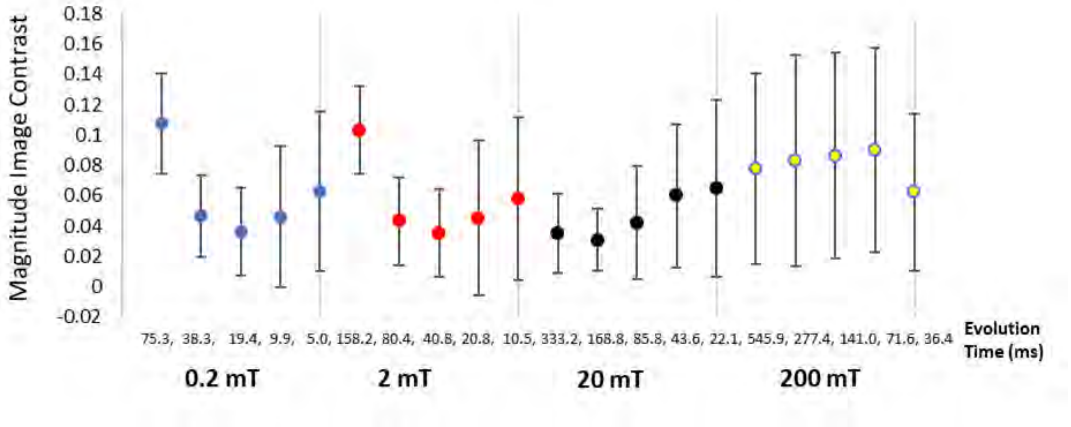

Fig. 1. Cohort mean ± standard deviation of magnitude image contrast obtained between white matter and white matter hyperintensity regions. The image contrast is shown for each field-cycling MRI image obtained at each evolution time and evolution field.

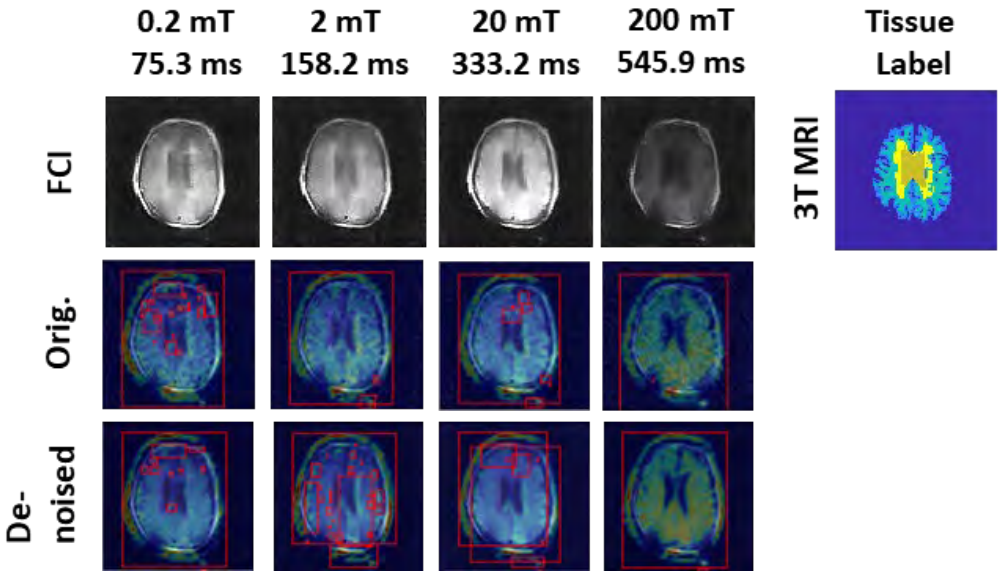

Fig. 2. Classification model highlighted regions of interest for original and denoised field-cycling MRI images of one patient. Saliency maps shown for a number of field-cycling MRI images obtained at different evolution times and evolution fields. Bounding boxes used to annotate saliency maps where map value above a given threshold. Corresponding tissue label from 3T MRI image of same patient is shown.

P-04

Susceptibility weighted imaging of the placenta

Amy Turnbull[a], George Hutchinson[a], Penny Gowland[a],

[a] SPMIC, University of Nottingham

Introduction: The function of the placenta relies on maternal blood, which is rich in oxygen and nutrients, bathing the entire surface of the fetal villi to allow exchange. It has been shown that healthy placentas exhibit slow, uniform flows and homogeneous oxygenation in order to facilitate this exchange [1]. There is a pressing need for a simple clinical measure that provides sensitivity to the distribution of oxygenated blood over the whole placenta. It has been shown that T2*, which is sensitive to the variation in oxygenation and absolute oxygenation as well as other factors, is a potential marker of placental compromise [2]. Phase data (and in particular susceptibility mapping) provides an alternative and independent measure of oxygenation from within the placenta. The aim of this work is to develop SWI images of the placenta combining T2* and phase data, and ultimately to test whether SWI will provide additional sensitivity to the absolute oxygenation as well as the local variation in oxygenation.

Method: Six participants, 35 ± 5 weeks pregnant were imaged at 3T using echo planar imaging at four echo times: 20ms, 25ms, 30ms and 35ms. The decay of the signal magnitude across the echo times was used to generate T2* maps using a weighted, linear least squares fit to the model:

$$\ln(S) = \ln(S_0) - \frac{TE}{T2^*}$$

The phase was then unwrapped, subtracted from the average of the slice to retain the variation then normalised to between 1 and -1. This was combined with the T2* maps to create susceptibility weighted images.

Results: Susceptibility weighted images were obtained for all six participants (figure 1). Histograms of T2* and SWI across the entire placenta ROI were made (Figure 2).

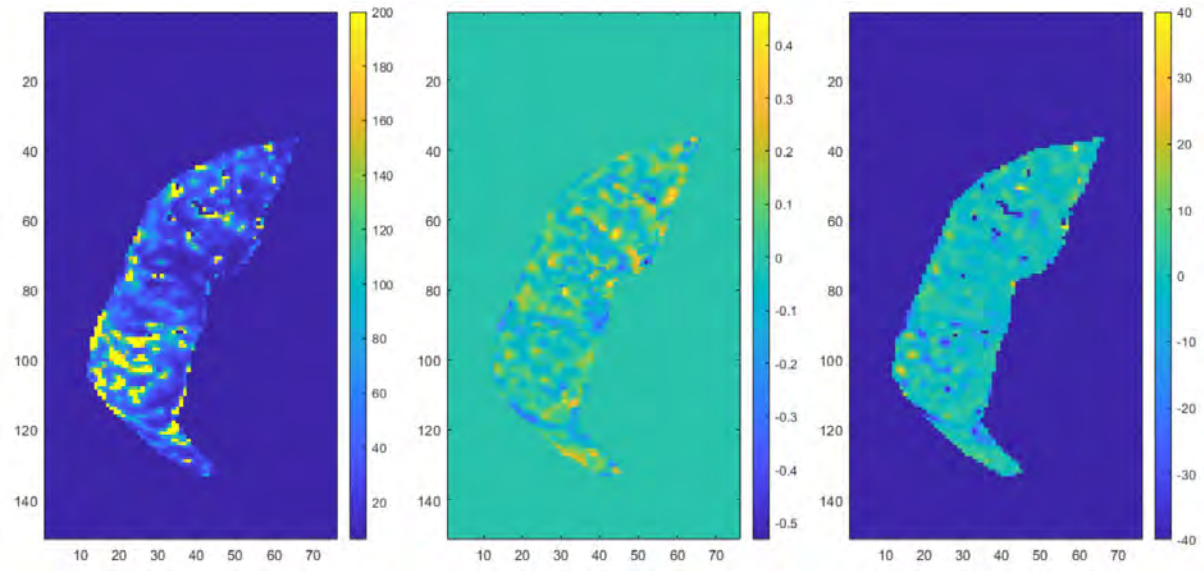

Fig. 1. Masked placenta taken from the transverse plane with maternal side on the left and fetal side on the right, a) T2* map, b) phase map, c) susceptibility weighted image.

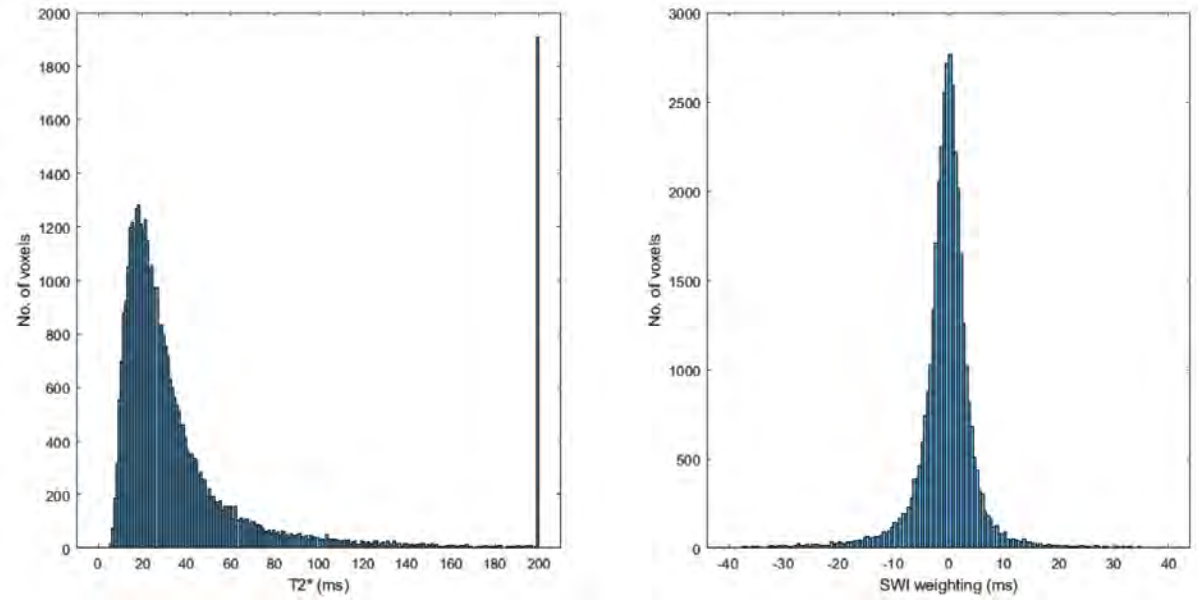

Fig. 2. A) Histogram of T2* values for one subject and B) associated SWI weighting.

Subject	T2* mean	T2* FWHM	SWI mean	SWI FWHM
001	**33.5**	**15 ± 1**	**0.02**	**2.0 ± 0.5**
002	**64.4**	**27 ± 1**	**-0.19**	**5.5 ± 0.5**
003	**52.7**	**25 ± 1**	**-0.42**	**5.0 ± 0.5**
004	**58.5**	**24 ± 1**	**-0.40**	**5.5 ± 0.5**
005	**42.4**	**22 ± 1**	**-0.48**	**5.0 ± 0.5**
006	**72.2**	**39 ± 1**	**-0.20**	**5.0 ± 0.5**

Table 1. Table showing the mean and full width half maximum of the T2* and SWI histograms for each subject.

Discussion: Susceptibility weighting imaging of healthy placentas is feasible and shows a consistent distribution between healthy participants. Further work will repeat this analysis using susceptibility mapping, consider alternative ways of combining the data and considering the local relationship between T2* and susceptibility.

Conclusions: Susceptibility weighted imaging could provide valuable measures of the mixing of oxygenated and deoxygenated blood in the placenta, indicating efficiency of placental function. This could help to identify impaired placental function, helping to inform when intervention is needed.

Acknowledgements: funding for Amy's PhD is from the EPSRC.

References

[1] Dellschaft, N. S., Hutchinson, G., Shah, S., Jones, N. W., Bradley, C., Leach, L., Platt, C., Bowtell, R., & Gowland, P. A. (2020). The haemodynamics of the human placenta in utero. *PLOS Biology*, *18*(5), e3000676. https://doi.org/10.1371/journal.pbio.3000676

[2] Sørensen, A., Hutter, J., Seed, M., Grant, P. E., & Gowland, P. (2020). T2*-weighted placental MRI: basic research tool or emerging clinical test for placental dysfunction? *Ultrasound in Obstetrics & Gynecology*, *55*(3), 293–302. https://doi.org/10.1002/uog.20855

P-05

Quantitative Susceptibility Mapping in the Head and Neck: An Optimized and Repeatable Reconstruction Pipeline

Matthew T. Cherukara[1], Karin Shmueli[1]
[1]Medical Physics and Biomedical Engineering, University College London, London, UK

Introduction: Quantitative susceptibility mapping (QSM) can be used to calculate the magnetic susceptibility of tissues from the MRI signal phase [1,2] and has recently been extended from the brain to other regions of the body [3]. QSM also has potential applications in the head and neck (HN); however, this anatomical region presents unique challenges for QSM, including fat-water phase artefacts, flow effects, physiological motion, and the presence of multiple air-tissue interfaces. For tissue susceptibility values provided by QSM to be clinically useful, the acquisition and reconstruction process must be repeatable. Previous work has been undertaken to develop an optimized HN QSM pipeline [4], and here we present further improvements, incorporating the latest developments in the different stages of the QSM reconstruction pipeline, and test the repeatability of the optimized HN QSM pipeline.

Methods: Multi-echo HN QSM images from 10 healthy volunteers (acquired under local ethics committee approval as part of a previous study [4]) were used to test the repeatability of 20 different QSM reconstruction pipelines. Each subject was scanned in three times per session, for two sessions one week apart. Data were acquired on a 3T Achieva system (Philips, Netherlands) with a 16-channel HN receiver coil, using a 3D GRE sequence. A coronal orientation with a SENSE acceleration factor of 2 in the first phase-encoding direction and 1.25 mm isotropic resolution were used. In-phase echo timing with four echoes (TE_1 = ΔTE = 4.61 ms) was used to reduce fat-water chemical shift effects.

Multi-echo images were combined using non-linear field fitting [5,6], and in the remaining stages of the QSM reconstruction pipeline (phase unwrapping, background field removal, and susceptibility calculation) multiple methods were tested based on recent literature [7,8]. Phase unwrapping methods tested were: Laplacian phase unwrapping (LPU) [6], a region-growing method (SEGUE) [9], and a path-based method (ROMEO) [10]. Background field removal methods tested were projection onto dipole fields (PDF) [11] and V-SHARP [12,13]. Susceptibility calculation methods tested were: an iterative Tikhonov-regularized inversion (iTik) [2,4], direct Tikhonov-regularized inversion (dTik), FANSI [14], Star-QSM [15], Weak-harmonic regularized FANSI [14,16], and L1-QSM [17]. Processing and analysis were conducted in MATLAB (MathWorks, Natick, MA).

Susceptibility maps were reconstructed for a single subject using the previously optimized 'old' pipeline (LPU, PDF, iTik) [4] and with each stage varied in turn. Regions of interest (ROIs) in the brain (thalamus, caudate nucleus, putamen, globus pallidus) and head and neck (parotid gland, submandibular gland, and several lymph nodes) were obtained by a combination of automatic segmentation using FSL FIRST [18] and manual segmentation (checked by an experienced radiologist). Pairwise differences in average susceptibility in each ROI were calculated between scans in the same session, or between sessions, and the distributions of these differences were used as a measure of intra-session and intersession repeatability, respectively.

Results: Visual assessment, and distributions of susceptibility values in HN ROIs, were used as an initial comparison between different techniques for the three stages of QSM reconstruction. A 'new' optimized pipeline consisting of ROMEO phase unwrapping, V-SHARP background field removal (An optimal V-SHARP kernel size (22 mm) was found by maximising contrast between susceptibility values in brain ROIs), and iTik susceptibility calculation, was compared with the 'old' pipeline for intra-session and inter-session repeatability. Fig. 1 shows the results of this comparison. The new pipeline resulted in lower variation in susceptibility values both within and between sessions, in most HN ROIs.

Discussion: Several HN QSM reconstruction pipelines based on state-of-the-art methods were compared before selecting an optimised 'new' pipeline which was tested in 10 subjects and found to have higher intra-session and intersession reliability than previous best results. Laplacian phase

unwrapping is inexact, and prone to underestimating phase contrast in areas of noise or near the tissue boundaries; therefore, we used, a path-based method (ROMEO) as it provides exact unwrapping with no major errors in tissue areas of interest. Background field removal using PDF led to less homogeneous susceptibility values in tissues expected to be uniform, especially close to the edge of the mask. V-SHARP appeared to remove residual background fields at the edges more effectively and led to more uniform susceptibility values in muscle tissue. Tikhonov-regularized susceptibility calculation produced susceptibility maps with minimal streaking artefacts (compared with FANSI and L1-QSM), less noise in the neck (compared with Star-QSM), and more expected levels of tissue contrast in the brain (compared with WH-FANSI).

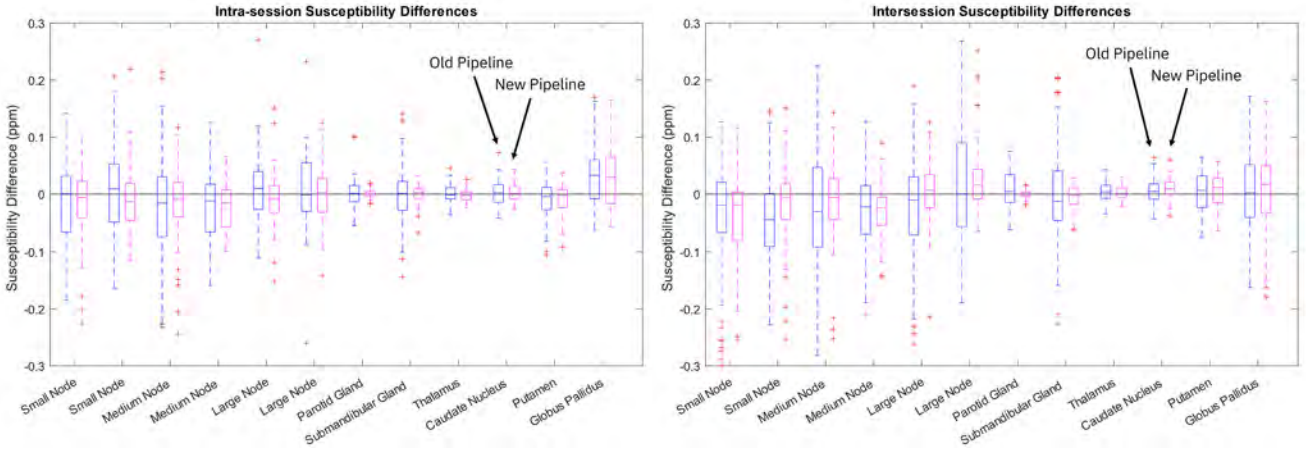

Fig. 1. Intra-session (left) and inter-session (right) differences in susceptibility values in HN ROIs, comparing a previously optimised reconstruction pipeline (blue) with a new pipeline (magenta).

Conclusions: A wide range of algorithms exist for the different parts of the QSM reconstruction pipeline [3,7,8]; however, the factors which confound susceptibility measurements vary throughout the body, so, for a given application, it is essential that an optimal reconstruction pipeline be determined. We compared a range of QSM algorithms and found a pipeline which produces repeatable susceptibility values in key ROIs in the brain and HN region.

Acknowledgements: M.T.C. is funded by CRUK multidisciplinary award 24348. K.S. is funded by ERC consolidator grant DiSCo MRI SFN 770939.

References

[1] K. Shmueli et al., *Magn. Reson. Med*. **62**, 1510-1522 (2009).
[2] Y. Wang and T. Liu., *Magn. Reson. Med*. **73**, 82-101 (2015).
[3] A. V. Dimov et al., *J. Magn. Reson. Imag.* **57**, 1621-1640 (2023).
[4] A. Karsa, S. Punwani, and K. Shmueli, *Magn. Reson. Med*. **84**, 3206-3222 (2020).
[5] T. Liu et al., *Magn. Reson. Med*. **69**, 467-476 (2013).
[6] Cornell MRL. *MEDI toolbox*: http://weill.cornell.edu/mri/pages/qsm.html [accessed 27/06/2023]
[7] S. D. Robinson et al., *NMR in Biomed*. **30**, 3601 (2017)
[8] F. Schweser et al., *NMR in Biomed*. **30**, 3604 (2017)
[9] A. Karsa and K. Shmueli. *IEEE Trans. Med. Imag.* **38**, 1347-1357 (2019).
[10] B. Dymerska et al., *Magn. Reson. Med.* **85**, 2294-2308 (2021).
[11] T. Liu et al., *NMR in Biomed.* **24**, 1129-1136 (2011).
[12] B. Wu, W. Li, A. Guidon, and C. Liu. *Magn. Reson. Med.* **67**, 137-47 (2012)
[13] C. Liu, *STI Suite*: https://people.eecs.berkeley.edu/~chunlei.liu/software.html [accessed 27/06/2023]
[14] C. Milovic et al., *Magn. Reson. Med.* **80**, 814-821 (2018).
[15] H. Wei et al., *NMR in Biomed.* **28**, 1294-1303 (2015).
[16] C. Milovic et al., *Magn. Reson. Med.* **81**, 1399-1411 (2019).
[17] C. Milovic et al., *Magn. Reson. Med.* **87**, 457-473 (2022).
[18] B. Patenaude, S. M. Smith, D. Kennedy, and M. Jenkinson, *NeuroImage* **56**, 907-922 (2011).

P-06

CSF and Whole Brain Referencing has Mixed Efficacy in Head and Neck versus Whole Brain Quantitative Susceptibility Mapping

Matthew T. Cherukara[1], Karin Shmueli[1]

[1]Medical Physics and Biomedical Engineering, University College London, London, UK

Introduction: Quantitative susceptibility mapping (QSM) can be used to calculate the magnetic susceptibility, χ, of tissues from the MRI signal phase [1,2]; however, these values are not absolute and may be affected by an arbitrary constant shift which is not accounted for by k-space dipole inversion [3]. In order to compare susceptibility estimates across subjects or centres, many studies reference χ values to a reference region [4]. In the brain in healthy subjects, cerebrospinal fluid (CSF) in the ventricles is often chosen as the reference region [4]. It is assumed that referencing χ values to such a region will remove subject-based or scanner-dependent inconsistencies. Background field removal is a key stage in the QSM reconstruction pipeline and is highly dependent on the mask region chosen. Therefore, we might expect χ maps calculated over different mask regions in the same subject to have different offsets. However, if both QSMs are referenced to the same region, we might hypothesise that any constant shift in χ should be corrected. In this work, we show that referencing is of mixed efficacy in providing consistent χ estimates, if there are differences in mask region.

Methods: Multi-echo 3D GRE data were acquired from 10 healthy volunteers, as part of a previous study [6], on a 3T Achieva system (Philips, Netherlands) using a 16-channel head-and-neck (HN) receiver coil. A coronal orientation with a SENSE acceleration factor of 2 in the first phase-encoding direction and 1.25 mm isotropic resolution was used. QSM images were reconstructed using the following pipeline: A brain mask was generated from magnitude images using FSL BET [7]; multi-echo images were combined using non-linear field fitting [8,9]; phase data were unwrapped using ROMEO [10]; background fields were removed using V-SHARP with a maximum kernel diameter of 22 mm [11,12]; and χ was calculated using an iterative Tikhonov-regularized inversion [6]. Deep-brain regions of interest (ROIs – thalamus, caudate nucleus, putamen, and globus pallidus) were automatically segmented using FSL FIRST [13], and the atria of the lateral ventricles were manually segmented for CSF referencing.

For each subject, two QSM images were reconstructed: once for the whole HN region, and once with the brain mask applied. Means and standard deviations of χ values in deep-brain ROIs were calculated for both data sets 1) without referencing, 2) after subtracting the whole brain mean χ, and 3) after subtracting the mean CSF χ. For each ROI, the difference between whole HN and brain-only ROI mean χ was calculated for all three referencing conditions, and two-tailed t-tests were used to test for statistically significant differences between whole HN and brain-only distributions of χ values for all three referencing conditions. All analyses were carried out in MATLAB (MathWorks, Natick, MA).

Results: The atria of the lateral ventricles had χ = 0.044 ± 0.022 ppm (mean ± s.d.) in brain-only QSM, and χ = 0.047 ± 0.027 ppm in whole HN QSM, with a low variance as expected. The caudate nucleus and thalamus had the lowest variance within ROIs and across subjects, so they were selected as exemplars for further analysis. Fig. 1 shows the absolute difference in mean χ between whole HN and brain-only QSMs for both the CN and thalamus and all three referencing conditions. In the CN, 7 of 10 subjects had statistically significantly different χ distributions between unreferenced HN and brain-only QSMs, reducing to 6 of 10 subjects after CSF referencing. In the thalamus, 6 of 10 subjects had statistically significantly different χ distributions between unreferenced QSMs, and 6 of 10 subjects had different χ distributions between CSF-referenced QSMs (not all the same subjects). It was hypothesised that referencing would remove any differences in ROI χ values due to differing mask regions; however, Fig. 1. shows that this was not consistently the case: In 2 of 10 subjects, referencing to CSF reduced the difference in mean χ between HN and brain-only QSMs in both ROIs. In a further 6 subjects, referencing reduced the difference in one of the two ROIs. In the final 2 subjects, referencing to CSF increased the difference in both ROIs. Referencing to the whole-brain mean χ did not significantly reduce differences in χ distributions between QSMs in any subjects.

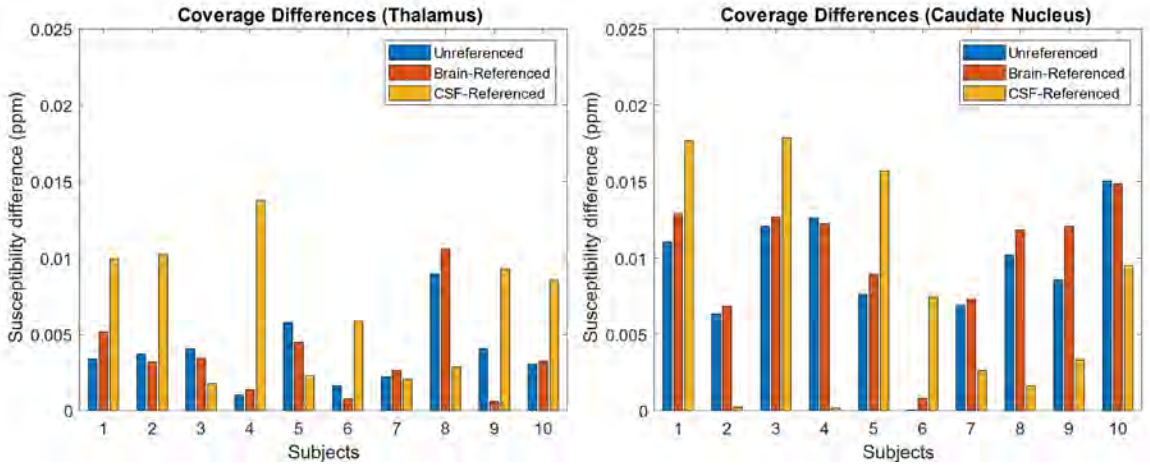

Fig. 1. Absolute difference in average caudate nucleus (left) and thalamus (right) susceptibility between brain-only and whole head-and-neck QSM, for unreferenced, brain-referenced, and CSF-referenced data.

Discussion: Quantitative susceptibility maps were reconstructed from whole HN or brain-only data, and χ distributions in the CN and thalamus were compared. The mask region (HN or brain only) significantly affected χ distributions in these ROIs in the majority of subjects. This result is consistent with previous studies comparing whole-brain masking to retrospective reconstruction in a smaller mask region [14,15]. These differences are likely to be the result of differences in background removal, leaving different levels of residual background fields.

The possibility of using CSF or whole brain referencing to overcome these differences was investigated. While group-level differences were not large enough for statistical significance, on the individual level, referencing to CSF had mixed results in the majority of subjects. This may be due to the previously reported limitations of CSF referencing: partial volume effects, flow artefacts, or the presence of the choroid plexus [3,5]. Referencing to the whole brain did not offer any improvement, which may be due orientation dependent contributions from white matter [16].

Conclusions: Referencing to CSF or the whole brain did not consistently overcome differences in QSM resulting from changes in masking region. Care is needed when making group-level comparisons of susceptibility values, and the choice of reference region should be investigated carefully for every application.

Acknowledgements: M.T.C. is funded by CRUK multidisciplinary award 24348. K.S. is funded by ERC consolidator grant DiSCo MRI SFN 770939.

References

[1] K. Shmueli et al., *Magn. Reson. Med*. **62**, 1510-1522 (2009).
[2] Y. Wang and T. Liu., *Magn. Reson. Med*. **73**, 82-101 (2015).
[3] Z. Liu, P. Spincemaille, Y. Yao, Y. Zhang, and Y. Wang, *Magn. Reson. Med.* **79**, 2795-2803 (2018).
[4] I. A. L. Lim, et al., *NeuroImage* **82**, 449-469 (2013).
[5] S. Straub, et al., *Magn. Reson. Med*. **78**, 204-214 (2017).
[6] A. Karsa, S. Punwani, and K. Shmueli, *Magn. Reson. Med*. **84**, 3206-3222 (2020).
[7] S. M. Smith, *Human Brain Mapping* **17**, 143-155 (2002).
[8] T. Liu et al., *Magn. Reson. Med*. **69**, 467-476 (2013).
[9] Cornell MRL. *MEDI toolbox*: http://weill.cornell.edu/mri/pages/qsm.html [accessed 27/06/2023]
[10] B. Dymerska et al., *Magn. Reson. Med.* **85**, 2294-2308 (2021).
[11] B. Wu, W. Li, A. Guidon, and C. Liu. *Magn. Reson. Med.* **67**, 137-47 (2012)
[12] C. Liu, *STI Suite*: https://people.eecs.berkeley.edu/~chunlei.liu/software.html [accessed 27/06/2023]
[13] B. Patenaude, S. M. Smith, D. Kennedy, and M. Jenkinson, *NeuroImage* **56**, 907-922 (2011).
[14] A. Karsa, S. Punwani, and K. Shmueli, *Magn. Reson. Med*. **81**, 1833-1848 (2019).
[15] A. M. Elkady, H. Sun, A. H. Wilman, *J. Magn. Reson. Imag.* 34, 574-578 (2016).
[16] F. Schweser, et al., *NeuroImage* **167**, 438-452 (2018).

P-07

Impact of reference region choice on statistical analysis in QSM

Patrick Fuchs[a], Carlos Milovic[b], Oliver C Kiersnowski[a], Karin Shmueli[a]

[a]Department of Medical Physics and Biomedical Engineering, University College London, London, UK.
[b]School of Electrical Egineering, Pontificia Universidad Catolica de Valparaiso, Valparaiso, Chile.

Introduction: The goal of quantitative magnetic susceptibility mapping (QSM)[1] is to reconstruct the magnetic susceptibility of tissue from the phase of the MRI signal. Brain QSM is often used to investigate, for example, iron content in various deep grey matter regions. Due to the nature of the relationship between the measured phase and the underlying susceptibility distribution, it is not possible to reconstruct the absolute susceptibility. Rather, we typically (implicitly) reconstruct a relative susceptibility with respect to some "mean" susceptibility value that is often assumed to be close to the average susceptibility of tissue or water within a region of interest.

QSM shows good reproducibility and repeatability when comparing scans with matched acquisitions and equal processing pipelines[2]. However, there could be a systematic bias with respect to this implicit reference (the "mean" susceptibility). Some argue that trading this implicit bias for an explicit bias with respect to a well understood reference region will help reinforce the quantitative nature of the susceptibility contrast[3]. Often, the cerebrospinal fluid (CSF) is used as a reference as it has been shown to be largely unaffected by disease or age and has a relatively uniform susceptibility[4].

In clinical QSM studies, the primary means of investigating susceptibility related effects is to compare regional mean susceptibility values between groups of patients and healthy controls. Here, we look at the influence of reference regions on statistical tests in a QSM study of temporal lobe epilepsy (TLE).

Methods: We investigated two global reference regions: the whole brain (from the brain mask used in the background field removal step in QSM) and one based on variance (RelVar, described below), not anatomy; and two local regions: CSF and a white matter region (corpus callosum, CC). The cohort consisted of 27 healthy controls, 19 patients with left TLE and 17 with right TLE, with ages ranging from 16 to 67 years old[5]. All subjects were scanned on a 3T GE Discovery MR750 system with a 1mm isotropic inversion recovery (T1) fast spoiled gradient-recalled echo sequence ($T_E{:}\,T_R{:}\,T_I = 3.1{:}\,7.4{:}\,400\,ms$), and a 3D gradient-echo (SWAN) sequence with 0.52 x 0.52 x 1.2 mm voxels, 5 echoes $\left(T_{E_1}{:}\,\Delta T_E{:}\,T_{E_5} = 12.9{:}\,5{:}\,32.8\,ms\right)$, $T_R = 37.1\,ms$, $FA = 15°$.

Susceptibility maps were reconstructed by a non-linear fit[6] of the SWAN complex data, Laplacian phase unwrapping[7], background field removal with projection onto dipole fields[8] and dipole inversion using the weak-harmonic non-linear total variation method from FANSI[9].

Statistical tests were performed using Matlab 2023a on 13 brain regions of interest that were segmented using geodesic information flows (GIF)[10] and HippoSeg[11] for the hippocampus. A relative variance map was generated using ANTs[12] following [13] (and thresholded at the 2nd percentile to provide a RelVar reference region), and a whole brain mask was obtained via Otsu thresholding the magnitude information[14] (which was also used In the QSM pipeline). Outliers were removed from all segmentations by removing voxels with susceptibility smaller than the 1st percentile or larger than the 99th percentile of the susceptibilities within an ROI. Before statistical testing, the data were age corrected using a linear fit across control participants in the ROIs.

Before performing age correction and statistical testing, referencing was performed by subtracting the mean susceptibility of each reference region from the whole brain (i.e. all ROIs). Groupwise analysis of variance (ANOVA) and post-hoc between-group Tukey's range testing (corrected for multiple between-group comparisons) were performed.

Results: In Figure 1, groupwise differences can be identified: only ROIs with a groupwise p-value close to being significant (< 0.2) are shown in this figure, orange values are considered statistically significant (at a 0.05 threshold). In Figure 2 the results of Tukey's range test can be found for the same ROIs as presented in Figure 1. The corpus callosum (CC) has a significantly between group difference, which is

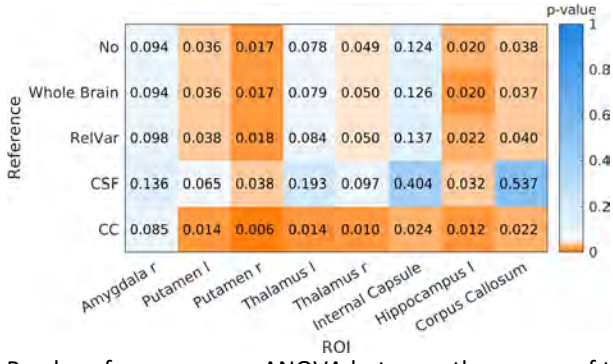

***Fig. 1.* Groupwise analysis.** P-values from one-way ANOVA between the means of the three groups of subjects (healthy control, left- and right-temporal lobe epilepsy). The p-values are for the null hypothesis that the means of the groups are equal. P-values below 0.05 are coloured in orange to signify significant between group differences. Rows are different reference regions, and columns are the deep grey matter ROIs.

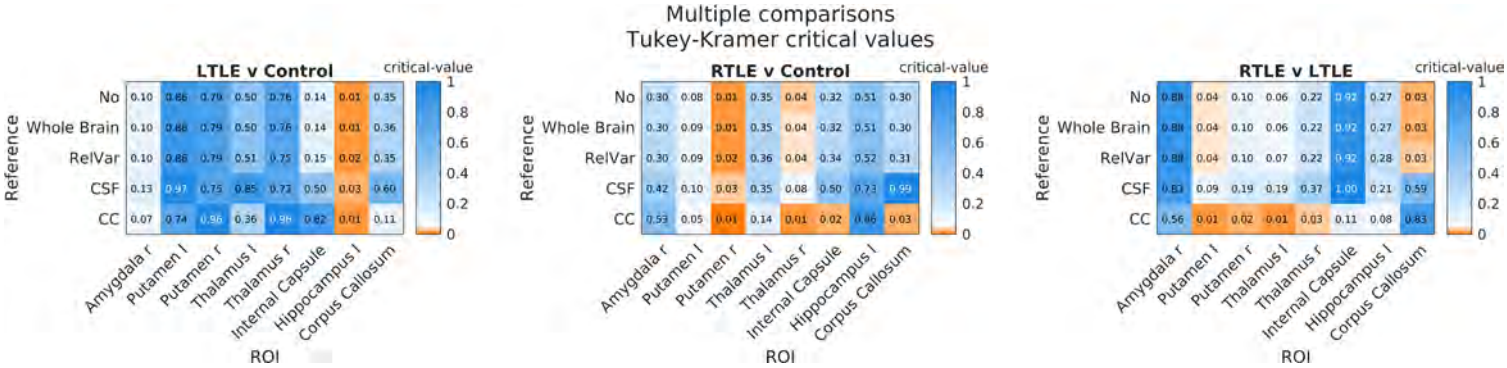

Fig. 2 Between group analysis. Critical values of Tukey's range test, orange denotes statistically significant differences (below 0.05). LTLE and RTLE are left and right temporal lobe epilepsy groups.

clearly seen in Figures 1 (top row, p-value of 0.038) and 2 (between RTLE and LTLE).

Conclusions Due to its significant difference the CC is a bad choice of reference region, as it will increase the number of significant groupwise ROI differences introducing bias. The whole-brain and RelVar reference regions had little impact on the statistical results. Using the CSF reference region reduced significant between-group susceptibility differences (Figure 1). This suggests that some of the between-group variation could be due to bias, and/or because the estimate of the mean of the CSF is noisy, thereby increasing the (sample) variance of the test statistic and thus decreasing the effect size.

Acknowledgements: The authors would like to thank Dr. Jon Clayden for his valuable discussions on our statistical analysis, John Duncan, Gavin Winston and Sjoerd Vos for allowing our use of the epilepsy dataset. PF and KS are supported by ERC Consolidator Grant DiSCo MRI SFN 770939. OK was supported by the EPSRC Doctoral Training Partnership (EP/R513143/1).

References

[1] Shmueli K. Quantitative Magnetic Resonance Imaging. 1st ed. Elsevier; 2020.
[2] Feng, X., Deistung, A., & Reichenbach, J. R. (2018). Zeitschrift für Medizinische Physik, 28(1), 36-48.
[3] P. Ravanfar et al., Frontiers in Neuroscience, vol. 15, 2021, doi: 10.3389/fnins.2021.618435.
[4] S. Straub et al., Magnetic Resonance in Medicine, vol. 78, no. 1, 2017, doi: 10.1002/mrm.26369.
[5] O. C. Kiersnowski et al., ISMRM Annual Meeting 2021, P. 1033
[6] Liu T, et al. Magn Reson Med. 2013;69(2):467-476. doi: 10.1002/mrm.24272
[7] Schofield and Zhu, 2003 M.A. Schofield and Y. Zhu, , Opt. Lett. 28 (2003), pp. 1194-1196
[8] T. Liu et al. NMR Biomed 2011;24(9):1129-36
[9] Milovic, C, et al., Magn Reson Med. 2019;. https://doi.org/10.1002/mrm.27483
[10] Cardoso MJ, Modat M, Wolz R, et al. IEEE Trans Med Imaging. 2015;34(9) doi:10.1109/TMI.2015.2418298
[11] Winston GP, Cardoso MJ, Williams EJ, et al. Epilepsia. 2013;54(12):2166-2173. doi:10.1111/epi.12408
[12] Avants, Brian B., Nick Tustison, and Gang Song. Insight j 2.365 (2009): 1-35.
[13] J. Acosta-Cabronero, et al., J. of Neur, 2016, doi: 10.1523/JNEUROSCI.1907-15.2016.
[14] Otsu N. IEEE Trans 46 Syst Man Cybern. 1979;9(1):62-66.

P-08

Investigating 'Inverse' Positive Activations in functional quantitative susceptibility mapping (fQSM)

Jannette Nassar[1], Oliver C. Kiersnowski[1], Patrick Fuchs[1], Karin Shmueli[1]
[1]Department of Medical Physics and Biomedical Engineering, University College London, UK

Introduction: Conventional magnitude-based blood oxygen level-dependent (BOLD) fMRI is a well-established and widely used neuroimaging technique, while functional quantitative susceptibility mapping (fQSM) [1], [2] represents a novel approach that may provide more localized activations.
In normal circumstances, in response to neuronal activation, BOLD fMRI and fQSM exhibit positive and negative signal changes, respectively, due to the decrease in paramagnetic deoxyhaemoglobin concentration on functional hyperaemia. However, in certain cases, a perplexing phenomenon has emerged, where the observed fQSM activations are contrary to the expected pattern, appearing as positive activations instead, negatively correlating with the stimulus [1]–[5] he occurrence of these 'inverse' activations raises intriguing questions about their underlying mechanism and requires further investigation.

Methods: 70 volumes of multi-echo 2D GRE EPI were acquired in a healthy 30-year-old male volunteer using a 3T Siemens-Prisma scanner and a 64-channel head coil, with the parameters and stimulus protocol in Figure 1. To maximize the BOLD signal, a standard visual stimulation paradigm with a conventional block design was used. Data processing steps included calculating brain masks at every volume using FSL BET [6] on the second echo magnitude images. For fMRI, the multi-echo magnitude images were combined using T_2*-weighted echo summation [7]. For fQSM, susceptibility maps were calculated from the phase images at each timepoint: the total field map was calculated using a non-linear fit of the complex data [8] plus Laplacian unwrapping [9]; intra-slice background fields were removed with 2D+3D V-SHARP [10] followed by 3D-PDF [11] to remove through-slice fields [12]. Susceptibility maps were then computed using non-linear total variation regularisation (FANSI, $\alpha = 2x10^{-4}$) [13]. fQSM processing was performed on absolute susceptibility maps, to minimise the impact of opposite sign cancellation of neighbouring voxels on smoothing [14].
Functional Analysis: SPM12 [15] was used for fMRI and fQSM. Spatial pre-processing included rigid-body realignment of the magnitude images to the first image in the time-series to correct for motion, with the resulting transformations applied to corresponding susceptibility maps and masks, and spatial smoothing with an 8 mm FWHM Gaussian kernel to improve SNR and increase statistical power [16]. A general-linear model (GLM) was reconstructed with a regressor for the visual stimuli. Statistically significant changes were detected by voxel-wise t-tests. fMRI and fQSM activation maps were generated using a threshold of $p<0.001$ without FWE correction or imposing a minimum cluster size restriction, allowing for the visualisation of individual supra-threshold voxels.

Results & Discussion: In addition to expected susceptibility decreases on activation, the analysis showed unexpected increases in susceptibility (positive activations) in fQSM (Fig. 2). All fMRI activations were more extensive and higher amplitude than the corresponding fQSM activations. Previous studies suggest explanations for positive fQSM activations including QSM reconstruction artifacts such as incomplete dipole inversion [1, 2], particularly near high susceptibility sources like veins. The inverse fQSM activations observed here were not close to large veins.

Conclusions: We observed 'inverse' activations in both BOLD fMRI and fQSM. This challenges the conventional paradigm of neuronal activation detection and highlights the need for further research into their underlying mechanisms.

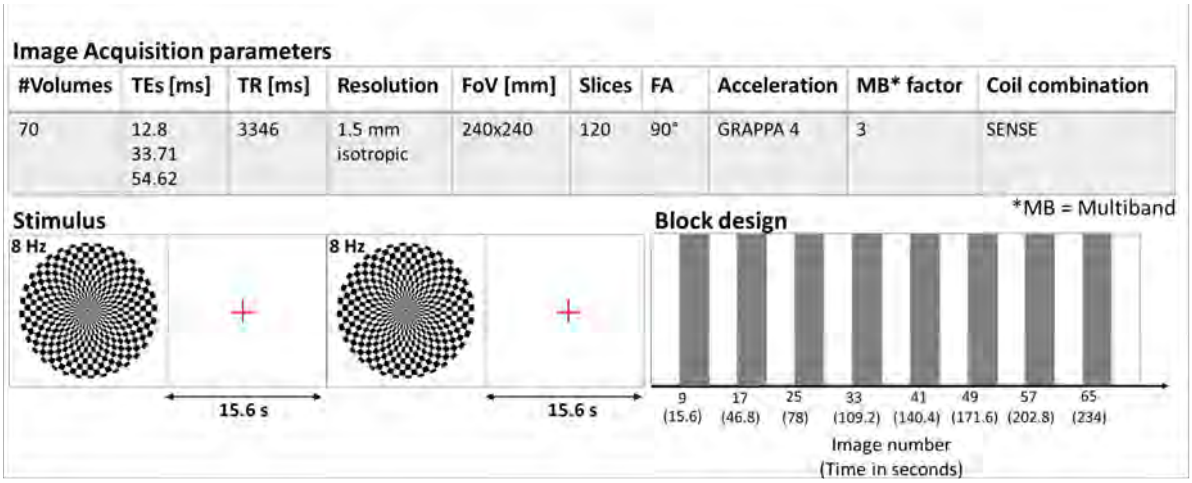

Fig. 1. **Image acquisition parameters**

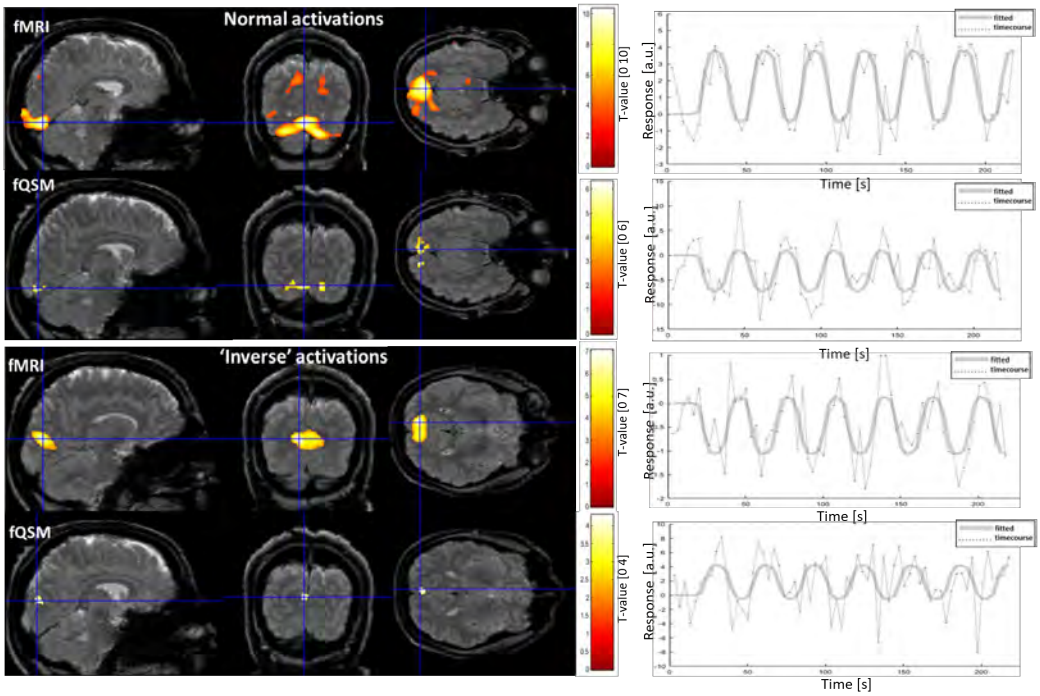

Fig. 2. **Normal and 'Inverse' activations**: normal activations consisting of positive fMRI (first row) and negative fQSM (second row) activated voxels, and 'inverse' activations consisting of negative fMRI (third row) and positive fQSM (forth row) activated voxels are shown in all three orientations, overlayed on the combined-echo magnitude images from the first timepoint.

References

[1] P. S. Özbay *et al.*, *NeuroImage*, vol. 137, pp. 52–60, Aug. 2016.
[2] D. Z. Balla *et al.*, *NeuroImage*, vol. 100, pp. 112–124, Oct. 2014.
[3] M. Bianciardi *et al*, *Hum. Brain Mapp.*, vol. 35, no. 5, pp. 2191–2205, May 2014.
[4] Z. Chen *et al*, *J. Neurosci. Methods*, vol. 261, pp. 161–171, Mar. 2016.
[5] M. Lancione *et al.*, *NeuroImage*, vol. 244, p. 118574, Dec. 2021.
[6] S. M. Smith, *Hum. Brain Mapp.*, vol. 17, no. 3, pp. 143–155, Nov. 2002.
[7] B. A. Poser *et al*, *Magn. Reson. Med.*, vol. 55, no. 6, pp. 1227–1235, 2006.
[8] T. Liu *et al*, *Magn. Reson. Med.*, 2013.
[9] M. A. Schofield *et al*, *Opt. Lett.*, vol. 28, no. 14, pp. 1194–1196, Jul. 2003.
[10] W. Li *et al*, *NeuroImage*, vol. 55, no. 4, pp. 1645–1656, Apr. 2011.
[11] T. Liu *et al.*, *NMR Biomed.*, vol. 24, no. 9, pp. 1129–1136, Nov. 2011.
[12] H. Wei *et al*, *NMR Biomed.*, vol. 30, no. 4, Apr. 2017.
[13] Milovic et al, Magnetic Resonance in Medicine - Wiley Online Library, 2018.
[14] M. J. Betts *et al*, *NeuroImage*, vol. 138, pp. 43–63, Sep. 2016.
[15] K. J. Friston *et al*, *Hum. Brain Mapp.*, vol. 2, no. 4, pp. 189–210, 1994.
[16] M. K. Chung, arXiv, Nov. 29, 2021.

P-09

Comparison of Bipolar Gradient Phase Offset Correction Methods for Quantitative Susceptibility Mapping

Mitchel Lee[a], Fenella Kirkham[b], Karin Shmueli[a]
[a]Department of Medical Physics and Biomedical Engineering, University College London, London, United Kingdom [b]Imaging and Biophysics, Developmental Neurosciences, UCL Great Ormond Street Institute of Child Health, London, United Kingdom

Introduction: Quantitative Susceptibility Mapping (QSM) uses phase information from the complex MRI signal to estimate the underlying magnetic susceptibility of the imaged tissue. Multi-echo gradient echo (ME-GRE) sequences are often used for QSM, typically with echoes acquired at a single gradient polarity, known as a monopolar acquisition. This requires 'fly-back' gradients between the echo readouts, which increase echo spacing and acquisition time. Acquisition efficiency can be improved using a bipolar acquisition, in which echo readouts are acquired with gradients of alternating polarity. However, the alternating readout direction can lead to phase discrepancies between the odd and even echoes, due to gradient delays and eddy currents. Failure to correct for these phase offsets may lead to errors during QSM processing. Here, we aimed to compare the performance of two phase offset correction methods.

Methods: Five healthy volunteers (aged 17.1 ± 5.5 years) were imaged with a multi-parametric mapping (MPM) acquisition [1] and a conventional ME-GRE sequence. Each of the MPM sequences were acquired using bipolar readout gradients, whereas the ME-GRE used monopolar gradients.

The T1-weighted FLASH sequence of the MPM acquisition had bipolar gradients, a 240x256x176 matrix, 1 mm isotropic resolution, 24.5 ms TR, 2.34 ms TE_1 and ΔTE, 8 echoes, 21° flip angle, and 465 Hz/pixel bandwidth.

MPM susceptibility maps were calculated from the T1-w sequence without any phase offset correction and then recalculated using two different correction methods. These were: Estimating the odd-even phase offset by **linear** fitting along the three spatial dimensions of a phase offset map obtained from the first three echoes [2]; The MCPC-3D-S phase offset correction method included in the **ROMEO** phase unwrapping package [3,4]. All QSM processing was performed using the same processing pipeline [5], other than the MCPC-3D-S offset correction, which used ROMEO unwrapping instead of SEGUE. Difference maps between the resulting QSMs were calculated.

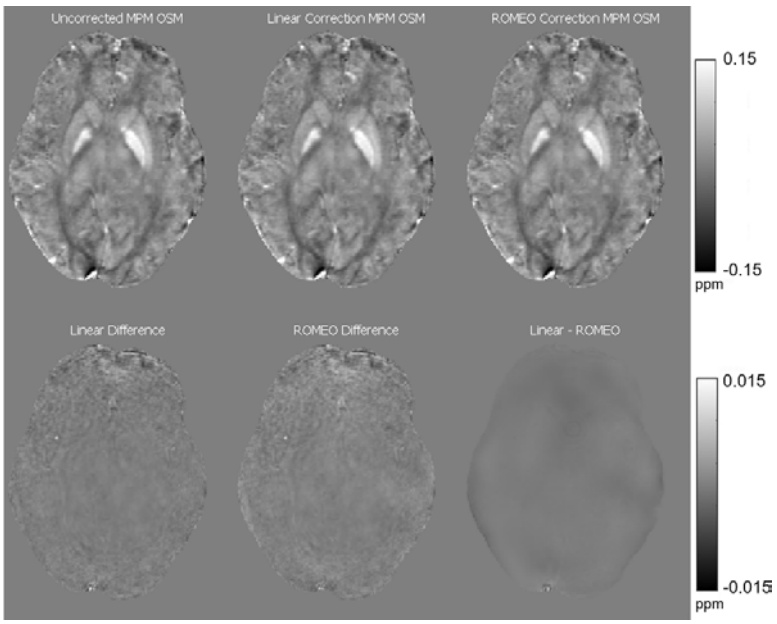

Fig. 1. QSMs calculated from the T1-w MPM sequence with and without the two phase offset corrections and corresponding difference maps. An axial slice is shown in a representative subject.

QSMs were also calculated from the monopolar ME-GRE sequence to provide a reference for the results obtained from the MPM sequence. ME-GRE sequence parameters: 156x192x144 matrix, 1.15 mm isotropic resolution, 38 ms TR, 3 ms TE_1, 4 ms ΔTE, 7 echoes

15° flip angle, 360 Hz/pixel bandwidth. These were processed using the same pipeline as the T1-w MPM sequence.

The ME-GRE QSM was coregistered to the MPM QSMs using FSL FLIRT [6]. Difference maps were then calculated between each of the T1-w MPM QSMs and the coregistered ME-GRE QSM. Whole brain mean absolute differences (MAD) were also calculated to evaluate the similarity between QSMs calculated with different phase offset correction methods.

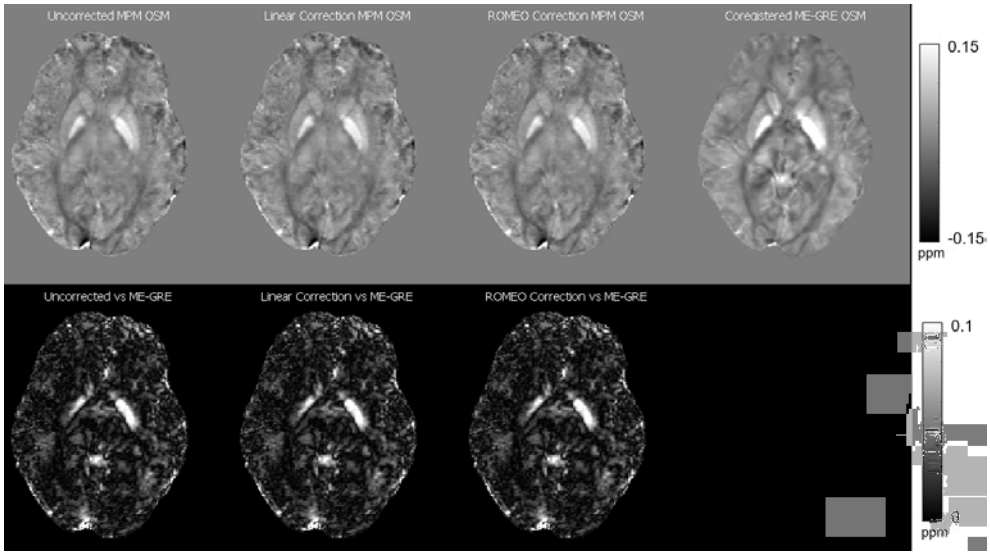

Fig. 2. The coregistered QSM calculated from the ME-GRE sequence shown alongside the MPM QSMs from Figure 1 with corresponding absolute difference maps.

Results: Example QSMs and absolute QSM difference maps are shown in Figure 1. Comparing the whole brain MAD for each correction method relative to the uncorrected MPM QSM, the linear correction had the smallest MAD of 1.11 ± 0.56 ppb. The ROMEO correction method gave a MAD of 1.23 ± 0.52 ppb. The MAD values comparing the MPM QSMs to the coregistered ME-GRE QSM were: Uncorrected: 17.93 ± 2.58 ppb; Linear correction: 17.88 ± 2.59 ppb; ROMEO correction: 17.86 ± 2.57 ppb.

Discussion: The whole-brain MAD values obtained from comparing the corrected and uncorrected MPM QSMs show that the effect of the correction is very small, with the linear and ROMEO corrections having very similar results.

Complete failures in the uncorrected QSMs, as observed in the literature [2], were not observed in this sample, but complete processing of the full cohort (13 healthy controls and 19 patients with sickle cell anaemia), including images from the other two (PD-w and MT-w) MPM sequences, could reveal cases where phase offset correction has a greater effect.

Based on the figures and MAD values between each of the phase-offset corrected MPM QSMs and the ME-GRE QSM, it appears that differences between the two sequences are the dominant contribution. The shorter final echo time in the ME-GRE sequence likely leads to a susceptibility underestimation larger than the scale of any errors due to the bipolar acquisition.

Conclusions: Applying phase offset corrections methods to this MPM sequence acquired using bipolar gradients did not have a substantial effect on QSM. This suggests that either of these phase offset corrections could be applied to QSM data acquired using this bipolar MPM sequence on this system.

References

[1] Tabelow K, et al. , *Neuroimage* 194 (2019): 191-210
[2] Li J et al. , *MAGMA* 28 (2015) : 347-355
[3] Eckstein K et al. , *Magn. Reson. Med* 79.6 (2018): 2996-3006
[4] Dymerska B et al. , *Magn. Reson. Med* 85.4 (2021): 2294-2308
[5] Murdoch R et al. , *Proceedings of the ISMRM Annual Meeting* (2020): 3206
[6] Jenkinson M et al. , *NeuroImage*, 17.2 (2002): 825-841

P-10

Investigating magnetic susceptibility differences in prostate cancer lesions

Laxmi Muralidharan[a], Manju Mathew[b], Adam Retter[b], Shonit Punwani[b], Karin Shmueli[a]

[a]Department of Medical Physics and Biomedical Engineering, University College London, United Kingdom
[b]Centre for Medical Imaging, University College London, United Kingdom

Introduction: Quantitative susceptibility mapping (QSM) has shown potential to measure disease-related changes in tissue iron, myelin, calcifications and oxygenation [1]. Previous QSM studies have investigated its potential to detect intraprostatic calcifications to use as fiducial markers for radiotherapy [2] and post biopsy in prostate cancer (PCa) [3]. Blood's susceptibility is directly proportional to its oxygenation, and low oxygenation (hypoxia) is thought to occur early in the evolution of PCa and is linked to an aggressive phenotype [4]. All this underpins our aim to investigate whether QSM has the potential to help detect and classify lesions in the prostate.

Methods: 20 patients were recruited as part of the Histo-MRI clinical study [5], where 5 patients had lesions and underwent prostatectomy, 6 patients had malignant lesions on biopsy and underwent (radio/cryo) therapy and 11 patients who were screened for prostate cancer but were not diagnosed with PCa (control cohort). All subjects were given Buscopan prior to the scan to reduce rectal gas and bowel motion. 3D GRE images were acquired on a 3T Philips Ingenia using an anterior 4x4 channel receive array and a 4x4 array in the table. Optimised scan parameters [6] included: FOV 420 x 320 x 128 mm, 1 mm isotropic resolution, 5 in-phase echoes, TE1 4.6 ms, ΔTE 6.9 ms, and SENSE factor 3. An optimized QSM pipeline was used to generate susceptibility maps: Total field maps from a non-linear fit of the complex data [7] underwent Laplacian unwrapping [8]. Whole prostate masks were contoured by two expert radiologists using MIM [9] and HOROS [10] software, and were used for background field removal using Variable-radius Sophisticated Harmonic Artifact Reduction for Phase data (VSHARP) with a maximum kernel width of 25 mm [11]. Susceptibility calculation was performed using iterative Tikhonov regularization [12] with the default regularization parameter α=0.05. One lesion per subject was contoured in the prostatectomy and therapy cohorts; and one healthy tissue contour was drawn per subject for the control cohort.

Results and Discussion: The mean lesion susceptibility values were significantly ($t(9)=3.8$, $p=0.004$) higher in the prostatectomy cohort (8.6 ± 4.8 ppb, mean ± SD) compared to the therapy cohort (0.30 ± 2.2 ppb) in this preliminary analysis.

One explanation of the significantly different susceptibility values in the different lesion cohorts is that lesion volumes in the prostatectomy cohort were larger (3736 ± 3403 mm^3) than the therapy cohort (2802 ± 2591 mm^3). Additionally, the lesion contours in the prostatectomy cohort and therapy cohort were drawn by different radiologists. Therefore, inter-reader variability needs to be taken into account: the lesion contours in both cohorts will all be drawn a single expert radiologist. If a difference in the susceptibility values between the different cohorts persists, the underlying reason for it will need further investigation. Co-registration of the MRI susceptibility maps with histological stains may enable further characterisation of the lesions and correlations with histopathological (Gleason) scores.

Conclusions: The preliminary results from this limited number of patients and lesions suggest that QSM may have potential to differentiate between different types of lesions. Future work will involve one radiologist contouring all the lesions to remove any effects of inter-reader variability. Further co-registration with histology may contribute to understanding any susceptibility differences observed between these different lesion types.

Acknowledgements: This work is funded by Cancer Research UK-EPSRC Multidisciplinary project award (A24348).

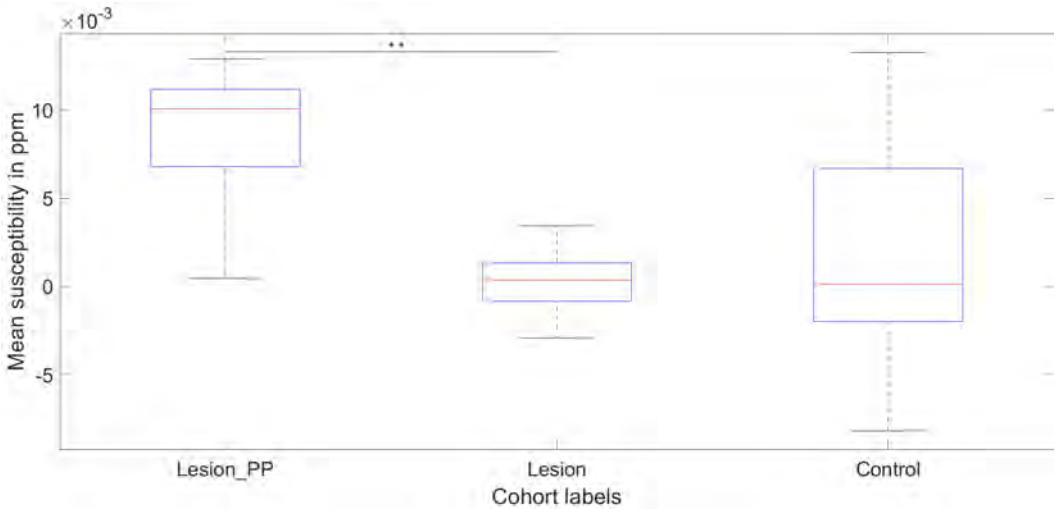

Fig. 1. Box plot of the distribution of lesion susceptibility values in the prostatectomy cohort, the therapy cohort and mean tissue susceptibility values in healthy control regions.

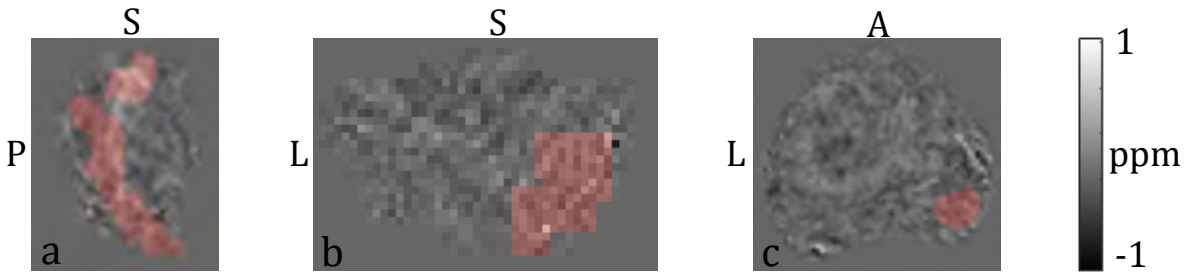

Fig. 2. Selected contour masks (red) overlaid on susceptibility maps. a. Sagittal view of a lesion contour in a subject from the prostatectomy cohort. B. Coronal view of a lesion contour in a subject from the therapy cohort. C. Axial view of a healthy tissue contour in a subject from the control cohort.

References

1. Fan, A.P., et al., *Quantitative oxygenation venography from MRI phase.* Magn Reson Med, 2014. **72**(1): p. 149-59.
2. Kan, H., et al., *Delineation of prostatic calcification using quantitative susceptibility mapping: Spatial accuracy for magnetic resonance-only radiotherapy planning.* J Appl Clin Med Phys, 2021.
3. Straub, S., et al., *Potential of quantitative susceptibility mapping for detection of prostatic calcifications.* J Magn Reson Imaging, 2017. **45**(3): p. 889-898.
4. Fraga, A., et al., *Hypoxia and Prostate Cancer Aggressiveness: A Tale With Many Endings.* Clin Genitourin Cancer, 2015. **13**(4): p. 295-301.
5. Singh, S., et al., *Histo-MRI map study protocol: a prospective cohort study mapping MRI to histology for biomarker validation and prediction of prostate cancer.* BMJ Open, 2022. **12**(4): p. e059847.
6. Muralidharan L, M.M., Clemente J, Caselton L, Kaur S, Brizmohun M, Punwani S, Shmueli K *An Optimized High Resolution Acquisition and Processing Pipeline for QSM in the Prostate*. in *ISMRM & ISMRT Annual meeting* 2023. Toronto, Canada.
7. Liu, T., et al., *Nonlinear formulation of the magnetic field to source relationship for robust quantitative susceptibility mapping.* Magn Reson Med, 2013. **69**(2): p. 467-76.
8. Schweser, F., et al., *Toward online reconstruction of quantitative susceptibility maps: superfast dipole inversion.* Magn Reson Med, 2013. **69**(6): p. 1582-94.
9. *MIM Software Inc.*; Available from: https://www.mimsoftware.com/.
10. *HOROS* Available from: https://horosproject.org/.
11. Schweser, F., et al., *Quantitative imaging of intrinsic magnetic tissue properties using MRI signal phase: an approach to in vivo brain iron metabolism?* Neuroimage, 2011. **54**(4): p. 2789-807.
12. de Rochefort, L., et al., *Quantitative susceptibility map reconstruction from MR phase data using bayesian regularization: validation and application to brain imaging.* Magn Reson Med, 2010. **63**(1): p. 194-206.

P-11

Improving phase-based quantitative conductivity mapping using least squares minimum norm solution

Jierong Luo[a], Oriana Arsenov[a], Karin Shmueli[a]
[a]Department of Medical Physics and Biomedical Engineering, University College London, London, UK.

Introduction: MR-Electric Properties Tomography (MR-EPT) provides a non-invasive technique to reconstruct tissue conductivity and permittivity from the distorted complex RF field (B_1) based on the Helmholtz equation [1]. Assuming local homogeneity of electrical properties, phase-based MR-EPT can solve the truncated Helmholtz equation for tissue conductivity by directly calculating the Laplacian of the transceiver phase (ϕ_0), or, alternatively, by integrating its first derivatives [2]. To overcome the noise-amplifying nature of the Laplacian operation, parabolic fitting of ϕ_0 has proved to be more robust than the finite difference method to reconstruct conductivity in the presence of noise [3]. Matrix inversion is conventionally used to perform the least squares fitting to generate polynomial coefficients within a kernel, from which the voxel-wise conductivity is calculated. Advanced reconstruction methods further incorporate anatomical information, by weighting the fitting with voxel-wise signal magnitudes and refining the kernel based on local tissue segmentations [4]. However, these kernel modifications often result in underdetermined linear systems for voxels within highly noisy regions and voxels near tissue boundaries, where the matrix can become ill-conditioned or singular. In computation, the inversion of underdetermined matrices permits many solutions, and unreliable solutions can be generated for singular matrices when the residuals are small. In the least squares methods, a particular solution can be found for underdetermined linear systems, which minimises both the Euclidean norm and the fit residuals [5]. Therefore, we investigated whether such "minimum norm" solutions can provide more robust conductivity estimates, particularly for voxels where the matrix inversion is ill-conditioned.

Methods: *Numerical brain phantom*: Noise-free complex B_1 was simulated using finite-difference time-domain electromagnetic simulation (XFdtd, USA) of a male human head model at 128 MHz and 1 x 1 x 1 mm^3 resolution [6, 7]. Gaussian noise was added to the real and imaginary signals to vary the phantom SNR. *In vivo brain MRI*: A multi-echo 3D GRE sequence was employed to acquire brain MRI in a healthy volunteer at 3T (Siemens, Germany) with TR = 30 ms, TEs = 4.92, 9.84, 14.76, 19.68, and 24.60 ms, FOV = 256x192x176 mm, with 7/8 partial Fourier and 1 x 1 x 1 mm^3 resolution. ϕ_0 was calculated by extrapolating the phase to TE = 0 after unwrapping with SEGUE [8]. *Quantitative conductivity mapping (QCM)*: We implemented phase-based QCM methods that employ magnitude-weighted Gaussian apodization (Mag) and tissue segmentation kernel modifications (Seg), respectively, and in combination (Mag+Seg) [4]. Segmentations were generated from the magnitude image (TE = 14.76 ms) using SPM [9]. Phantom and in-vivo conductivity maps were reconstructed from ϕ_0 based on Laplacian [3] and surface-integral formulations [2], with 2nd-order polynomial least squares fitting. We computed and compared the conductivities solved by least squares fitting using left-division operation for matrix inversion, and using QR decomposition for finding the least squares minimum norm solution [10]. All image processing was performed in MATLAB (R2022b, MathWorks).

Results and Discussion: In both phantom and in-vivo QCM calculated with matrix inversion, we observed unreliable (NaNs and Infs) and unrealistic reconstructed conductivity values near tissue boundaries and noisy brain regions. In the numerical phantom, the number of ill-conditioned voxels erroneously reconstructed by matrix inversion (Fig. 1A, indicated by white arrows) increased with decreasing SNR and kernel size, and was minimised using minimum norm solution (Fig. 1B, C). Although the number of voxels inaccurately reconstructed by matrix inversion could be reduced by selecting a large kernel size for the polynomial fitting, minimum norm solution yielded conductivity maps (Fig. 2A) with a distribution of smaller regional conductivity variations (i.e. few voxels with inaccurate or unphysical conductivities) than matrix inversion (Fig. 2C). In regions where the linear system is well-conditioned, the difference between the conductivity calculated using the minimum norm solution and matrix inversion is negligible (Fig. 2B).

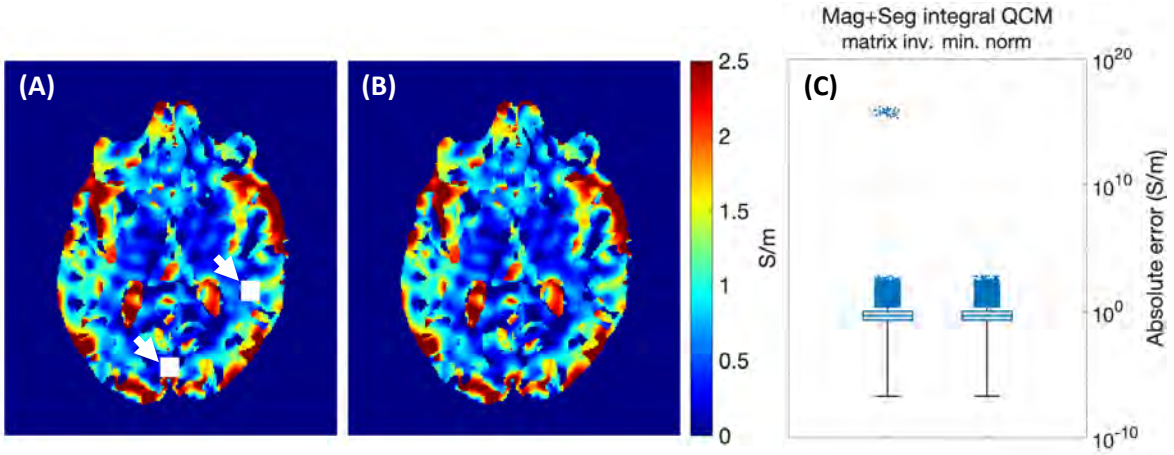

Fig. 1. Conductivity maps of the numerical phantom reconstructed by Mag+Seg integral QCM with a small kernel (11*11*11), using matrix inversion (A) and minimum norm solution (B), and their absolute errors of reconstructed conductivity (C). The effect of erroneously reconstructed voxels is indicated by arrows.

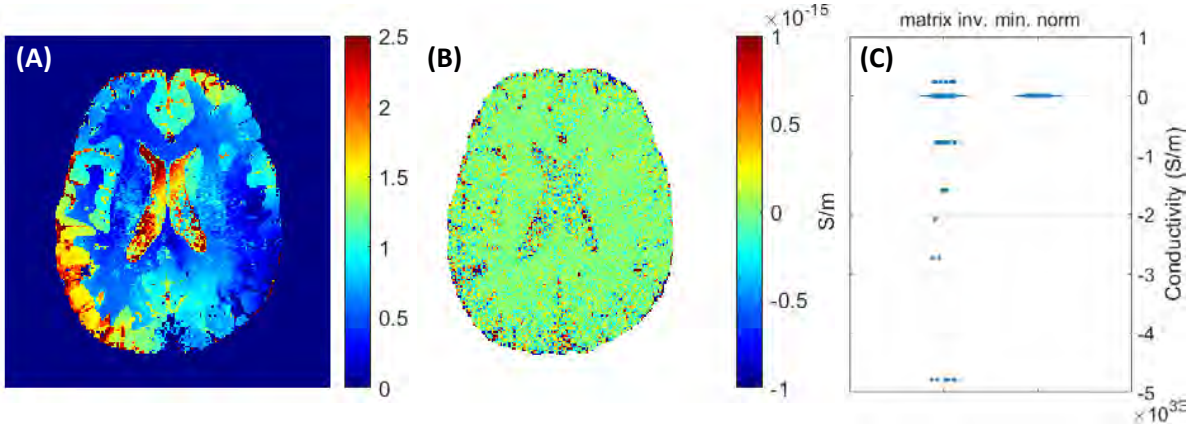

Fig. 2. *In vivo* conductivity reconstructed by Mag+Seg integral QCM with a large kernel (23*23*23) using minimum norm solution (A). Conductivity difference map (B) between minimum norm solution and matrix inversion, green regions indicate the absence of a numerical difference. CSF conductivity distributions using matrix inversion and minimum norm solution (C).

Conclusions: In this work, we demonstrated that the minimum norm solution for polynomial fitting improved conductivity estimation when the linear system was underdetermined, compared with least squares fitting using matrix inversion. In well-conditioned regions, the minimum norm solution preserved the stability of the resulting conductivity values. Therefore, minimum norm least squares fitting is advantageous for phase-based reconstruction of conductivity maps from images with low SNR.

Acknowledgements: The authors are supported by European Research Council Consolidator Grant (DiSCo MRI SFN 770939).

References

[1] U. Katscher, and C. A.T. van den Berg, *NMR Biomed.* **30(8)**, e3729 (2017).
[2] T. Voigt, U. Katscher, and O. Doessel, *MRM*. **66(2)**, 456-466 (2011).
[3] S. K. Lee, S. Bulumulla, and I. Hancu, *IEEE Trans. Med. Imaging* **34(11)**, 2220-2232 (2015).
[4] A. Karsa, and K. Shmueli, *Proc. Ann. Meeting ESMRMB* (2020).
[5] B. Mario, and B. Patrizia, Introduction to Inverse Problems in Imaging (1st ed.), CRC Press, Boca Raton, 1998.
[6] A. Karsa, P. Fuchs, and K. Shmueli, *Proc. Ann. Meeting ISMRM* (2021).
[7] R. Leijsen, et al. *J. Imaging* **5(2)**, 25 (2019).
[8] A. Karsa, and K. Shmueli. *IEEE Trans. Med. Imaging* **38(6)**, 1347-1357 (2018).
[9] J. Ashburner, *et al*. SPM12 Manual, Wellcome Trust Centre for Neuroimaging, London, 2021.
[10] G. Strang, Linear Algebra and Learning from Data, Wellesley-Cambridge Press, Wellesley, 2019.

P-12

Modelling Magnetization Transfer in Segmented ZTE Pulse Sequences

Oliver Pinna[a], Gareth Barker[a], Tobias C Wood[a]

[a] Department of Neuroimaging, King's College London, IoPPN, DeCrespigny Park, Camberwell, SE5 8AF

Introduction: Zero Echo-Time (ZTE) imaging is an attractive alternative to conventional scans as it is comparatively silent, fast, and captures short-lived signals [1]. While the native contrast of ZTE is T1-weighted, preparation pulses can be used to achieve a wide range of contrasts. Here we consider RF-preparation pulses used to increase sensitivity to myelin through semisolid Magnetization Transfer (MT). Deriving algebraic signal equations for such a segmented MT-prepared sequence is tedious and inflexible, and traditional Bloch simulations are cumbersome, as many repetitions are needed before reaching a steady state. In this study, we build upon previous work using homogenized Bloch Equations to provide a fast and flexible sequence simulation method [2] and compare the results to in-vivo measurements.

Theory

As the ZTE readout can be considered a fully spoiled Gradient Echo sequence [1], we neglect the transverse magnetization and consider only the longitudinal magnetization in a system with free (water) and semisolid (myelin) pools, with relative fractions $M_0^f + M_0^s = 1$. The evolution of the magnetization is governed by the differential equations [2, 3, 4, 5, 6]:

$$\frac{d\boldsymbol{M}}{dt} = (\boldsymbol{\Omega} + \boldsymbol{\Lambda})\boldsymbol{M} + \boldsymbol{C} = \boldsymbol{A}\boldsymbol{M} + \boldsymbol{C}$$

$$\text{or } \frac{d\widetilde{\boldsymbol{M}}}{dt} = \widetilde{\boldsymbol{A}}\widetilde{\boldsymbol{M}} \text{ where } \widetilde{\boldsymbol{M}} = \begin{bmatrix}\boldsymbol{M}\\ 1\end{bmatrix}, \widetilde{\boldsymbol{A}} = \begin{bmatrix}\boldsymbol{A} & \boldsymbol{C}\\ \boldsymbol{0} & \end{bmatrix}$$

and $\boldsymbol{M} = \begin{bmatrix}M_z^f\\ M_z^s\end{bmatrix}$, $\boldsymbol{\Omega_{RO}} = \begin{bmatrix}\sin\alpha_{RO} & 0\\ 0 & exp(-W\tau_{RO})\end{bmatrix}$, $\boldsymbol{\Omega_{MT}} = \begin{bmatrix}1 & 0\\ 0 & exp(-W\tau_{MT})\end{bmatrix}$, $\boldsymbol{\Lambda} = \begin{bmatrix}-R_1^f - k_f & k_s\\ k_f & -R_1^s - k_s\end{bmatrix}$ and $\boldsymbol{C} = \begin{bmatrix}R_1^f M_0^f\\ R_1^s M_0^s\end{bmatrix}$. Due to kinetic equilibrium, $k_f M_0^f = k_s M_0^s = k$

Over a period Δt, where $\widetilde{\boldsymbol{A}}$ is constant, the evolution of $\widetilde{\boldsymbol{M}}$ is given by $\widetilde{\boldsymbol{M}}(t + \Delta t) =$ $\exp(\widetilde{\boldsymbol{A}}(t)\Delta t)\widetilde{\boldsymbol{M}}(t)$. The steady state of a sequence is then given by:

$$\widetilde{\mathbf{M}}(t + TR) = \prod_{n=0}^{N-1} \exp(\widetilde{\mathbf{A}}(t + n\Delta t)\Delta t)\widetilde{\mathbf{M}}(t) = \widetilde{\boldsymbol{X}}(t)\widetilde{\mathbf{M}}(t)$$

where $\widetilde{\mathbf{M}}(t)$ is the eigenvector of $\widetilde{\boldsymbol{X}}(t)$ with unit eigenvalue.

Methods: A healthy volunteer was scanned at 3T (GE Premier) with a 48-channel head coil. The sequence parameters used were $TR = 2ms$, $\tau_{MT}/\tau_{RF} = 20ms/16\mu s$, $\alpha_{MT}/\alpha_{RF} = 1800°/1°$ (Gaussian MT pulse at 5kHz), spokes per segment = 768. The scan time was approximately 3 minutes.

Each segment was divided into 16 bins containing 48 spokes and reconstructed with Total Variation regularization along the time dimension [7]. An ROI was drawn in posterior white matter over three slices, and the averaged signal fitted to the above model using non-linear least squares [8].

Results: Figure 1 (left) shows the first and last reconstructed frames. The signal intensity in white matter increases by approximately 5% between these frames. Figure 1 (right) shows the time course in the ROI and the resulting fit from the model. The fitted parameters were: $k = 0.90 \pm 0.01$ s^{-1}, $R_1^f = 0.840 \pm 0.071$ s^{-1}, $R_1^s = 9.97 \pm 0.99$ s^{-1} and $M_0^s = 0.031 \pm 0.001$.

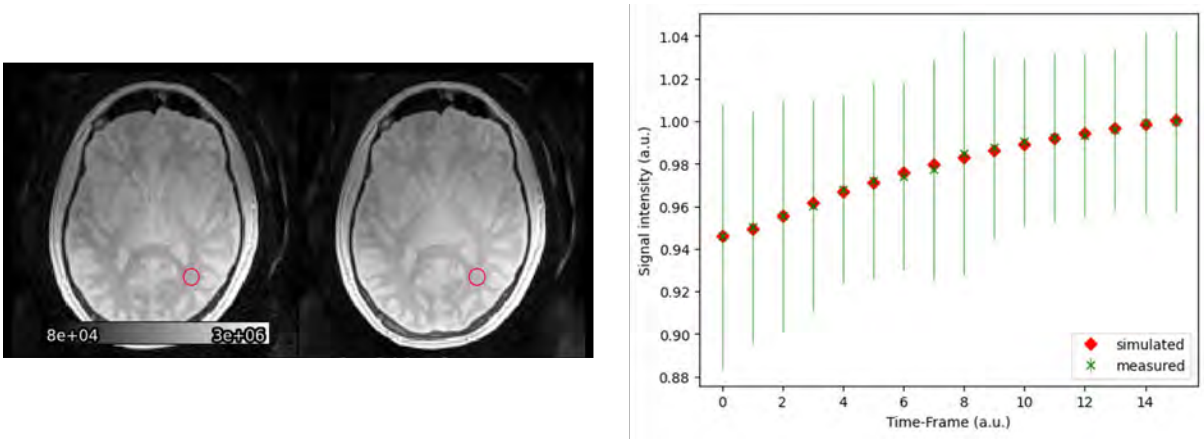

Figure 5 (Left) First and last of 16 frames reconstructed from a single ZTE dataset showing an increase of WM signal intensity. The red circle indicates the ROI. (Right) Normalized white matter ROI signal simulated and measured from the ZTE frames (error bar = ±1std).

Discussion: The Homogenized Bloch Equations framework allowed straightforward modelling of the ZTE sequence with different parameters and was accurate enough to produce a plausible fit to the data. Importantly, we were able to include the saturation effect of the short hard RF pulses used for the ZTE readout, which can affect the bound pool. The tissue parameters found from the fit are the correct order of magnitude but show some discrepancies to literature values. This can be at least partially attributed by the lack of a B1+ map in this initial experiment, which will affect both the effective read-out flip-angle and the saturation of the semi-solid pool by the Gaussian pulse. Future work will investigate optimal sequence settings for extracting accurate quantitative MT parameters.

Conclusions: Homogenized Bloch Equations are an efficient and flexible way to simulate complicated segmented pulse sequences such as MT-prepared ZTE.

References

[1] E. Ljungberg *et al.*, *Prog. Nucl. Magn. Reson. Spectrosc.*, vol. 123, pp. 73–93 (2021).
[2] S. J. Malik *et al*, *Magn. Reson. Med.*, vol. 83, no. 3, pp. 935–949 (2020).
[3] R. M. Henkelman *et al*, *Magn. Reson. Med.*, vol. 29, no. 6, pp. 759–766 (1993).
[4] M. Gloor *et al*, *Magn. Reson. Med.*, vol. 64, no. 1, pp. 149–156 (2010).
[5] A. Ramani *et al*, *Magn. Reson. Imaging*, vol. 20, no. 10, pp. 721–731 (2002).
[6] Y. Wang *et al*, *NeuroImage*, vol. 213, p. 116700 (2020).
[7] T. Wood *et al*, 'spinicist/riesling: v0.11'. Zenodo, May 17, 2023. doi: 10.5281/zenodo.7944190.
[8] P. Virtanen *et al, Nature Methods*, vol. 17, no. 3, pp. 261-272 (2020).

P-13

Streamlining Sequence Parameter Comparison and Protocol Optimisation: Leveraging Version Control and Power BI

Yukai Zou[a,b], Mobeen Ali[a], Chris Everitt[c], Angela Darekar[a,b]

[a]Department of Medical Physics, University Hospital Southampton NHS Foundation Trust
[b]School of Clinical and Experimental Sciences, Faculty of Medicine, University of Southampton
[c]Cross Sectional Imaging Department, Radiology, University Hospital Southampton NHS Foundation Trust

Introduction: Clinical MR physicists are integral to the successful translation of quantitative MR (qMR) biomarkers by focusing on activities such as installing sequences, optimising parameters and establishing consistent, robust and efficient protocols [1]. To effectively manage this workflow, it is crucial that the protocols and sequence parameters adhere to the FAIR principles: Findable, Accessible, Interoperable, and Reusable [2]. Currently, the process of manually retrieving this information via a scanner console is inefficient and time-consuming, which is a challenge within a busy clinical setting, and complicated by the fact that protocols are constantly evolving. An absence of version control for scanner protocols and the failure to adhere to the FAIR principle for data management, contributes to these issues. To overcome these challenges, we propose implementing a version control system and utilizing Power BI to visualise sequence parameters to enable research protocol harmonisation. In this abstract, we present a workflow that addresses these issues within a clinical research environment.

Methods: Neuro research protocols from all the MRI scanners in the Trust were exported as xml files. The files were retrieved from a local workstation and variations across versions were monitored using Git. Each xml file was parsed to generate a spreadsheet in comma-separated values (CSV) format, using R (version 4.2.2) along with xml2 (version 1.3.3) and tidyverse (version 2.0.0) packages. All the files and codes were managed using Bitbucket repository. The spreadsheets were uploaded back to the cloud and imported into Power BI, where data models were established to query differences between the CSV files, upon which interactive visuals were created within Power BI reports for user interaction. For an illustrative summary, see Fig. 1.

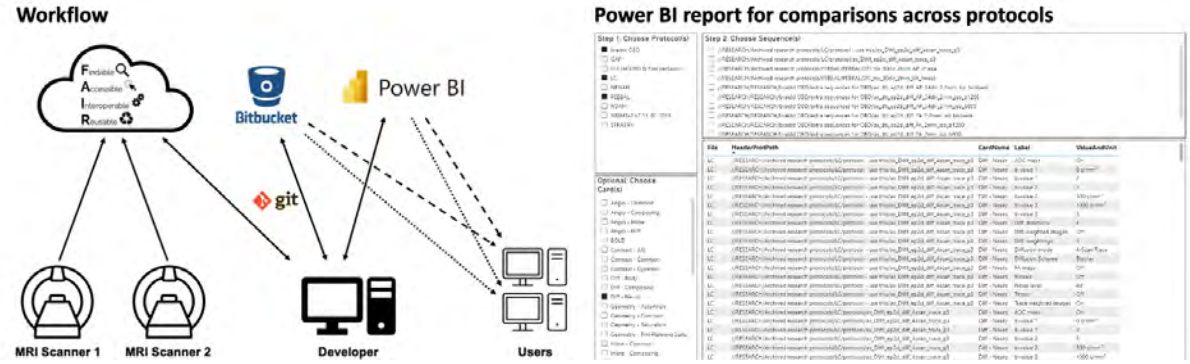

Fig. 1. Illustrative summary of workflow and a Power BI report example.

Results: In total, there were 16 protocols, 226 sequences, and more than 37,000 parameters, and there were 166 parameters per sequence on average (max: 414, min: 88). Protocols were organised into three top-level folder (RESEARCH, USER SMR1, PHYSICS), four second-level folder, and 15 third-level subfolders, with some having fourth- and fifth-level subfolders – a complicated file structure to enable comparisons. The Power BI report facilitates direct and semi-automated comparison of protocols and specific sequence parameters, across multiple projects and scanners. It also supports tracking the evolution of a single protocol with multiple versions, thus aiding protocol optimization. This results in efficiencies relating to protocol set-up, removes the need to use scanner console to compare protocols, and ensures research data acquisition consistency to enable data sharing.

Discussion: The Power BI report enables thorough review of all imaging research projects by facilitating the comparisons of multiple protocols and sequence parameters. Notably, the report visualises the changes made in optimising sequence parameters, which assists our understanding of how these parameters influence the

quantitative values derived from imaging data, and such understanding is a crucial step in translation of qMR biomarkers. The outputs from this workflow also allow comparison of our protocols with community consensus initiatives that focus on different organs and/or disease areas, such as the UKRIN-MAPS multi-parametric renal MRI protocol [1]. We can use the Power BI report to monitor and ensure, going forwards, that research protocols are consistent across projects to allow pooling of data (if appropriate). Lastly, the workflow holds great promise for clinical protocol management in the future. The Power BI report is securely managed within a clinical environment, as access permissions are only granted to relevant personnel.

Conclusions: By integrating FAIR principles, version control and data visualisation, our workflow has significantly improved protocol management, enabled more robust and efficient sequence parameter optimisation and improved data acquisition quality and consistency. The outputs present clear benefits for planning and delivering research in a busy clinical environment, by enabling efficient utilisation of time at the scanner console, thus maximising the use of valuable clinical resources for patient care.

Acknowledgements: We thank the Business Intelligence Team at the University Hospital Southampton NHS Foundation Trust, for their support in granting a pro-license for Power BI and providing us with guidance on information governance.

References

[1] P. L. Hubbard Cristinacce, J. E. Markus, S. Punwani, et al. *Magn. Reason. Med.,* 1- 7 (2023).
[2] M. Wilkinson, M. Dumontier, I. Aalbersberg, et al. *Sci. Data* **3**, 160018 (2016).

P-14

Machine learning based characterisation of glioma shows best performance with post-contrast T1 and diffusion imaging

Gabriel Oliveira-Stahl[a], Marianna Inglese[b,c], Steffi Thust[d,e,f,g], Matthew Grech-Sollars[h, i]

[a] Institute of Neurology, University College London, UK
[b] Department of Biomedicine and Prevention, University of Rome Tor Vergata, Rome, Italy
[c] Department of Surgery and Cancer, Imperial College London, London, UK
[d] Precision Imaging Beacon, Medical School, University of Nottingham, UK
[e] Sir Peter Mansfield Imaging Centre, School of Physics and Astronomy, University of Nottingham, UK
[f] Radiology Department, Queen's Medical Centre, Nottingham University Hospitals NHS Trust
[g] Department of Brain Rehabilitation and Repair, Institute of Neurology, University College London, UK
[h] Lysholm Department of Neuroradiology, National Hospital for Neurology and Neurosurgery, University College London Hospitals NHS Foundation Trust, London, UK
[i] Department of Computer Science, University College London, UK

Introduction: Gliomas are the most common type of malignant brain tumours. Tumour grading and genotyping is essential for guiding treatment and to predict prognosis. Accurate glioma classification relies on tissue diagnosis, which has associated surgical risks, takes time and is not feasible in all patients. XGBoost is one of many machine learning algorithms currently available to perform classification tasks from MR images, potentially enabeling non-invasive glioma characterisation. Choosing the optimal MR modality and best region of interest for feature extraction to maximize model performance remains an empirical question. A recently published dataset [1] contains glioma segmentations for structural and advanced MR acquisitions (Diffusion, SWI, ASL), presenting an opportunity for a systematic search of ideal model inputs. Our aim was to assess which tumour regions and which imaging modalities provided the best accuracy for untreated glioma characterisation.

Methods: The cleaned dataset comprised of 493 glioma patients, of which 56 (11%) were diagnosed with WHO grade 2, 43 (9%) with WHO grade 3, and 394 (80%) with WHO grade 4. The IDH mutation was present in 103 patients (21%). The dataset was divided into 80% for training, and 10% for each validation and testing, while stratifying the groups along the dimensions 1) IDH status, and 2) WHO Grade. A pyRadiomics based pipeline was set up on a high-performance computing cluster to extract 18 first-order features from 10 structural and advanced MR acquisitions (pre-contrast T1, T2, post-contrast T1, FLAIR, SWI, ASL, DWI, ADC, DTI fractional anisotropy and mean diffusivity). XGBoost classifiers were trained on all extracted first-order features, along with basic clinical information (sex and age) to predict WHO grade (grade 2, 3 or 4) and *isocitrate dehydrogenase* (*IDH*) mutation status (wildtype or mutant) with all possible combinations of the 10 modalities as input. First-order features have been separately extracted from the necrotic core, the enhancing region, the non-enhancing region, the whole tumour, and the whole brain, whereby the whole tumour is defined as necrotic core + enhancing region + non-enhancing region.

Results: The XGBoost classifier performed best when features were extracted from the whole tumour (fig. 1, panel a). The modalities that were used for the best performing models are post-contrast T1 (used in 10 / top 10 models), DWI (used in 8 / top 10 models), DTI fractional anisotropy, FLAIR, SWI, and ADC (all used in 6 / top 10 models). The best performing model was trained on first-order features from DTI FA, FLAIR, DWI, post-contrast T1 and DTI MD, and achieved a balanced accuracy of 0.8 for WHO grade prediction and of 0.93 for IDH status prediction (Fig. 1, panel b). The area under the receiver operating characteristic curve (AUC ROC) is 0.98 for differentiating WHO grade 2 gliomas against the other two grades, 0.90 to predict grade 3 tumours and 0.99 for grade 4 gliomas (Fig. 2, panel a). For the classification of the IDH mutation status the AUC ROC is 0.96 (Fig. 2, panel b).

a)

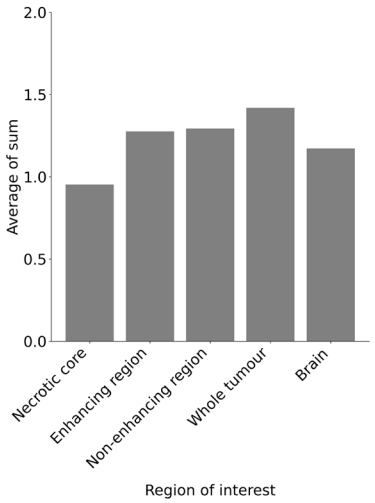

b)

MR acquisition	WHO Grade balanced accuracy	IDH balanced accuracy	sum
DTI eddy FA, FLAIR, DWI, T1 contrast, DTI eddy MD	0.8	0.93	1.73
DTI eddy FA, FLAIR, SWI, DWI, T1 contrast, ASL, T2	0.8	0.91	1.71
DWI, T1 contrast, ASL, T2	0.8	0.88	1.67
FLAIR, SWI, T1 contrast, ASL	0.87	0.8	1.67
ADC, DTI eddy FA, DWI, T1 contrast	0.8	0.86	1.66
ADC, DTI eddy FA, FLAIR, SWI, DWI, T1 contrast	0.8	0.86	1.66
ADC, FLAIR, DWI, T1 contrast, DTI eddy MD, T1	0.8	0.86	1.66
ADC, DTI eddy FA, FLAIR, SWI, DWI, T1 contrast, ASL, T2	0.8	0.86	1.66
ADC, DTI eddy FA, SWI, T1 contrast	0.73	0.93	1.66
ADC, DTI eddy FA, T1 contrast, ASL	0.73	0.93	1.66

Fig. 6. Performance of XGBoost classifier measured in balanced accuracy depends heavily on the brain region chosen for feature extraction (see bar plot) as well as on MR acquisition input (see table). **a)** Comparison of average model performance across all models for different regions of interest during feature extraction. Perfect balanced accuracy for two targets (WHO and IDH) would attain an average of sum = 2. **b)** Top 10 best performing models alongside their MR acquisition input. Features extracted from whole tumour.

a)

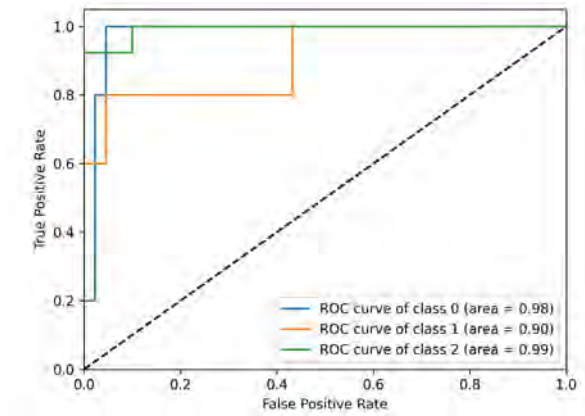

b)

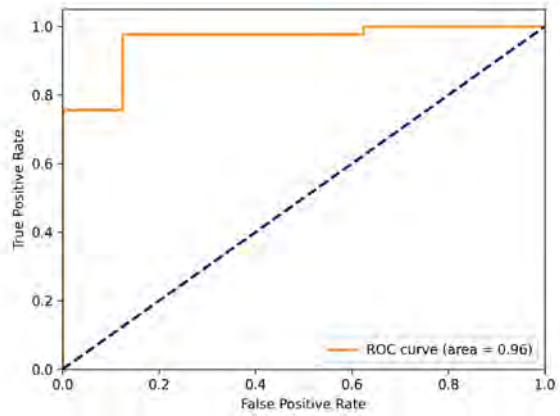

Fig. 7. Receiver operating characteristic curve for best performing model. **a)** ROC for WHO grade prediction. As there are three classes, the evaluation requires three "1 vs. all" ROC curves. Class 0 corresponds to WHO grade 2, class 1 to WHO grade 3, and class 2 to WHO grade 4. **b)** ROC for IDH mutation status prediction.

Discussion: Our study demonstrates how the XGBoost algorithm can effectively predict the WHO grade and IDH mutation status in gliomas using first-order features extracted from MR images. The most informative data appeared to come from post-contrast T1 and diffusion imaging, with features extracted from the whole tumour yielding the highest accuracy. The significant number of models that were trained, however, comes with the risk of overfitting the model on the validation set. Also, while our validation scores are promising, further research should investigate how these models perform on completely unseen data. Additionally, future studies might want to explore how accuracy can be improved by the incorporation of more clinical and genetic data into the model.

Conclusions: Our study suggests that XGBoost can provide meaningful insights for glioma characterisation, especially when trained on post-contrast T1 and diffusion imaging from the whole tumour. However, future work is required to assess the model's performance on unseen data.

References

[1] E. Calabrese *et al.*, 'The University of California San Francisco Preoperative Diffuse Glioma MRI (UCSF-PDGM)'. The Cancer Imaging Archive, 2022. doi: 10.7937/TCIA.BDGF-8V37.

P-15

Impact of diffusion-orientation and phase encoding on EPI image distortion and ADC bias

Prashant Nair[a], Rosie Goodburn[a] , Bastien Lecoeur[a], Uwe Oelfke[a], Andreas Wetscherek[a]

[a]Institute of Cancer Research, 15 Cotswold Rd, Sutton, London

Introduction: The apparent diffusion coefficient (ADC) is a potential quantitative biomarker for assessing response to radiotherapy and for aiding online treatment planning. Diffusion-weighted (DW) imaging acquired with an echo-planar imaging (EPI) readout suffers from geometric distortion related to field inhomogeneity and eddy currents, limiting its utility for radiotherapy treatment planning. The purpose of this work is to investigate the influence of the EPI phase encode direction and diffusion encoding directions on the geometric distortion and ADC accuracy (bias).

Methods: We scanned a diffusion phantom [1] (Qalibre MD Inc., Boulder, CO) filled with ice-water with an ExamCard based on the DW-EPI prostate consensus protocol [2] on a 1.5T Unity MR-Linac (Elekta AB, Stockholm). ADC maps were calculated online using *b*-values 0, 150, 500 s/mm^2.
ROIs were drawn manually, and mean ADCs were calculated using MATLAB R2022a (The MathWorks, Natick, MA) and compared using unpaired t-tests. Geometric distortion was assessed on *b*-500 images by having five repeat measurements of distances between phantom markers A, B and C as shown in figure 1D. ADC biases for the vials with unique ADCs - 1,4,6,8,10 was evaluated. A p-value of 0.05 was considered statistically significant.
The following comparisons were made:

- Phase Encoding: – Anterior Posterior (PE-AP) vs Right Left (PE-RL) with Overplus trace diffusion weighted images (t-DWI). The following experiments were conducted with PE-AP. Gradient Overplus applies gradients simultaneously along different physical axes to minimise TE for optimal SNR.
- Overplus t-DWI vs no-overplus t-DWI
- Overplus t-DWI vs individual overplus orientations
- No Overplus t-DWI vs diffusion encoded along X, Y and Z axes.

For the Overplus scheme, ADC maps had to be calculated manually from the individual diffusion orientation images. The generated ADC maps were compared against the online calculated trace-weighted ADCs to measure any difference/bias in the measurement methods using a paired t-test.
The [pre, post] phantom temperatures (°C) for the measurements were read after letting the thermometer adjust for 1 minute in the ice bath.

Results: The distortion with the PE-AP trace weighted image with gradient overplus was lower than with PE-LR as indicated by the average marker distances (reference – 12.04, 6.0, 10.45 cm) (12.0, **5.9, 10.41** cm) compared to (11.94/**5.82/10.25** cm), where bold font represents statistical significance. The overplus t-DWI had significantly lower distortion along AC (10.41 cm) vs 10.36 cm for non-overplus t-DWI.
Among the scans with overplus, the gradient orientation of 0.66/0.33/-0.66 (X/Y/Z) – OvpDir2, had the lowest geometric distortion (figure 1A) measured by the relative errors to the reference values of the distances for the three markers. When no overplus was used, the lowest distortion was seen when only the Z gradient was used (figure 1B). Comparing the best gradient orientations from the overplus and non-overplus schemes, there was no significant difference between the BC and the AC distances. However, encoding only along Z, the AB distances were not significantly different from the reference while with overplus 0.66/0.33/-0.66 (X/Y/Z), this distance was significantly higher than the reference (figure 1C).
With the Overplus scheme, the ADC bias is lower with the OvpDir2 - 0.66/0.33/-0.66 (X/Y/Z) gradient orientation (figure 2A). This is in terms of the overall ADC deviation from the reference values of each vial. Similarly, without overplus, single diffusion encoding along the Z axis has the least ADC bias (figure 2B).
The measured vs manually calculated ADC for the overplus trace weighted images were not significantly different ($p = 0.06$).

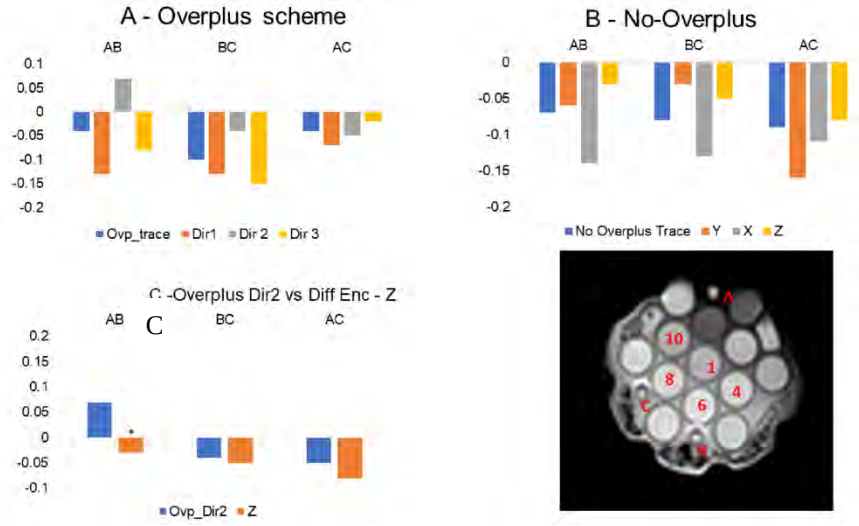

Fig. 1. Geometric distortion measures from the various protocol configurations: Geometric distortion (cm)for the overplus and no-overplus schemes measured as AB, BC and AC distances

Discussion: For use of DW MRI for radiotherapy treatment adaptation in MR-guided radiotherapy, not only accurate ADC measurements, but also geometric accuracy is required. The geometric distortion was reduced with single diffusion encoding both with and without the overplus schemes compared to the respective trace weighted images, which is in line with the results of Kooreman et al. [2].

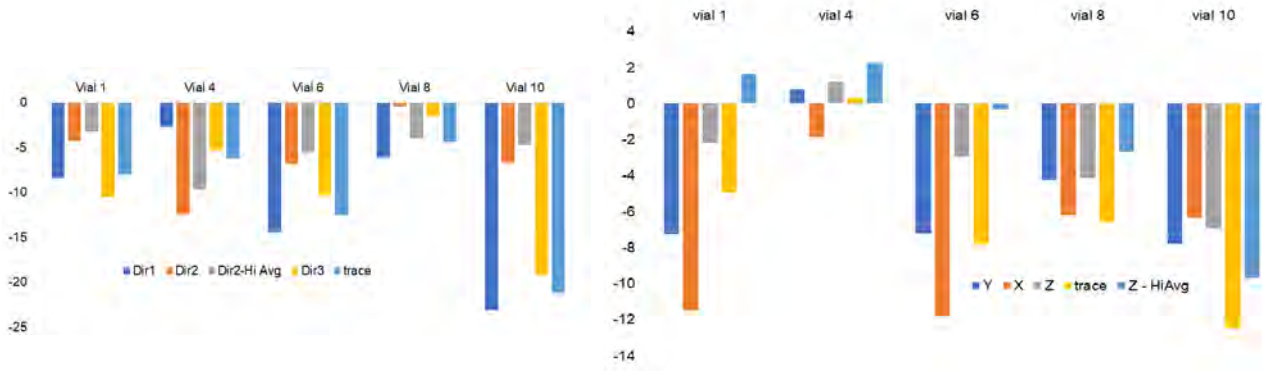

Fig. 2. ADC bias (%) from the various protocol configurations

Similarly, ADC biases were lower with the same diffusion encoding orientations in which the GDs were lowest.

Conclusion: In anatomies where isotropic diffusion could be assumed, scanning with diffusion-encoding only along the Z gradient axis could yield more accurate ADCs with lower geometric distortion at the cost of reduced SNR due to increased echo and diffusion times at the same b-value.

Acknowledgements: Joan Chick, Royal Marsden Sutton, London for discussions and David Higgins, Philips UK for sharing the Philips development environment

References

[1] K. E. Keenan et al. Proc Intl Soc Mag Reson Med 2017;25:3922
[2] E.S Kooreman, P. J VanHoudt et al, Radiother Oncol 2020 Vol. 153 Pages 106-113

P-16

Hippocampal subfield segmentation of super-resolved (resolution-enhanced) diffusion MRI validated with high-resolution T1-weighted imaging

Bastien BRUN[a,b], Prince Nwaubani[c], Matteo Figini[d], Bradley Karat[e], Daniel C Alexander[d], Alessandro Colasanti[c], Mara Cercignani[b]

[a]Polytech Marseille Department of Biomedical Engineering, Aix-Marseille University, Marseille, France
[b]Cardiff University Brain Research Imaging Center, Cardiff University, Cardiff, United Kingdom
[c]Brighton and Sussex Medical School, University of Sussex, Brighton, United Kingdom
[d]Centre for Medical image Computing and Department of Computer Science, University College London, London, United Kingdom
[e]Schulich School of Medicine and Dentistry, University of Western Ontario, London, Canada

Introduction: The hippocampus, an anatomically complex region within the medial temporal lobe, plays a crucial role in cognitive, affective, and behavioral regulation. However, assessment of the hippocampus and its subfields using non-invasive techniques such as MRI is difficult due to its size and complex shape. Image artifacts and limited spatial resolution lead to significant partial volume effects, impacting accurate characterization. Additionally, geometric distortions in diffusion MRI (dMRI) hinder precise co-registration with structural MRI, affecting the extraction of subfield-specific diffusion indices. While high-resolution acquisition protocols have been proposed [1], time constraints often restrict brain coverage and b-value. To overcome these challenges, our study took a different approach to achieve high-resolution dMRI. We employed Image Quality Transfer (IQT) [2], a computational technique that utilizes machine learning to learn the mapping from lower to higher quality data and enhance the spatial resolution of dMRI. The aim of the study was to investigate whether this approach followed by automated hippocampal subfields segmentation can produce a reliable segmentation, matching diffusion parametric maps.

Methods: For this proof-of-principle study, we selected 15 datasets from the WU-Minn HCP Data section, Q3 release [3] of the Human Connectome Project (https://www.humanconnectome.org). The 3 shell-diffusion weighted images included 18 b=0, and 270 diffusion weighted images split into 3 sets of 90 directions, with b-values of 1000, 2000, and 3000 s mm^{-2} respectively. The original resolution was 1.25 mm isotropic [4]. To increase the resolution of the raw dMRI, we fit the mean apparent propagator (MAP) MRI model [5] to the original data, and then used IQT to enhance the resolution of MAP coefficient maps to 0.625 mm isotropic. Those coefficient maps were then used to produce synthetic diffusion weighted images. Directionally averaged images were then obtained for b=1000 s mm^{-2}. The corresponding T1-weighted scan – which is used as standard for automatic subfield segmentation - was also downloaded (resolution= 0.7 mm isotropic) and co-registered to the mean b=1000 images. The *HippUnfold* algorithm [6] was applied to either image modality to segment the hippocampus. *HippUnfold* segments the following parts: subiculum, 4 portions of the cornus ammonis (CA1, CA2, CA3, CA4), stratum radiatum lacunosum-moleculare (SRLM), and dentate gyrus. T1-weighted scans were segmented using the default settings for this modality. The diffusion-weighted data were segmented 3 times using different nnU-Net models, namely the 'T2-weighted', 'Hippb500', and 'NeonateT1w' models. The difference between these models is primarily in the training data used.
The results were first visually assessed and rated. Next, we used the Dice index to establish the degree of overlap between the T1-segmentation and the 3 dMRI segmentations for the whole hippocampus. The model that maximised the overlap was chosen on a participant-basis and further analyses were performed on the output of that model. Next, we compared the whole hippocampus and subfield volumes between T1-weighted and the best dMRI segmentation. The metrics used were: the mixed-2-way average measurement intra-class correlation coefficient (ICC), the coefficient of variation (CV), and the Pearson's correlation coefficient. Bland-Altman plots were also used to investigate potential biases.

Results: Upon visual inspection, it was observed that using T1-weighted anatomical images yielded satisfactory segmentation results, although there were instances of slight overestimation in the volume of the subiculum. The segmentation results for the b=1000 dMRI were variable, depending on participant and model. Overall, the 'NeonateT1w' model (chosen for 9/15 participants) and 'Hippb500' model (chosen for 6/15 participants) outperformed the 'T2-weighted' model. The average Dice index was 0.88 for the left hippocampus and 0.89 for

the right hippocampus. The intra-class correlation coefficient (ICC) for the whole hippocampal volume was 0.95 and 0.85 for the left and right hemispheres, respectively, with coefficient of variation (CV) values of 5.6% and 3.5%. Bland-Altman plots indicated that the dMRI tended to slightly overestimate the whole hippocampal volume (Fig 1). When comparing the volumes of each subfield, the agreement between modalities was excellent for CA4 (ICC>0.9), very good for the subiculum, dentate gyrus, and SRLM (ICC>0.8), while the lowest ICC was found for CA2 (ICC=0.11). Figure 1 displays a randomly selected segmented left hippocampus using both modalities, along with the Bland-Altman plot for the whole hippocampus.

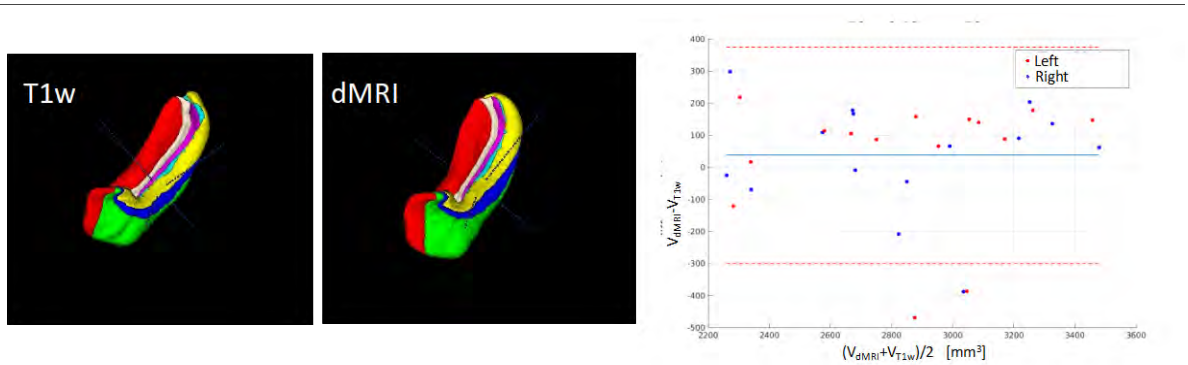

Fig. 1. Segmentation comparison. Subfield segmentation of T1-weighted images (left) and dMRI (centre). Bland-Altman plot for the whole hippocampal volume (right)

Discussion: Our study demonstrates the feasibility of enhancing dMRI resolution through machine learning techniques to achieve accurate segmentation of the hippocampus using *HippUnfold*. It is important to carefully evaluate and select the most suitable model when applying *HippUnfold* to dMRI data. Excellent agreement between T1-weighted and dMRI segmentation can be achieved for the entire hippocampus and the larger subfields. Currently, we are further investigating the implications of these two segmentations on quantifying subfield-specific diffusion indices. Additionally, we are expanding our analysis to include data acquired from patients with multiple sclerosis on a clinical scanner, exploring the potential clinical applications.

Conclusions: Our preliminary results on the feasibility of segmenting hippocampal subfields from super-resolved dMRI are encouraging but further analyses of quantitative data are needed.

References

[1] Su L, Hayes L, Soteriades S, Williams G, Brain SAE, Firbank MJ, Longoni G, Arnold RJ, Rowe JB, O'Brien JT *Journal of Alzheimer's disease*, **61**, 415-424 (2018).

[2] Alexander DC, Zikic D, Ghosh A, Tanno R, Wottschel V, Zhang J, Kaden E, Dyrby TB, Sotiropoulos SN, Zhang H, Criminisi A, *NeuroImage*. **152**, 283-298 (2017).

[3] Van Essen DC, Smith SM, Barch DM, Behrens TE, Yacoub E, Ugurbil K; WU-Minn HCP Consortium, *Neuroimage*. **80**, 62-79 (2013).

[4] Sotiropoulos SN, Moeller S, Jbabdi S, Xu J, Andersson JL, Auerbach EJ, Yacoub E, Feinberg D, Setsompop K, Wald LL, Behrens TE, Ugurbil K, Lenglet C, *Magnetic resonance in medicine*. **70**, 1682-9 (2013).

[5] Özarslan E, Koay CG, Shepherd TM, Komlosh ME, İrfanoğlu MO, Pierpaoli C, Basser PJ, *NeuroImage*. **78**, 16-32 (2013).

[6] DeKraker J, Haast RA, Yousif MD, Karat B, Lau JC, Köhler S, Khan AR, *eLife*. **11**, e77945 (2022).

P-17

Optimisation of T1ρ imaging for detecting cardiac fibrosis

Liene Balode[a], Dana Dawson[a], James Ross [a]

[a]University of Aberdeen, Aberdeen, UK

Introduction: In addition to conventional contrast-obtaining methods that use the spin-lattice (T1) and spin-spin (T2) relaxation mechanisms, there is another contrast-obtaining method that uses spin-lattice relaxation in the rotating frame (T1ρ). T1ρ contrast can be obtained by performing imaging following the application of a spin-lock (SL) pulse. Because of its sensitivity to low-frequency motional processes (Hz-kHz), T1ρ can be used to investigate the macromolecular composition and proton exchange within the tissue [1]. Hence, T1ρ MRI has the potential to detect cardiac fibrosis that is the result of an increase of protein deposition in the myocardial extracellular matrix. Cardiac T1ρ imaging is technically difficult and accurate T1ρ quantification remains challenging in routine clinical practice [2]. Therefore, in this work we have aimed to optimise our T1ρ imaging protocol for detecting cardiac fibrosis at 3T by varying the pulse sequence parameters.

Methods: After informed consent, healthy volunteers were scanned using a 3.0 T MRI scanner (Achieva dStream, Philips, Amsterdam, Netherlands). The imaging sequence starts with a SL pulse (90_x—SL_y—180_y—SL_{-y}—90_{-x}) which is followed by a breath-held single-shot balanced steady-state free precession (bSSFP) image acquisition to acquire images of basal, mid-cavity and apical segments of the left ventricle. SL pulse durations used were linearly spaced from 0 ms to $SL_{max.}$ To optimise our protocol, we varied the following sequence parameters: SL_{max} (20, 30, 40 ms), the number of SL pulses used (4 or 6) and the flip angle (FA) of the bSSFP sequence (between 10^0 and 90^0). The acquired T1ρ maps were analysed using the Philips IntelliSpace Portal software.

Results: It was found that the measured T1ρ did not change significantly when FA was altered from 10^0-90^0 (Figure 1), however a significant improvement in image signal-to-noise ratio (SNR) was observed. There was no significant difference in the measured T1ρ relaxation time of the myocardium when acquisitions used 4 and 6 SL pulses. The acquisitions with different maximum SL pulse durations showed that the measured T1ρ relaxation times depends on the maximum length of the SL pulse used.

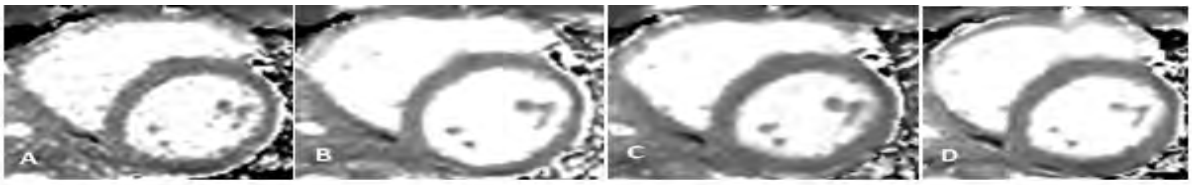

Fig. 1. Quantitative T1ρ maps acquired from a basal slice. The flip FA used for acquired image and corresponding T1ρ relaxation time: a) 10^0 and 43 ms, b) 20^0 and 45 ms, c) 30^0 and 42 ms, d) 90^0 and 44 ms.

Discussion: Although the SNR increased for the T1ρ images with increasing FA, the measured T1ρ relaxation time from the T1ρ maps did not change significantly. It was observed that T1ρ map quality is sufficient for the FA ranging from 20^0-30^0. Increasing the number of SL pulses from 4 to 6 was expected to reduce T1ρ quantification error as more data points were acquired for the exponential decay. However, there was no significant difference in the T1ρ rho relaxation time measured. Using 20 and 30 ms instead of 40 ms for the maximum duration of the SL pulse resulted in reduced measurement of T1ρ which we attribute to insufficient sampling of the relaxation process.

Conclusions: To reduce maximum breath hold durations, 4 SL pulses could be used, which would be a more suitable option for patients with cardiovascular disease who are unable to perform long breath holds. The maximum SL pulse duration should be at least 40 ms SL pulse should be used to ensure sufficient sampling of the myocardium T1ρ relaxation. The optimum FA for the bSSFP acquisition sequence should range from 20^0-30^0 to ensure sufficient image SNR without the specific absorption rate considerations imposed by the use of larger flip angles.

References

[1] Wang P, Block J, Gore JC. Chemical exchange in knee cartilage assessed by R1ρ (1/T1ρ) dispersion at 3T. Magn Reson Imaging. 2015;33(1):38-42.
[2] Bustin A, Witschey WRT, van Heeswijk RB, Cochet H, Stuber M. Magnetic resonance myocardial T1ρ mapping: Technical overview, challenges, emerging developments, and clinical applications. J Cardiovasc Magn Reson. 2023;25(1):34.

P-18

Magnetic Resonance Imaging as a Therapeutic Device: Utilization of Iron Oxide Nanoparticles (SPIONs) for Tumor and Cancer Treatment

Sidharth Vinod[a], Silpamol Jaimon[b], Shazna Ashraf K K[c] Amisha Sabu[d]

[a,c]University of Aberdeen, Kings College, Aberdeen, AB24 3FX
[b,d]Swansea University, Singleton Park, Sketty, Swansea SA2 8PP

Introduction: The application of Magnetic Resonance Imaging (MRI) as a therapeutic device has gained significant attention in recent years due to its potential in targeted tumor therapy. This research paper aims to explore the utilization of Superparamagnetic Iron Oxide Nanoparticles (SPIONs) integrated with MRI technology for the treatment of tumors and cancer. By combining the unique properties of SPIONs with the imaging capabilities of MRI, a powerful platform for precise tumor imaging, targeted drug delivery, and localized hyperthermia treatment is created.

Methods: In order to investigate the potential of SPIONs in tumor therapy, a comprehensive overview of their principles, including synthesis methods and physical and chemical properties, is provided. The paper delves into the functionalization of SPIONs with specific targeting moieties, such as antibodies or peptides, to enhance their tumor-specific accumulation. Furthermore, the role of MRI in SPION-based tumor therapy is elucidated, highlighting its ability to non-invasively image SPIONs, monitor their distribution in real-time, and assess treatment response. Advanced MRI techniques, such as Magnetic Particle Imaging (MPI), are also explored as a means to enhance the detection and quantification of SPIONs within tumors.

Results: The unique magnetic properties of SPIONs open up a range of therapeutic strategies for cancer treatment. Hyperthermia treatment, achieved through the application of an alternating magnetic field, allows for localized heating of tumor tissues, leading to tumor cell death. Moreover, SPIONs can serve as carriers for chemotherapeutic agents, genes, or photodynamic therapy agents, enabling targeted drug delivery and controlled release. These versatile capabilities of SPIONs, combined with the imaging capabilities of MRI, offer great potential for improved tumor therapy outcomes.

Discussion: The integration of SPIONs with MRI technology presents exciting possibilities for precise tumor imaging, targeted drug delivery, and localized hyperthermia treatment. However, there are several challenges that need to be addressed to facilitate the translation of SPION-based MRI therapy into clinical practice. Optimizing the synthesis of SPIONs to enhance biocompatibility and targeting efficiency is crucial. Additionally, further understanding of the underlying mechanisms of SPION-mediated therapy is needed, along with rigorous preclinical and clinical studies to ensure safety and efficacy.

Conclusion: This research paper highlights the promising role of SPIONs in MRI-based tumor therapy, offering a comprehensive analysis of their synthesis, functionalization, and integration with MRI technology. The combination of SPIONs and MRI enables real-time monitoring of SPION distribution, assessment of treatment response, and targeted drug delivery. Continued advancements in SPION synthesis, functionalization techniques, and clinical studies are essential to unlock the full potential of SPION-based MRI therapy, ultimately improving the outcomes of tumor and cancer treatment.

P-19

Numerical Modelling of MRI-related RF Power Deposition of Orthopaedic Implants - How Detailed do the Implant Models have to be?

Michael Taylor[a], R Stephen Nicholas[b, c]

[a]University of Aberdeen, King's College, Aberdeen AB24 3FX Scotland, UK
[b]University of Dundee, Nethergate, Dundee DD1 4HN Scotland, UK
[c]Ninewells Hospital and Medical School, NHS Tayside, Dundee DD1 9SY Scotland, UK

Introduction: Numerical modelling of the electromagnetic fields in the MR environment using the Finite-Difference time-Domain (FDTD) method has become an accepted way to assess safety in MRI, particularly in relation to Radiofrequency (RF) power deposition around orthopaedic implants. Guo et al [1], highlighted that where multiple orthopaedic implants are present in close proximity (as may be the case in patient who have undergone orthopaedic surgery to fix complex multiple fractures), Specific Absorption Rates (SAR) may be elevated to levels that may be considered unsafe. However, their models were simple, and it is the aim of this present work to examine whether using models that better represent real-world orthopaedic implants will produce different SAR results, specifically focussing on the magnitude and spatial distribution.

Methods: Simulations were set up in Sim4Life (version 7.2.1.11125, Zurich MedTech AG, Switzerland) using the P-EM-FDTD solver. An 8-leg Birdcage coil was set up to produce a uniform B_1 field oscillating at 64 MHz (1.5 T), with a model of the ATSM phantom filled with tissue-equivalent gel placed at the centre. Implant models were based around a DePuy Synthes titanium Locking Compression Plate (LCP) with screws. The plates were modelled to four levels of complexity: basic (modelled as a thick rectangle with similar dimensions), low, medium and high, where plate ends are bevelled and rounded off, screw holes are represented with chamfers and threads (Fig 1). Screws of two types (cortical and cancellous) were modelled as cylinders with conical points, heads, and screw threads for all plate complexities. Plate dimensions were 59×12×3.3 mm; screw dimensions were length 10 mm, thread diameter 3.5 mm (cortical) and 4 mm (cancellous). The plates were simulated individually, placed in the same position in the phantom. All other simulation parameters were kept identical to ensure consistency. The simulated E-fields were converted into 0.1g averaged SAR values and these were plotted graphically at various positions around the implants.

Results: It can be clearly seen from Fig. 1 that the SAR distributions vary significantly depending on the complexity of the implant. The basic configuration demonstrates intense hotspots at the corners, which become a more generalised single region in the centre of the plate-end when a realistic design is used.

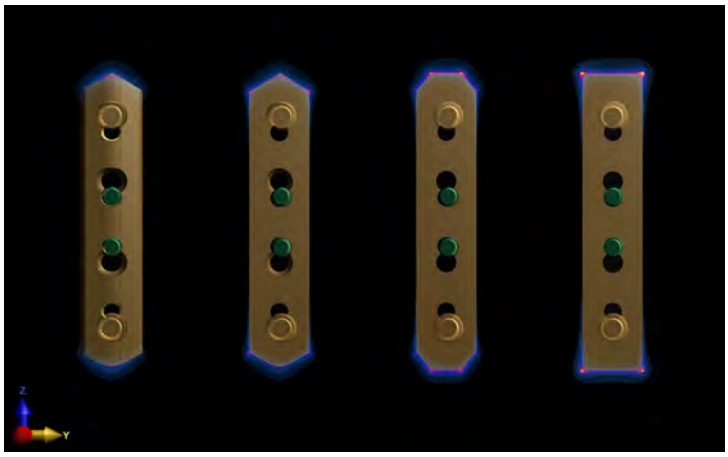

Fig. 1. Models of the LCP plate with differing complexity, with left to right showing high, medium low and basic complexity. Colours in the regions surrounding the implants represent the SAR distribution normalised to the maximum SAR observed in the basic plate.

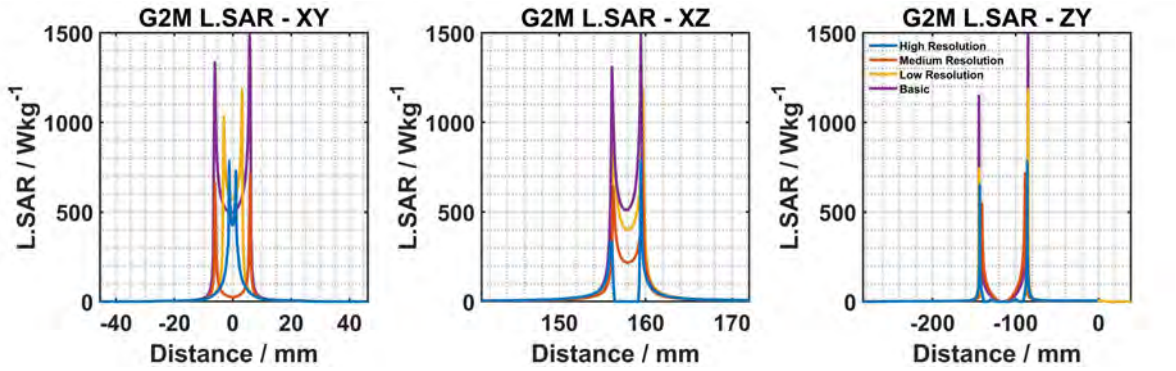

Fig. 2. Graphs showing 0.1 g local SAR at various locations around the implants with varying model complexities. Plots taken along a line in a plane where the SAR was maximal ("Go to Max" or G2M). Left: y-direction in X-Y plane; middle: x direction in X-Z plane and right: z direction in ZY plane. Purple – basic, yellow – low, red - medium, and blue – high.

The graphs in Fig. 2 demonstrate that the SAR levels vary significantly with plate complexity, with the use of a simple plate resulting in a peak local SAR that is 1.9 times higher than that seen in the high complexity plate. Aside from the differences in spatial positions of the maxima, the peak SAR values between the medium and the high complexity plate are similar.

Discussion: This work demonstrates that the complexity of the implant models can have a marked effect on both the distribution and intensity of SAR. Having a model that represents the implant faithfully may seem intuitive, but this requires a fine simulation grid size, long simulation times and higher computing requirements. The implications are that implants whose MRI safety is assessed using these computational methods may be seen as having a higher risk for RF induced heating, with the potential consequence that patients with such implants may not be scanned. It is therefore important that models should accurately represent the implants, although a high level of detail may not be necessary if representative peak SAR values only are required and the spatial distribution is not critical, which may be helpful in situations where limitations on computational power exist.

Conclusions: When performing FDTD simulations to assess the effects of MR-related RF heating around orthopaedic implants, care should be taken to ensure that the model is a good representation of the real-world implants. Using overly simplistic models may lead to incorrect spatial distributions of SAR and elevated SAR values.

Acknowledgements:

References

[1] Guo R, Zheng J, Wang Y, et al. Magn Reson Med. 2019; 82: 1848–1858.

P-20

Universal Excitation Pulses for a Parallel-Transmit Head Coil at 7T

Yiling Hu[a], Belinda Ding[a,b], Shajan Gunamony[a,c], David A. Porter[a], Sydney N. Williams[a]

[a]Imaging Centre of Excellence, University of Glasgow, Glasgow, UK
[b]Siemens Healthcare Ltd., Frimley, UK
[c]MR CoilTech Limited, Glasgow, UK

Introduction: 7T MRI offers improved resolution over 1.5T and 3T MRI with the drawbacks of increased radiofrequency (RF) field inhomogeneity and higher tissue power deposition [1]. Parallel transmission (pTx) addresses these issues by splitting the transmit coil into multiple, independently controlled channels [2]. However, designing subject-specific pTx pulses is time-consuming due to variations in B_0 and B_1^+ maps [3]. Universal pulses (UPs) provide a plug-and-play solution that balances image quality and time efficiency to increase the appeal of pTx 7T MRI for clinical use [3]. This abstract presents the process and preliminary results of designing excitation UPs for an in-house RF head coil introduced earlier this year for the 7T scanner at the Queen Elizabeth University Hospital in Glasgow.

Methods:

Equipment and data: Radiofrequency excitation pulses were designed for a MAGNETOM Terra 7T MRI scanner (Siemens Healthineers AG, Germany) equipped with a custom-built head coil with 8 transmit channels and 64 receive channels (8Tx64Rx) (MR CoilTech Limited, UK). Siemens' pTx pulse design (PPD) toolbox was modified and used for pulse design and simulation in MATLAB (The MathWorks, USA). Universal pulses were generated using transverse B_1 maps previously acquired from 16 healthy subjects. The pulse design process was guided by 5° UPs previously designed for an earlier prototype of the head coil with 8 transmit and 32 receive channels (8Tx32Rx).

RF pulses and sequences: 5°, 15°, and 50° flip angle (FA) excitation pulses were designed to be used in 3D MPRAGE [4] and 3D FLASH [5] sequences. Optimum pulse designs were identified by using Bloch simulations to minimize the normalized root mean squared error (NRMSE) and specific energy dose (SED), using circularly polarized (CP) pulses and 8Tx32Rx UPs as standards.

Algorithms: Three methods of numerical optimization were used, two of which used algorithms from MATLAB's Global Optimization Toolbox: (i) GlobalSearch, a deterministic global minimum solver, and (ii) simulannealbnd, which uses the simulated annealing algorithm [6]. A 100ms RF pulse and combined optimized variables (COVs) were optimized using varying subject dataset sizes. CP pulses and 8Tx32Rx UP's COVs were used as optimizer starting points. The third method, referred to as the "stacked method," used concatenated adjustment data from 14 subject maps and Siemens' bespoke PPD toolbox optimization, based on the process described by Aigner et al. [7].

Validation: Phantom tests were performed using 3D FLASH and a head-and-shoulders phantom with similar conductivity and permittivity to that of brain tissue for validation. Preliminary results were obtained from three healthy subjects using 3D MPRAGE and 3D FLASH, comparing CP, 8Tx32Rx UP, 8Tx64Rx UP, and a subject-specific pulse. The healthy-subject scans in vivo were performed using a second prototype of the 8Tx64Rx head coil.

Results: GlobalSearch and simulannealbnd methods provided poor results, with high SED and inhomogeneous excitation patterns despite low NRMSE. The stacked method yielded low NRMSE and SED with good image uniformity and was applied in-vivo. Fig 1 compares the performance of CP, 8Tx32Rx UP, 8Tx64Rx UP, and tailored design for 5° FA excitation pulses on the 14 subject maps used to design the pulse. The 8Tx64Rx UP NRMSE (~25%) outperforms both CP (~40%) and 8Tx32Rx UP (~30%), and its SED (0.0075) is also much lower than that of 8Tx32Rx UP (0.0180). Phantom testing and the study in vivo of the 5° pulse (Fig 2) validate these simulation results, with low NRMSE of 25% and SED of 0.0075. The 15° and 50° FA UPs also perform better than CP in NRMSE but have poor excitation-pattern homogeneity in simulation and in vivo.

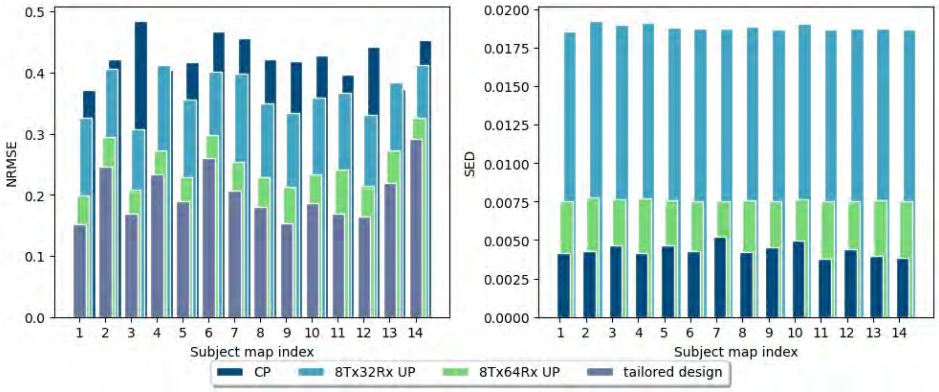

Fig. 1. Simulated NRMSE and SED for a 5° excitation pulse across 14 subjects. The 8Tx64Rx UP NRMSE outperforms both CP and 8Tx32Rx UP but not a subject-specific tailored pulse. 8Tx64Rx UP has higher SED than CP but performs better than 8Tx32Rx UP.

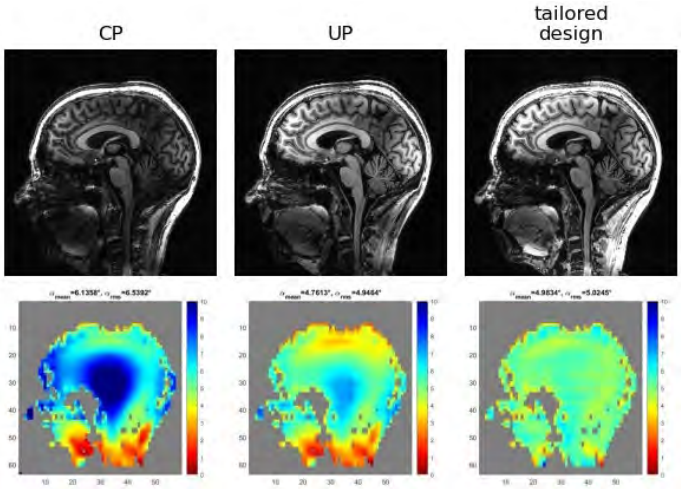

Fig. 2. Images acquired in vivo (top row) and simulation results (bottom row) for RF excitation pulses using CP, 8Tx64Rx UP, and a tailored (subject-specific) design. The UP has a more homogeneous excitation and image as well as better contrast compared to CP, but the subject-specific pulse has the most homogeneous excitation.

Discussion: The limited success of the MATLAB optimization algorithms was likely due to time constraints and computational limits. Preliminary results using the stacked method showed effectiveness in small flip angles. Further development and testing in a wider subject group are needed to confirm its effectiveness and improve upon larger FA pulse design. A similar method can also be applied to designing inversion UPs for a more comprehensive solution.

Conclusions: Initial results from simulations and scans in vivo suggest that low-flip angle excitation UPs designed with the stacked method can achieve sufficient uniformity at 7T with limited image-quality effects from RF field inhomogeneity and SAR values that allow practical application in vivo.

Acknowledgements: We are grateful to NeuroSpin Paris for their 3D FLASH sequence, University of Erlangen for their 3D MPRAGE sequence, and Siemens for the PPD toolbox and technical support.

References

[1] Williams et al. (2023). *Physics in Medicine and Biology*, **68**(2).
[2] Padormo et al. (2016). *NMR in Biomedicine*, **29**(9), 1145–1161.
[3] Gras et al. (2017). *Magnetic Resonance in Medicine*, **77**(2), 635–643.
[4] Mugler et al. (1990). *Magnetic Resonance in Medicine*, **15**(1), 152–157.
[5] Matthaei et al. (1986). *Magnetic Resonance Imaging*, **4**(5), 381–386.
[6] Global Optimization Toolbox version: 4.8.1 (R2023a): The MathWorks Inc. https://www.mathworks.com.
[7] Aigner et al. (2022). *Magnetic Resonance in Medicine*, **87**(1), 70–84.

P-21

Investigating the impact of complementary microstructural phenomena on diffusion MRI measurements

Zhiyu Zheng[a], Karla Miller[a], Benjamin Tendler[a], Michiel Cottaar[a]

[a]Wellcome Centre for Integrative Neuroimaging, University of Oxford, Oxford, United Kingdom

Introduction: Diffusion-weighted MRI (dw-MRI) simulations investigate how microstructural geometry impacts the measured dw-MRI signal. There are several complementary microstructural phenomena that also impact MRI measurements, including water exchange, magnetisation transfer (MT), and off-resonance effects. If these phenomena cause a substantial signal deviation, it could bias the dw-MRI measures, as these phenomena's signal contributions are often ignored and incorrectly attributed to diffusion by dw-MRI models [1,2]. To address this, a novel Monte-Carlo simulator integrating both diffusion and all the aforementioned phenomena was developed [3]. Here we use this simulator to estimate the dw-MRI signal deviation induced by MT and membrane permeability.

Methods: Two analytical descriptions of the dw-MRI signal evolution were chosen as references for comparison with simulation results: Mitra's approximation at short diffusion times [1] and the diffraction-like signal pattern at high q-values [2].

The intrinsic diffusivity (D) was set to 2μm^2/ms for all simulations to mimic tissue fluid. To simulate MT, Monte-Carlo spins were divided into two exchanging groups: the bound pool and the free pool. The bound pool is localised at user-generated obstructions and has a very short relaxation time, while the free pool occupies the remaining space. When a spin collides with an obstruction it has a certain probability of transferring to the bound pool. This probability is determined by the average time being bounded and the ratio between surface spin density on the obstruction and the volume density in the free pool, which are adjustable parameters in the simulator. For ease of interpretability, we quantify the size of the MT effect by its effect on the T_2 (i.e., effective T_2). To simulate permeability, the simulator allows spins to pass through an obstruction with a user-defined probability.

For the diffraction pattern simulation, 10^5 spins were simulated between regularly spaced parallel walls 1μm apart with an instantaneous diffusion-weighted gradient applied orthogonally to the wall. Simulations were performed with varying MT or permeability, with the diffusion time (t) set to 40ms for MT and 10ms for permeability to ensure long diffusion time relative to the wall separation. Signal attenuation at various q-values was obtained and compared to the analytical solution $E(q) = \frac{\sin(\pi q L)}{\pi q L}$.

For Mitra's approximation, 10^6 spins were used to reduce noise generated by random motion and the wall separation was changed to 10μm. The q-value was fixed at 1 rad/μm and the signal attenuation was recorded at various diffusion times. The gap separation and the intrinsic diffusivity (D_0) were then estimated using Mitra's approximation equation $D(t) = D_0\left[1 - \frac{\frac{4S}{V}}{9\sqrt{\pi}}\,(D_0 t)^{\frac{1}{2}}\right] + O(D_0 t)$, where D(t) is the ADC estimated from signal attenuation, S/V is the wall separation's reciprocal.

Results: As shown in Figure 1, realistic MT strength has no observable effect on the diffraction pattern. Permeability reduces the signal amplitude, but does not shift the locations of the extrema. For Mitra's approximation, Figure 2 shows that both MT and permeability cause overestimation of wall spacing.

Discussion: To first order one might expect the relaxation due to MT to affect the signals with and without diffusion weighting equally and, hence, not affect the signal attenuation. However, some spins will by chance interact more with the obstructions. These spins will both experience more restrictions and have a shorter effective T_2 due to MT. This effect is particularly pronounced for the short diffusion time in the Mitra's approximation, where MT causes a reduced signal contribution from spins interacting with the obstructions,

which causes us to overestimate the compartment size. At the longer diffusion times used in the diffraction experiment, this effect is less pronounced, because spins are more thoroughly mixed and have roughly equal probability to interact with obstructions and experience MT.

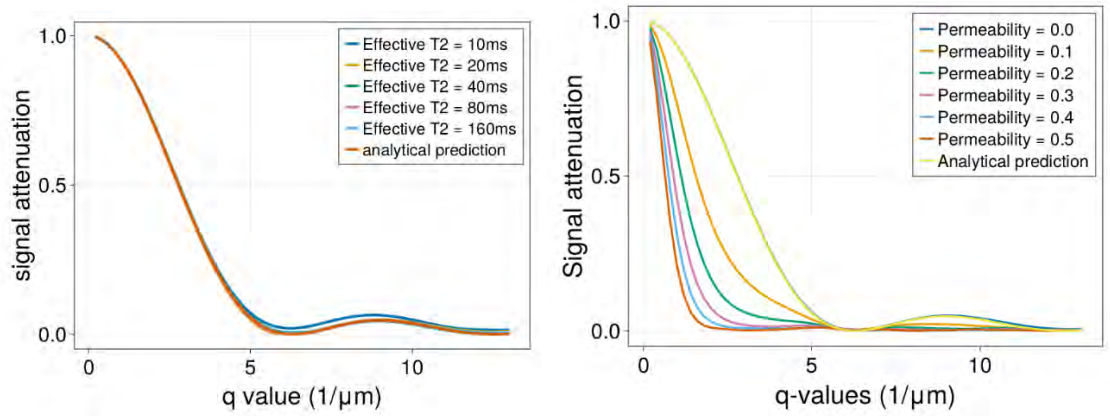

Fig. 1. Changes in diffraction pattern due to magnetisation transfer (MT) (left) and permeability (right), effective T_2 is the T_2 driven purely by MT effects.

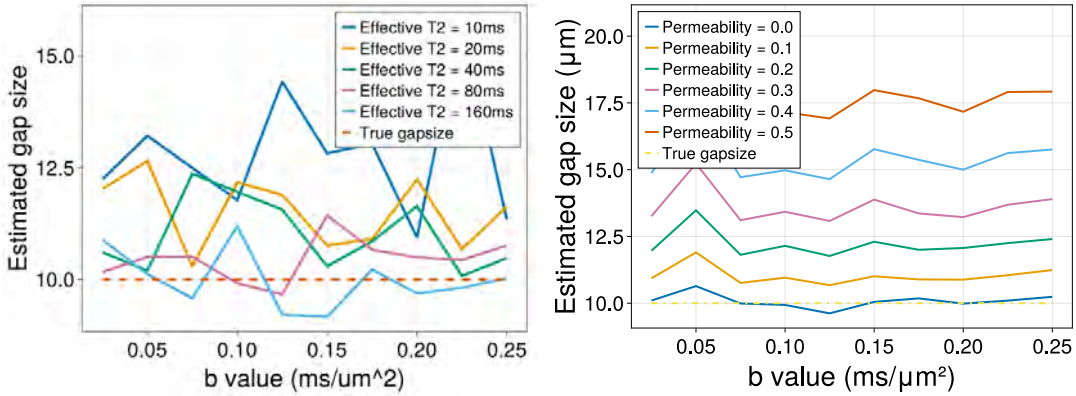

Fig. 2. Biased gap estimation using Mitra's approximation due to MT (left) and permeability (right)

Permeability reduces the signal amplitude for the diffraction pattern because it allows spins to displace beyond the walls, which causes further dephasing under diffusion encoding. In Mitra's approximation, permeability will reduce the fraction of spins that interact with the obstructions, which leads to an overestimation of the gap size in a similar way as MT.

We aim to build on these findings and use the simulator to investigate other phenomena that impact MRI measurements, alongside alternative MRI modalities.

Conclusions: We used a novel Monte-Carlo simulator that combines different microstructural phenomena to simulate MT and permeability's effect on dw-MRI signal. We have found in practice that MT and permeability don't cause significant errors in single compartment dw-MRI measurements comparing to other factors such as irregular structure geometry. It is likely that MT's effect will be more significant in a multi-compartment setting.

Acknowledgements: This research is generously supported by the Wellcome Trust Collaborative Award (215573/Z/19/Z) and China Scholarship Council.

References

[1] P.P. Mitra, P.N. Sen, L.M. Schwartz, Phys. Rev. B 47 (1993) 8565–8574.
[2] E. Özarslan, P.J. Basser, J. Magn. Reson. 188 (2007) 285–294.
[3] M. Cottaar, https://doi.org/10.5281/zenodo.7318657 (2022).

P-22

3D Distortion Compensation of Low Field MR Images Using Soft Registration of a Scan of a 3D Printed Phantom to a Simulated Scan of the Same Phantom

Harry Lanz[a], Karyn E Chappell[a], Mihailo Ristic[a], John V M McGinley[a]

[a]Imperial College London, Exhibition Rd, South Kensington, London SW7 2BX

Introduction: MR images are acquired and reconstructed assuming that the main field, B_0, is uniform. In practice, B_0 is typically only uniform close to isocentre of the imaging volume. In previous work we designed a 0.15T scanner [1] that generates B_0 using a permanent magnet array. The imaging volume of this scanner is approximately a sphere of 15cm diameter. Away from the isocentre our images show significant distortion. To compensate for this distortion, we modelled, using computer aided design (CAD), and 3D printed a calibration phantom. An MR scan was taken of the printed phantom, and a simulated scan of the phantom was generated. Soft registration techniques [2,3] were then used to register the scan to the simulation in order to compensate for and quantify the 3D distortion field.

Methods: The calibration phantom filled the entire imaging volume of the scanner to capture all distortion present in the data. The internal structure was a 3D grid of 5mm radii spheres (with a larger 7.5mm radius sphere at the phantom centre) spaced 17.5mm apart, with spars in each layer supporting the spheres. 9 layers were printed in total. The internal space was filled with vegetable oil to provide contrast in the MR scan. The outer wall had markings modelled into it to orient the phantom correctly in the scanner. A scout scan was used to align the large central sphere with the scanner isocentre. A 150x150x150mm scan of the phantom was then taken with 1x1x1mm voxels.

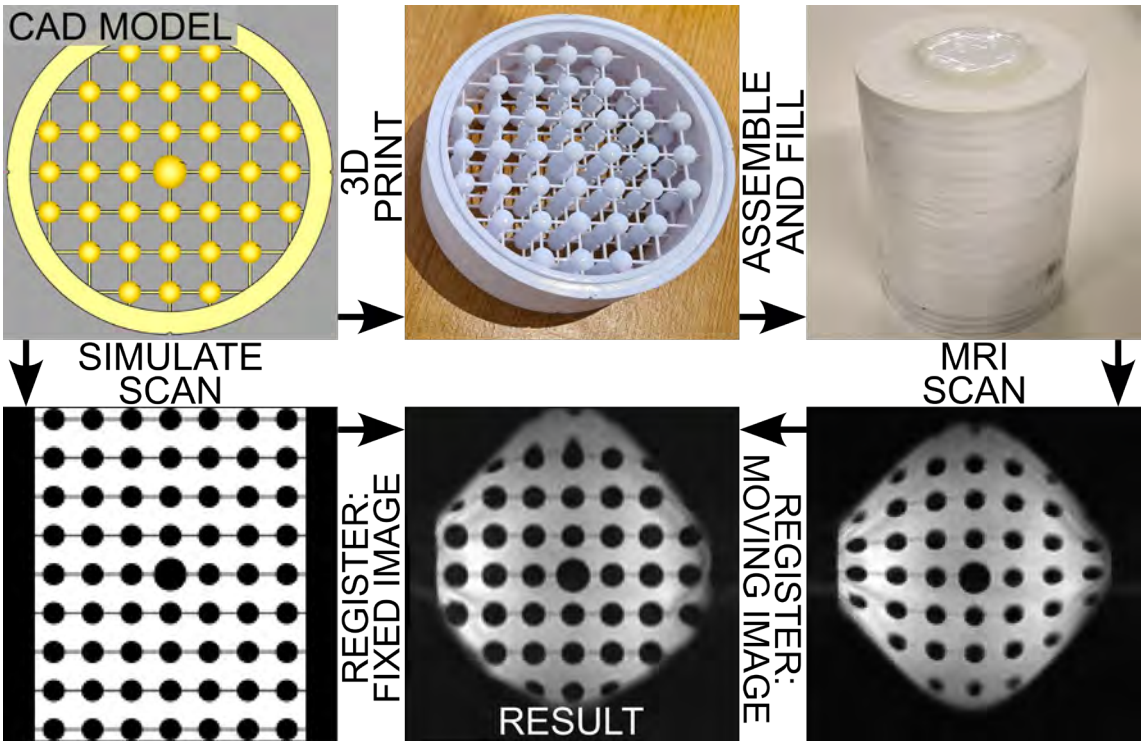

Fig. 1. Overview of modelling, construction, simulation, MR scanning, and distortion compensation results. Top row, left to right, shows CAD to final 3D print. Bottom left shows the simulated scan of the CAD. Bottom right shows the MR scan of the 3D print. Bottom middle shows the MR scan registered to the simulated scan.

The CAD/simulated scans were produced using CadQuery [4], a Python based programmatic CAD software. The simulated scan of the phantom was generated by modelling a 1x1x1mm voxel and computing its intersection with the phantom geometry, the volume of intersection being proportional to voxel intensity. This was repeated for all voxel coordinates corresponding to those in the real scan. The real scan was soft-registered to the simulated scan using B-Spline transforms to account for 3D distortions. Before the soft registration a rigid Euler

registration was performed to eliminate any systematic rotation/translation error from the compensation. The implementation of the registration algorithms were from elastix [2,3] which also output the final transform parameters, allowing the distortion compensation to be applied to other images.

Results: The top left image in Figure 1 shows the CAD model of the phantom. From this model the 3D print (top middle, and top right) and simulated scan (bottom left) were generated. The bottom right image shows the real MR scan of the phantom, and the bottom middle shows the registration results. The data was acquired sagitally, showing a cross section of all layers; spars can therefore only be seen travelling left to right. In the real scan data, the central sphere and close neighbours show low distortion whereas further from the centre, the spheres follow curves, showing in plane distortion. The cross sections of the spheres vary in radii further from the centre, and the spars between spheres bend in and out of the plane, showing out of plane distortion. The real scan also contains a diamond shaped artificial edge where B_0 drops off.

The simulated scan, also shown sagitally, is a distortion free representation of the phantom, all spars and spheres are consistent across the image. At edges within the structure the partial volume effect can be seen, the simulated voxels partially overlap with the phantom geometry here. The simulated scan doesn't have an artificial edge, it captures all of the phantom that fit inside the field of view.

The result of registering the real scan to the simulated scan shows a significant reduction in distortion. The spheres form a regular grid with consistent radii, and the spars are visible across the image.

Discussion: The registered image shows a regular grid of spheres and spars much further from the isocentre than in the original data. By registering the real scan data to the simulated scan data, the 3D distortion can be compensated for. There is still distortion present towards the artificial edges of the image where the original distortion was greatest. This could be improved with a more finely tuned registration mask near the artificial edge. The partial volume effect present in the simulated scans is an important characteristic to replicate, without it, the simulated scans would have unrealistically sharp edges which would be detrimental to the registration process. Distortion during image acquisition also causes bright/dark areas as the voxels are stretched/compressed. This artifact is present in the real scan and registered image. However, with the transformation known, the voxel compression ratios could be calculated and intensities scaled proportionally to correct for this.

Conclusions: Registration of real MR data of a 3D printed phantom to a simulated 'ground truth' scan of the phantom CAD model provides 3D distortion compensation using only image data. A field map of B_0 is not necessary, making the method simple to implement. The transform parameters output from the registration are then applicable to subsequent images taken with the same scanner/sequence. Therefore, distortion of these images can also be corrected, with the potential to also correct for intensity artifacts. The use of programmatic CAD enables easy sharing of the technique as users do not need 3D modelling skills to generate a similar phantom/simulation.

Acknowledgements: This work was partly supported by the Wellcome Trust Innovator Award WT215908/Z/19/Z.

References

[1] McGinley, J.V.M., Ristic, M. and Young, I.R.: A permanent mri magnet for magic angle imaging having its field parallel to the poles. *Journal of Magnetic Resonance* **271**, 60–67 (2016). https://doi.org/10.1016/j.jmr.2016.08.001

[2] Klein, S., Staring, M., Murphy, K., Viergever, M.A. and Pluim, J.P.W.: elastix: A toolbox for intensity-based medical image registration. *IEEE Transactions on Medical Imaging* **29(1)**, 196–205 (2010). https://doi.org/10.1109/TMI.2009.2035616

[3] Rueckert, D., Sonoda, L., Hayes, C., Hill, D., Leach, M. and Hawkes, D.: Nonrigid registration using free-form deformations: application to breast mr images. *IEEE transactions on medical imaging* **18(8)**, 712–721 (1999).

[4] CadQuery, https://github.com/CadQuery/cadquery, Last accessed on: 13/07/2023.

P-23

Do anthropomorphic phantoms enhance compliance with the professional bodies' quality assurance guidelines for MRI in radiotherapy

Meshal Alzahrani[a], David Broadbent[b], Irvin Teh[a], Bashar Al-Qaisieh[b], Adrian Walker[c], Rachel Lamb[c], and Richard Speight[b]

[a]Biomedical Imaging Science Department, University of Leeds, Leeds, United Kingdom
[b]Department of Medical Physics and Engineering, Leeds Teaching Hospitals NHS Trust, Leeds, United Kingdom
[c]Leeds Test Objects, Boroughbridge, United Kingdom

Introduction: Interest in MRI in radiotherapy (RT) has increased due to its unique advantages such as excellent soft tissue contrast. This project aimed to evaluate whether anthropomorphic phantoms enhance compliance with these professional bodies' quality assurance guidelines for MRI in RT as compared to other phantoms.

Methods: Three phantoms were used in this project: an anthropomorphic multimodality head and neck phantom, an American College of Radiology (ACR) large MRI phantom, and a vendor MRI QA phantom, which is a homogeneous phantom. The following tests were carried out:

(1) Magnetic Field Drift test (2) Transmitter and Gain Calibration: T1 relaxation times were calculated for each phantom to determine the appropriate repetition time (TR) to use with each of them. The automatic and manual transmitter gain values were obtained using all phantoms Then, the difference between automatic and manual transmitter gain values was compared. (3) SNR/image quality/ when employing RT accessories: Two scans were obtained for all phantoms. The first scan was performed without the use of RT accessories, and the second was performed with RT accessories. Signal-to-noise ratio (SNR), Percent Image Uniformity (PIU) and percent signal ghosting (PSG) values were calculated using all phantoms.

Tests 1 and 3 were repeated twice immediately upon completion, without changes to the phantom setup, and then, they were repeated twice more with repositioning the phantom. The coefficient of variation (CoV) was calculated for both cases.

(4) QA for MRI-Computed tomography (CT) registration: CT scans were obtained for the anthropomorphic and ACR phantoms. Then, the CT and MRI obtained for the phantoms in the treatment position were rigidly registered within Raystation (RaySearch, Sweden). To calculate the dice similarity coefficient (DSC), a contour of the structure in the middle of the ACR phantom and the brain in the anthropomorphic phantom (Figure 1) was drawn. The contour was repeated two times to calculate the CoV. (5) End to end: After completing the image registration, a treatment plan was created for the anthropomorphic phantom and ACR phantom within Raystation to deliver 2 Gy to the target volume (Figure 1). The radiation dose will be delivered to the ionisation chamber in the anthropomorphic phantom to compare the measured dose with the planned dose.

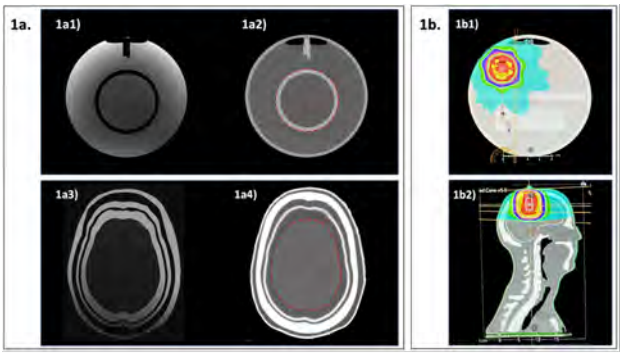

Fig. 1. 1a. MRI and CT images of ACR phantom and anthropomorphic phantom. 1a1) Axial MRI image of ACR phantom, 1a2) Axial CT image of ACR phantom, 1a3) Axial MRI image of anthropomorphic phantom and 1a4) Axial CT image of anthropomorphic phantom. Dashed contour lines show structures that have been contoured to calculate DSC. 1b. Radiation-treatment-planning CT scans. 1b1) Axial image of ACR phantom and 1b2) sagittal reconstruction of anthropomorphic Phantom. Colour wash display shows the dose distribution.

Results: (1) Magnetic Field Drift test: Figure 2 shows the CoV between the central frequency values obtained from each phantom. (2) Transmitter and Gain Calibration: T1 relaxation times of the vendor phantom, ACR phantom, and anthropomorphic phantom were 100, 145.7, and 1200 ms, respectively. Experiments on MRI transmitter gain using three phantoms showed an increasing discrepancy between automatic and manual calculations, from 1.3% with the Vendor phantom, to 6% with the ACR phantom, up to 12.3% with the anthropomorphic phantom. (3) SNR/image quality/ when employing RT accessories: Figure 2 shows the CoV between the results of SNR, PIU and PSG without RT accessories and with RT accessories for each phantom. (4) QA for MRI-CT registration: The CoVs between the DSC values were 0.16 and 1.36 for the ACR and anthropomorphic phantom, respectively. (5) End to end: A treatment plan for the anthropomorphic and ACR phantom has been successfully created. The anthropomorphic phantom can accommodate a dosimeter, while the ACR phantom cannot. Work is ongoing to complete this test.

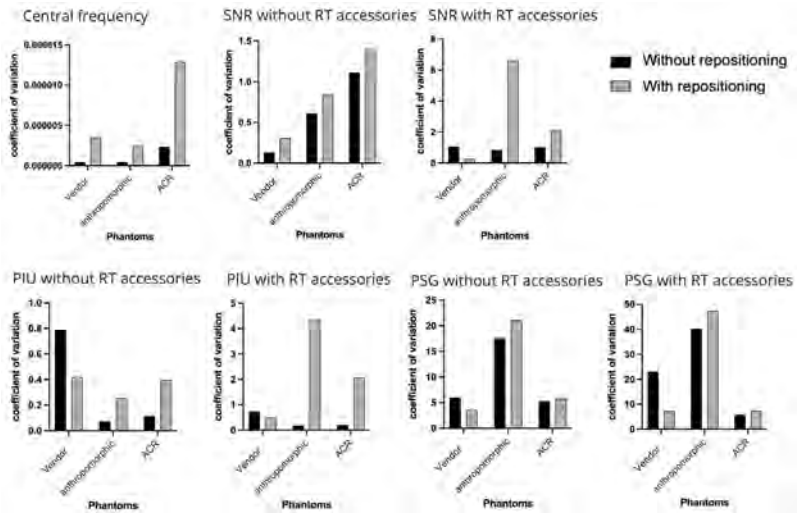

Fig. 2. The CoV between the results.

Discussion: This project demonstrated that the anthropomorphic phantom can be used in tests such as the magnetic field drift and in evaluating SNR, PIU and PSG, like other phantoms. As for the transmitter and gain calibration test, the differences between automatic and manual transmitter gain calculated using the anthropomorphic phantom and ACR phantom were large as compared to the difference calculated using the vendor phantom. Therefore, the anthropomorphic and ACR phantoms are not ideal for this test. Regarding QA for MRI-CT registration, the ACR phantom has much clearer structures than the anthropomorphic phantom. The brain contrast in the CT anthropomorphic phantom images is less pronounced than the structures of the ACR phantom (Figure 1). This may lead to a less accurate contour drawing when using the anthropomorphic phantom. However, the anthropomorphic phantom appears superior to the other phantoms in terms of QA for MRI-CT registration and the end-to-end test because the complexity of the phantom is more representative of the patient and a dosimeter can be placed inside the phantom.

Conclusions: The anthropomorphic phantom is important in QA procedures for MRI in RT, especially in QA for MRI-CT registration and end-to-end tests, and can be considered a complement to the other phantoms.

P-24

Ensuring Accurate Stereotactic Planning During Intraoperative MRI through RF Coil QA

James Thorpe [a], Rafal Panek [a,b], Paul Morgan [a,b]

[a] Nottingham University Hospitals NHS Trust, Medical Physics, Nottingham, United Kingdom
[b] University of Nottingham, School of Medicine, Nottingham, United Kingdom

Introduction: Intraoperative MRI is the application of MRI during a surgical procedure to provide the surgical team with up to date anatomical information to assist them to make more precise and informed decision during an operation (e.g. resection of brain tumour). This requires the use of a stereotactic frame or RF coil that affixes to the patient head throughout the procedure. While standard diagnostic coils usually have defined Quality Assurance (QA) procedures, the coil configuration used for intra-operative MR acquisition does not. In addition, intra-operative MRI requires assurance not only of the image quality but also the ability to identify the fiducials. The QA programme described here has been developed in order to monitor the condition of a third party intraoperative head coil independent of any existing QA programme established for the MRI scanner and standard RF coils [1].

Methods: The QA programme was set up for a NORAS MRI Products intraoperative 8-channel head coil (Noras MRI products, Höchberg, Germany) in conjunction with a Philips Ingenia Elition X 3.0T MRI scanner used for Intraoperative MRI. QA testing has been performed monthly since May 2022 by acquiring a 3D T1-weighted rapid gradient echo (FFE) 1.5mm isometric image with two dynamics of a standard Philips 5L bottle phantom (repetition time = 5.8 ms, Echo time = 2.6 ms, flip angle = 8°, NSA = 1, BW=285) with a large FOV (400 x 322 x 250 mm) covering the whole phantom and fiducial markers and sent to a workstation for analysis.

Offline analysis is performed by identifying the locations of the 5L bottle phantom and 14 fiducial markers (positioned on the interior of the anterior component of the coil) within the image (Matlab, MathWorks). The number and coordinates of the fiducials is evaluated as a test of consistency and equipment setup. A ROI is defined as a sphere covering 75% of the volume of the bottle phantom located within the coil. The SNR within this ROI is calculated using the subtraction method [2] for each individual element image as well as the combined image. An SNR profile along the length of the phantom bottle and used to determine the distance (*D*) outside of the coil at which the SNR within the phantom has decreased to 50% of the SNR of the phantom within the coil. The mean signal intensity and SNR of each of the fiducial markers are also calculated.

Baseline measurements were acquired by performing five repeated QA tests on the coil and phantom in order to establish standard errors for the measurements. The first 15 sets of measurements were then used to establish threshold values for the measurements of SNR and *D*.

Results: Figure 1 shows the SNR of the bottle phantom within the coil from May 2022 to June 2023. It can be seen that although no measurement has exceeded the established thresholds, there appears to be a steady downward trend in SNR (R^2 = 0.55). The individual elements were all functioning correctly for each test. No obvious trends were visible in the measure of *D* or fiducial marker signal intensity. Every fiducial marker was identified in every test and their relative coordinates remained consistent (r_{mean} = 139.5±2.5mm, θ_{mean} = 1.95±0.09°, ϕ_{mean} = -0.24±0.04°).

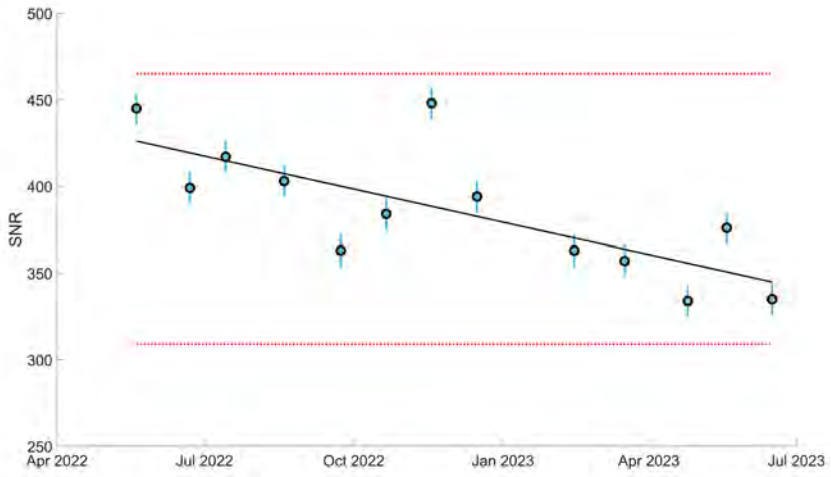

Fig. 1. Signal to noise ratio (SNR) of bottle phantom in NORAS Coil from May 2022 to June 2023 with thresholds shown in red and trend line in black

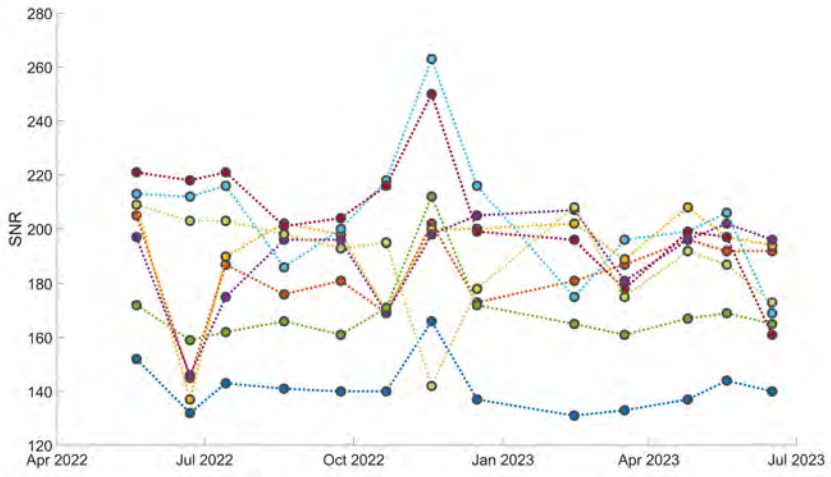

Fig. 2. Signal to noise ratio (SNR) of bottle phantom in NORAS Coil for each coil element from May 2022 to June 2023

Discussion: The downwards trend in SNR for the bottle phantom was not reflected in weekly QA performed on the scanner which suggest NORAS coil SNR deterioration over time. However no thresholds have been exceeded and testing will be continued. If this trend were to continue then the threshold could be expected to be breached in December 2023.

Conclusions: In order to ensure accurate stereotactic planning from MRI a monthly QA programme of the third party NORAS coil has been established. The results of this programme confirm the coil has been functioning at expected SNR levels throughout its usage in intraoperative MRI cases. However, a downward trend in SNR suggests that the coil could be deteriorating over time.

References

[1] Institute of Physics & Engineering In Medicine, Report 112 Quality Control and Artefacts in Magnetic Resonance Imaging; 2017

[2] National Electrical Manufacturers Association. NEMA Standards Publication MS1–2008. Determination of Signal-to-Noise Ratio (SNR) in Diagnostic Magnetic Resonance Imaging. 2008:1-9.

P-25

3D-printable phantoms for quantitative dynamic contrast-enhanced MRI

M. Sulaiman Sarwar[a,b], Antoine Vallatos[a,c], Rachaita Podder[c], Cher Hon Lau[d], Adam Waldman[a,e], Simone Dimartino[b], Michael J. Thrippleton[a,e]

[a]Centre for Clinical Brain Sciences, University of Edinburgh, Edinburgh, UK
[b]Institute for Bioengineering, University of Edinburgh, Edinburgh, UK
[c]Glasgow Experimental MRI Centre, School of Psychology and Neuroscience, University of Glasgow, Glasgow, UK
[d]Institute for Materials and Processes, University of Edinburgh, Edinburgh, UK
[e]Edinburgh Imaging, Edinburgh, UK

Introduction: Dynamic contrast-enhanced (DCE-) MRI is widely used to assess perfusion, permeability, and other tissue properties. Commonly used tracer kinetic models describe passage of intravenously injected contrast agent through tissue [1]. The model parameters reflect physiological properties useful for evaluating disease physiology, progression and treatment. For example, blood-brain barrier (BBB) integrity may be evaluated with the permeability-surface area product *PS*, which characterises leakage of contrast agent from blood capillaries to extravascular extracellular space (EES) [2]. However, differences in scanner hardware, acquisition and analysis can introduce measurement uncertainties, causing significant variation in fitted model parameters [1,3].

Adapted DCE-MRI phantoms are needed for validation of novel techniques, quality assurance and multi-site harmonisation [4]. However, challenges in engineering compromise the ability of existing phantoms to recapitulate DCE-MRI measurements; specifically they do not allow manipulation of key relevant tissue properties like the permeability-surface area product (*PS*), plasma volume fraction (v_p) and EES volume fraction (v_e).

Previous work demonstrated the use of 3D-printing to fabricate phantoms mimicking tissue behaviour in DCE-MRI measurements [5]. Their design consisted of a porous 3D-printed (3DP) material containing channels to represent blood vessels, which was integrated into a flow circuit generating a clinically relevant arterial input function (AIF). This study investigates how changes in 3D-printing parameters affect DCE-MRI model parameters. We hypothesised that increasing the volume fraction of pore forming agents in the 3D-printing formulation (v_{pore}), while keeping the printed channel volume fraction (v_{chan}) constant, would increase v_e and *PS* as measured by DCE-MRI. Likewise, we hypothesised increasing v_{chan} while keeping v_{pore} constant, would increase v_p and *PS*.

Methods: Phantoms were fabricated using digital light processing printing [6]. v_{pore} is the volume fraction of pore forming agents in the printing formulation (proxy for v_e). v_{chan} represents the channel volume fraction defined by a computer model (proxy for v_p). Nine phantoms were fabricated with v_{chan} varied between 0.08, 0.11 and 0.14 (for designed channel diameters of 0.65, 0.75 and 0.85 mm with 2 mm centre-to-centre spacing) and v_{pore} varied between 0.55, 0.65 and 0.74.

A flow circuit facilitated contrast agent injection. Water was pumped (17 mL/min) to the phantom. 3 mL of gadobutrol (69 mM) was injected into a mixer (containing 21 mL of water) upstream of the phantom followed by dilution with 140 mL of water. This protocol was optimised to reproduce the population-averaged AIF model by Georgiou, et al [7].

Phantoms were scanned using an established clinical DCE-MRI protocol [1]. This consisted of a 3D T1W spoiled gradient echo sequence using a 3T Siemens Skyra scanner and 32-channel phased-array head coil, TR/TE = 3.4 ms/1.7 ms, FA = 15°, 2 x 2 x 2 mm resolution (interpolated to 1 x 1 x 2 mm), and 53 volumes acquired every 31.7 s. Mean signal intensities of the AIF and tissue mimicking material regions of interest were converted into concentration and fitted with the extended Tofts (ET) model as described previously [1]. The first post-contrast data point was omitted during fitting to attenuate effects of flow [3].

Results: Figure 1A compares typical measured phantom AIFs with a clinical AIF model. The area under these AIF curves was within 14% of the model AIF. Figure 1B shows the ET model fitted to representative phantom tissue data. The ET model fit data with mean absolute percentage error (MAPE) below 3.0%.

Figure 2A-C shows ET model parameters for all phantoms. Increasing v_{pore} from 0.55 to 0.74 while fixing v_{chan} at 0.11 causes a 29% increase in *PS*, a 24% increase in v_e and a 22% decrease in v_p. Increasing v_{chan} from 0.08 to 0.14 while fixing v_{pore} at 0.65 causes a 36% increase in *PS*, a 1% increase in v_e and a 53% increase in v_p. All phantoms shared these trends.

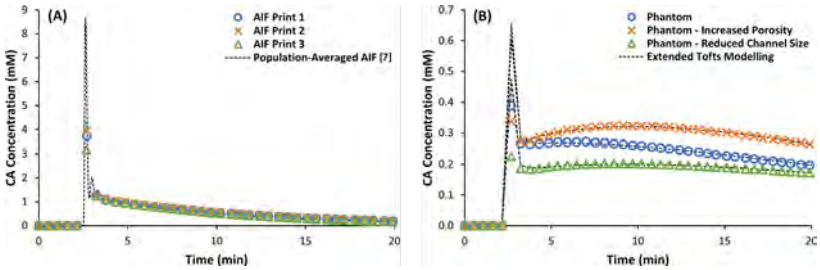

Fig 8. Comparison of (A) population-averaged AIF model with measured phantom AIFs and (B) ET model fitted to phantom tissue concentration curves for (Print 1) v_{pore} = 0.55 and v_{chan} = 0.14, (Print 2) v_{pore} = 0.74 and v_{chan} = 0.14 and (Print 3) v_{pore} = 0.55 and v_{chan} = 0.08.

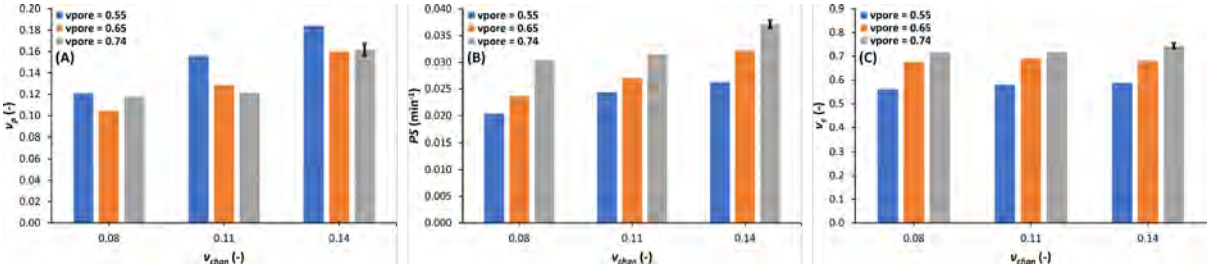

Fig 9. (A-C) Model parameters obtained by fitting the ET model to all phantom data. Error bar for v_{chan} = 0.14 and v_{pore} = 0.74 shows ± 1 SD based on four repeated experiments.

Discussion: The ET model fitted all phantom data, confirming that phantom DCE-MRI signals can be modelled using a two-compartment pharmacokinetic model. As hypothesised, an increase in phantom v_{pore} led to an increase in fitted *PS* and v_e, reflecting faster transport between channels and pores, and an increase in porosity, respectively. Similarly, an increase in phantom v_{chan} led to an increase in fitted *PS* and v_p, reflecting increased channel surface area and channel volume fraction, respectively. Another trend is v_p decreasing with increasing phantom v_{pore}, likely due to water content within channels (as a fraction of the total phantom water content) decreasing because of increasing v_{pore}. Future work will focus on: (1) comparing phantom performance between clinical and preclinical scanners and (2) establishing empirical values for phantom porosity and channel size in order to elucidate the relationship between physical phantom and DCE-MRI model parameters.

Conclusions: By combining tuneable 3DP phantoms with a flow circuit, we mimicked in-vivo DCE-MRI experiments and altered modelled "tissue" properties in a controllable fashion. These results suggest that 3DP phantoms have the potential to address limitations of previous phantom designs and facilitate technical validation, quality assurance and multi-site harmonisation of DCE-MRI.

References

[1] Heye, A.K. *et al*. *NeuroImage* **125**, 446–455 (2016).
[2] Thrippleton, M.J. *et al*. *Alzheimers Dement.* **15**, 840–858 (2019).
[3] Manning, C. *et al*. *Magn. Reson. Med.* **86**, 1888–1903 (2021).
[4] Shukla-Dave, A. *et al*. *J. Magn. Reson. Imaging* **49**, e101–e121 (2019).
[5] Sarwar, M.S. *et al*. *Proc Intl Soc Mag Reson Med* **30**, (2022).
[6] Dimartino, S. *et al*. *Bioresour. Bioprocess.* **9**, 20 (2022).
[7] Georgiou, L. *et al*. *Magn. Reson. Med.* **81**, 1955–1963 (2019).

P-26

A dual-frequency $^{1}H/^{19}F$ body coil array at 3 Tesla

Paul McElhinney[1], Sarah Allwood-Spiers[2], Graeme Keith[1], Belinda Ding[3], David Brennan[4], Natasha Fullerton[2], Celestine Santosh[2,4], David Porter[1], Shajan Gunamony[1,5]

[1]Imaging Centre of Excellence, University of Glasgow, Glasgow, Scotland; [2]NHS Greater Glasgow & Clyde, Glasgow, United Kingdom; [3]Siemens Healthcare Limited, Frimley, United Kingdom; [4]Aurum Biosciences Limited, Glasgow, United Kingdom; [5]MR CoilTech Limited, Glasgow, United Kingdom

Introduction: To investigate the use of a perfluorocarbon (PFC) for use in as diagnostic tool in the investigation of inflammation inside the human body, an eight-channel transceiver $^{1}H/^{19}F$ dual-frequency 3-Tesla body array has been developed and evaluated on a human subject. The switching between the two frequencies is enabled by the control signals that are programmed through the coil file. The dual-frequency operation enables the same coil to be used at both frequencies, which reduces scan time, improves patient comfort, and provides accurate anatomic localisation.

The array consisted of four transceiver elements each on the anterior and posterior halves. A 1x2 power splitter is used to feed the RF power from the scanner to the two halves and the power is split further within each half using a 1x4 splitter. The transmit phase between the coil element input and power splitter is controlled by coaxial cable lengths to homogenise the B_1^+ field over the region of interest (ROI) containing the liver and spleen.

This abstract presents the first in-vivo results, and a comparison with the electromagnetic (EM) simulations used for B_1^+ homogenisation, SAR assessment and validation of the dual-frequency array.

Methods: EM simulation of the radiofrequency (RF) coil was performed using CST Studio Suite 2021 (Dassault Systems, France). The simulations were performed at both ^{1}H and ^{19}F frequencies (123.2 MHz and 115.9 MHz). The coil is locally shielded and extended 200mm along the z-direction. The adjacent array elements are overlapped and the coupling between the next-neighbouring elements are decoupled using transformers[2]. The model included all component losses, scanner bore and cable loss.

The coil was tuned and matched to the Duke body model[5], and single channel B_1^+ field maps were extracted to calculate the phase shims required to generate the preferred B_1^+ distribution. The optimisation criteria included the mean reference voltage, local 10g SAR, SAR efficiency and B_1^+ homogeneity for a ROI covering the central mass of the Duke torso. A final shim was selected maximising the homogeneity of B_1^+ field in the liver and spleen and the cable phases on the coil adjusted accordingly. Using this final shim solution, additional simulations of other body models and coil positions were generated. These were used along with experimental validation of the B_1^+ maps and temperature rise on phantoms to perform safety validation. With conservative safety margins applied in the coil file, the coil was approved locally for human imaging. Experimental validation of the B_1^+ maps was performed in a 3T MRI system (MAGNETOM Prisma, Siemens Healthineers Germany).

To demonstrate the image quality at 1H and 19F frequencies a subject was positioned with a vial containing the ABL-101 solution attached to the left anterior side of the coil housing and imaged using a gradient echo sequence at the ^{1}H frequency and at the ^{19}F frequency. Switching may be done without disturbing the subject by moving the coil plug from the ^{1}H to ^{19}F /X-nuclei plug on the patient table.

Results: A comparison of the measured and simulated B_1 maps is shown in Figure 1 for the subject and for the Duke human body model ^{1}H frequency. The location of both slices is 5mm inferior to the isocentre.

Figure 2 shows the gradient echo images of the subject, showing the coverage (a-c), a TSE image acquired during a breath hold (d), and an image acquired at the ^{19}F frequency (e), where we can clearly see the test vial filled with ABL-101.

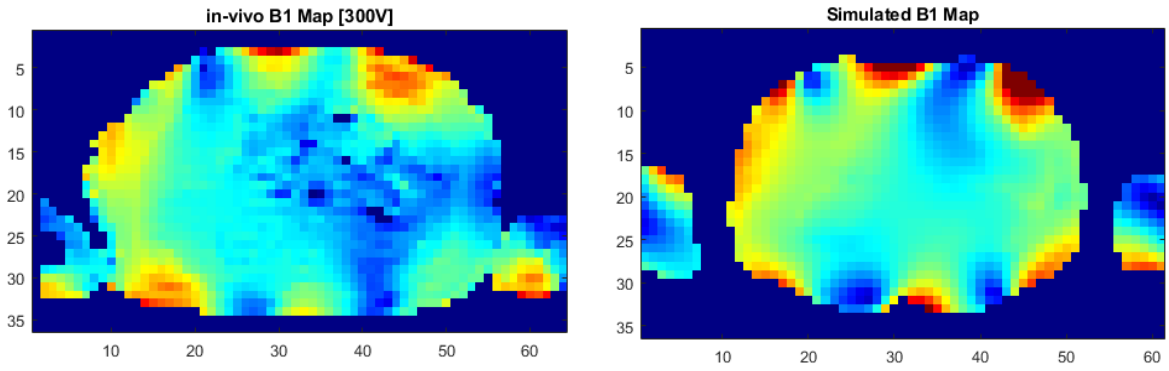

Fig. 1. (right) Measured B_1^+ map in human subject (left) simulated B_1^+ map in "Duke" body model. Demonstrating the optimum shim solution for imaging of the liver and spleen.

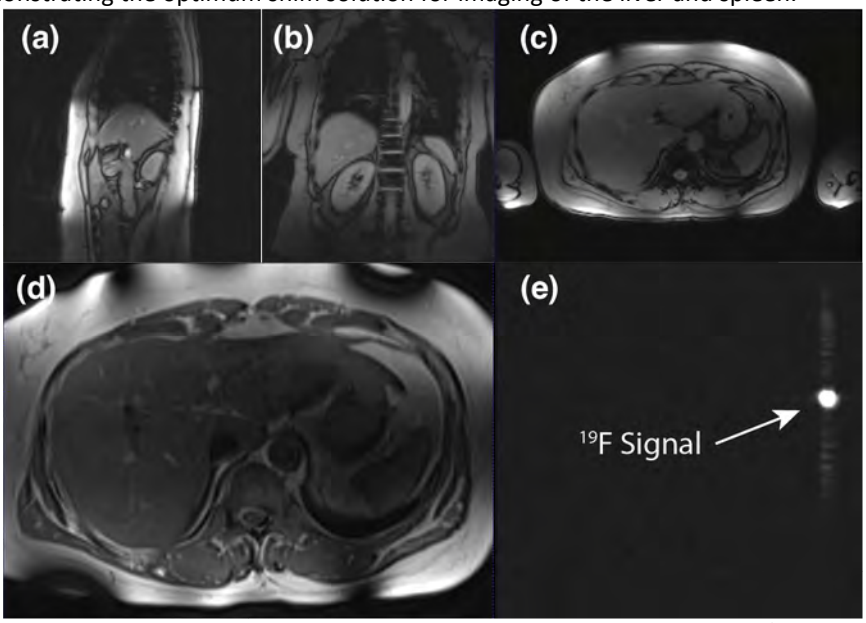

Fig. 2 (a, b) localiser images, (c) GRE image at ^{1}H and, (d) TSE image at ^{1}H, (e) GRE image at ^{19}F showing vial containing PFC compound.

Discussion: In selecting the best shim for this application, we chose the minimum standard deviation for its coverage since it is desirable in this application that we can get a consistent signal from both the liver and the spleen. While the SAR is higher in this case it is not so high that it should provide any difficulty and the benefit of increased coverage is of higher value here. The ability to switch between ^{19}F and ^{1}H is advantageous as we can maintain the subject position for both imaging sequences. We were able to achieve a 0.85 mm resolution using a TSE sequence with good homogeneity over the liver.

Conclusions: For the eight-channel transceiver ^{1}H/^{19}F dual-frequency 3-Tesla body array, B_1 simulations were performed at both frequencies and experimentally validated at ^{1}H frequency. Simulation and measurement shows the robustness of the single phase shim solution in both phantom and in-vivo studies.

References

[1] Adriany G et al. Magn Reson Med. 2005;53(2):434-445. doi:10.1002/mrm.20321.
[2] Williams SN et al. Front Phys. Jul 2021. Vol 9.
[3] Hoffmann J et al. 2016;29(9):1131-1144. doi:10.1002/nbm.3290
[4] Darçot E et al. *NMR Biomed*. 2020;33(1):e4212. doi:10.1002/nbm.4212
[5] Christ A et al. Magn Reson Med. 2010;64(2):439-446. doi:10.1002/mrm.

Author Index

MAGNETOM Cima.X

Make the difference.

siemens-healthineers.co.uk/cima-x

From oncological conditions to neurological disorders, MRI plays a key role in the clinical pathway of many patients. But despite the continuous medical and technological progress, there are still many diseases not fully understood and patients that physicians struggle to help.

That is why we keep pushing the boundaries of high-end 3T MRI to support clinicians and scientists in their mission to address these challenges and ultimately improve patient care. MAGNETOM Cima.X is our strongest 3T MRI system ever that provides deeper insights into the human body.

Transforming patient care and science, it features Gemini Gradients with 200[1] mT/m at 200 T/m/s for an unparalleled whole-body performance.

Discover more

With MAGNETOM Cima.X you can make the difference.

- Unprecedented whole-body performance of 200[1] mT/m at 200 T/m/s in clinical use
- Imaging powerhouse for consistent and precise head-to-toe images
- Deep Resolve deep-learning based image reconstruction for increased productivity in MRI
- The Open Recon[2] platform boosts collaboration and customisation
- Intuitive powerhouse for complex scientific work and day-to-day tasks

1 ≥ 200 mT/m (±3% for design tolerances)

2 Open Recon is to add clinical reconstructions to the system, if signed and released for clinical use by Siemens Healthineers. Any other image reconstruction used, e.g., by researchers, is automatically labelled not for diagnostic use, which may require observation of national regulations.

SIEMENS Healthineers

Proud supporters of the ISMRM British & Irish Chapter

GOLD STANDARD PHANTOMS

Functional Stability Reference

fMRI is used daily in clinics around the world to map eloquent areas prior to brain surgery. The lack of an fMRI signal in such a region close to a lesion might not mean that this region is not active. In fact, if your MRI scanner is not stable, you might generally not be able to detect small, reduced or distorted signals.

an easy way to test the stability of your MRI scanner*

*As prescribed by the fBIRN consortium more than 20 years ago...

absence of evidence IS NOT evidence of absence

experience our wide range of phantoms at:

goldstandardphantoms.com

GOLD STANDARD PHANTOMS

Unit H13
Steel Bank Business Park
20 Prospect Road
Sheffield, S2 3EN
United Kingdom

BRUKER

Maxwell Magnets

- Intelligent Magnet Technology

MRI

Innovation with Integrity


ABERDEEN
DYCE
VICTORIA STREET
Aberdeen International Airport
727
17 P&J Live Arena
INVERURIE ROAD
A96
B997
A90 North
THE PARKWAY
ELLON ROAD
AUCHMILL ROAD
River Don
GREAT NOTHERN ROAD
Seaton Park
St Machar's Cathedral
OLD ABERDEEN
Aberdeen Treasure Hub
University of Aberdeen
King's College
KING STREET
Aberdeen Sports Village
Aberdeen Beach
Pittodrie Stadium
19 Beach Ballroom
NORTH ANDERSON DRIVE
Aberdeen Royal Infirmary
Westburn Park
Victoria Park
Curl Aberdeen
Codonas
Woodend Hospital
SKENE ROAD
UNION STREET
MARKET STREET
FOOTDEE
QUEENS ROAD
ALBYN PLACE
A944
Hazlehead Park
Torry Battery
Johnston Gardens
The Gordon Highlanders Museum
GREAT WESTERN ROAD
ANDERSON DRIVE
HOLBURN STREET
VICTORIA ROAD
Winter Gardens
Duthie Park
South Harbour
GREAT SOUTHERN ROAD
A93
NORTH DEESIDE ROAD
WEST TULLOS ROAD
Deeside Way
Robert Gordon University
SOUTH DEESIDE ROAD
STONEHAVEN ROAD
River Dee
B9077
18 Ardoe House Hotel
A90 South
WELLINGTON ROAD

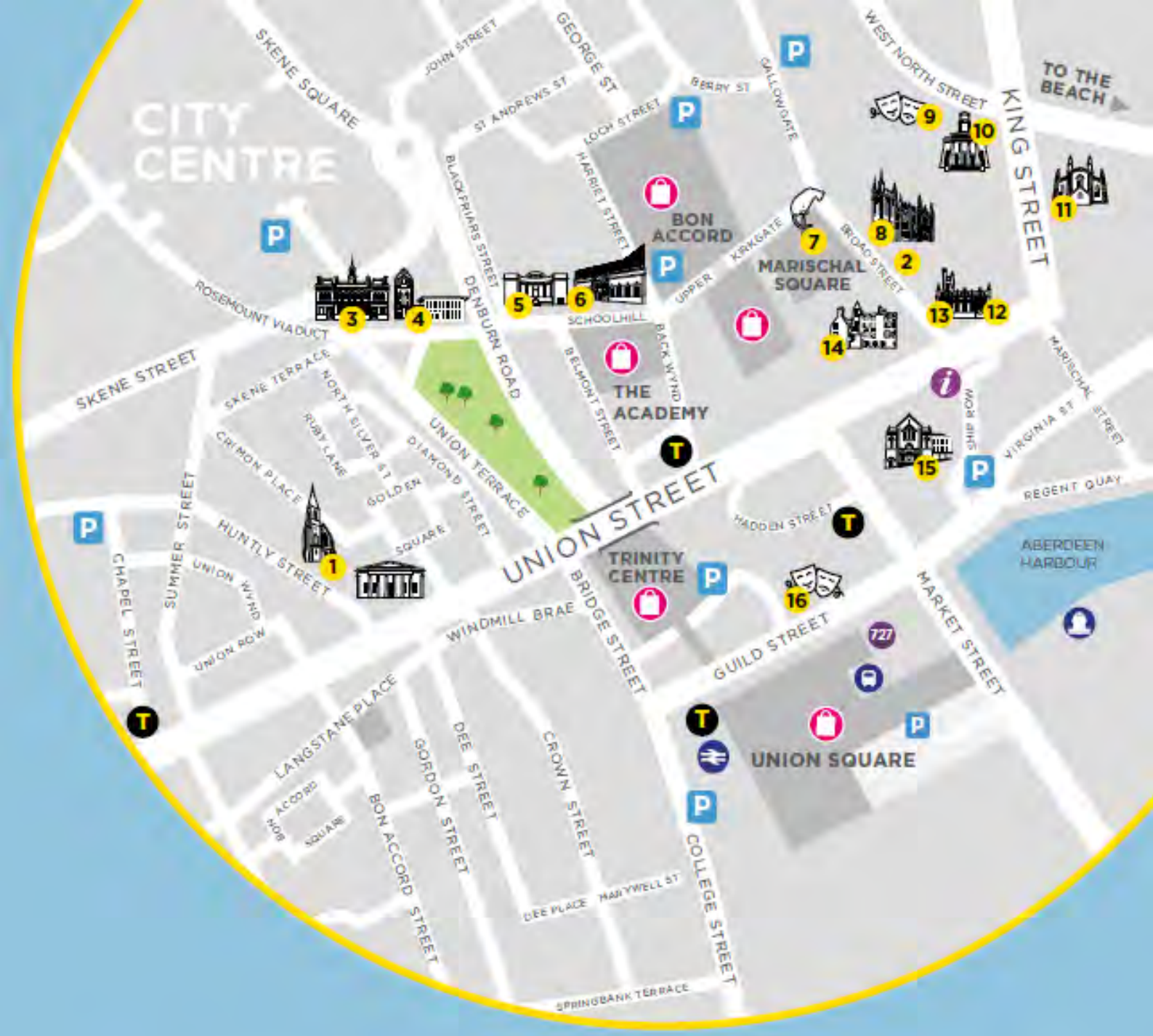

Aberdeenshire
Scotland

#visitABDN #beautifulABDN
www.visit**abdn**.com

- ABERDEEN INTERNATIONAL AIRPORT
- BUS STATION
- PARKING
- TRAIN STATION
- AIRPORT BUS TO CITY CENTRE
- SHOPPING CENTRE
- FERRY TERMINAL
- TAXI RANK
- VISITOR INFORMATION

1. ST MARY'S CATHEDRAL
2. BROAD STREET (bus pick up point for Dinner & Ceilidh)
3. CENTRAL LIBRARY
4. HIS MAJESTY'S THEATRE
5. COWDRAY HALL
6. ART GALLERY
7. POISED LEOPARD
8. MARISCHAL COLLEGE
9. THE LEMON TREE
10. ARTS CENTRE
11. ST ANDREW'S CATHEDRAL
12. THE TOLBOOTH MUSEUM
13. TOWN HOUSE (Civic Welcome Reception Venue)
14. PROVOST SKENE'S HOUSE
15. MARITIME MUSEUM
16. TIVOLI THEATRE
17. P&J LIVE AT TECA (Conference Venue)
18. ARDOE HOUSE HOTEL (Conference Dinner Venue)
19. BEACH BALLROOM (Ceilidh Venue)

ISMRM | British & Irish CHAPTER

'New Horizons in MRI'

13-15 September 2023

1495 UNIVERSITY OF ABERDEEN

CAMPUS MAP

1 Zoology Building
2 Cruickshank Building
3 23 St Machar Drive
4 King's Museum (Old Town House)
5 Students' Union Building
6 St Mary's
7 Fraser Noble Building
8 Elphinstone Road Halls
9 Science Teaching Hub
10 The Sir Duncan Rice Library
11 Meston Building
12 Multi-Faith Chaplaincy
13 Confucius Institute
14 Security Office/Mailroom
15 Counselling Service
16 Edward Wright Building
17 Edward Wright Annexe
18 MacRobert Building
19 William Guild Building
20 Arts Lecture Theatre
21 Taylor Building
22 Old Brewery
23 New King's
24 Regent Building
25 University Office
26 Elphinstone Hall
27 Linklater Rooms
28 King's College Chapel
29 King's College Centre
30 King's College
31 King's Pavilion
32 50-52 College Bounds
33 Butchart Centre
34 Crombie Annexe
35 Crombie Halls
36 Rocking Horse Nursery
37 King's Hall
38 Powis Gate/Muslim Prayer Room
39 Johnston Hall
40 Johnston Annexe
41 Humanity Manse
42 Bedford Road Workshops/CHP
43 Johnston Central
44 International Centre
45 Infohub
46 46-48 College Bounds

(P) Regulated Parking

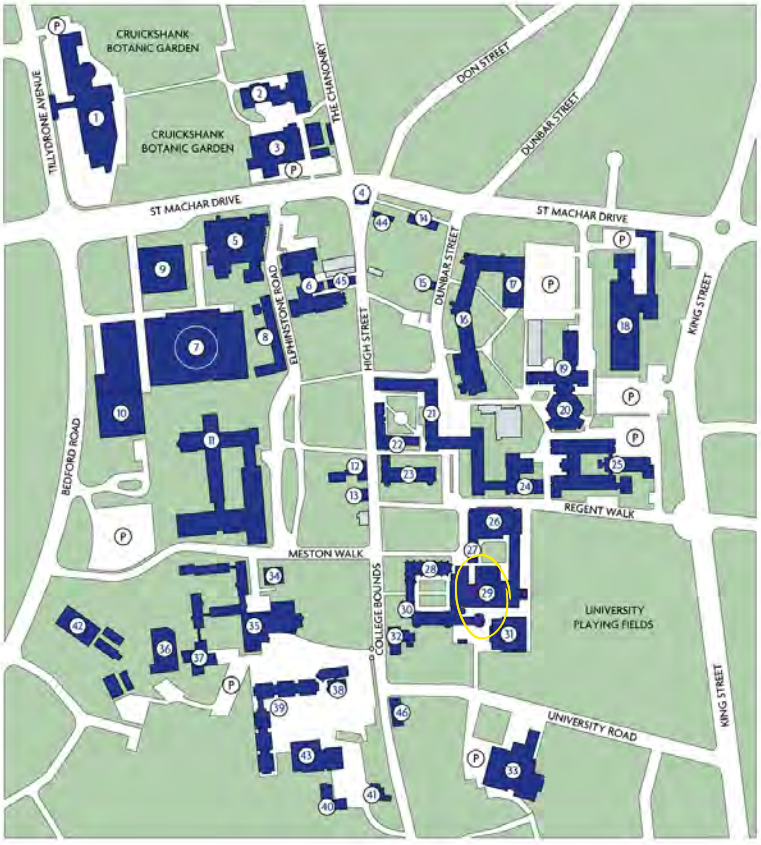

VENUE AND ADDRESS

King's Conference Centre, University of Aberdeen, Scotland, UK, AB24 3FX

CONTACT INFORMATION

Event Organisers
Contact: Julie Dixon, CPD Services
Address: University of Aberdeen, Room 29, University Office, King's College, Aberdeen, AB24 3FX
Web: www.abdn.ac.uk/events/conferences/bicismrm2023
Email: cpdservices@abdn.ac.uk
Tel: +44 (0) 1224 272523